EXPLORING THE DISTANT UNIVERSE WITH CROSS-CORRELATION STATISTICS

by

Daniel J. Matthews

BS Physics, University of Iowa, 2005

BS Astronomy, University of Iowa, 2005

MS Physics, University of Pittsburgh, 2007

Submitted to the Graduate Faculty of

the Kenneth P. Dietrich School of Arts and Sciences in partial

fulfillment

of the requirements for the degree of

Doctor of Philosophy

University of Pittsburgh

2014

UNIVERSITY OF PITTSBURGH

DEPARTMENT OF PHYSICS AND ASTRONOMY

This dissertation was presented

by

Daniel J. Matthews

It was defended on

January 14th 2014

and approved by

Jeffrey A. Newman, University of Pittsburgh

Andrew R. Zentner, University of Pittsburgh

W. Michael Wood-Vasey, University of Pittsburgh

Ayres Freitas, University of Pittsburgh

Rupert A. C. Croft, Carnegie Mellon University

Dissertation Director: Jeffrey A. Newman, University of Pittsburgh

EXPLORING THE DISTANT UNIVERSE WITH CROSS-CORRELATION STATISTICS

Daniel J. Matthews, PhD

University of Pittsburgh, 2014

Future cosmological surveys will require distance information for an extremely large number of galaxies in order to gain insight into the structure and history of our Universe. Current methods of obtaining accurate distance information such as measuring the redshifts of galaxies via spectroscopy are not feasible for such enormous datasets, mainly due to the long exposure times required. Photometric redshifts, where the redshift is measured using broadband imaging through only a few filters, are a promising avenue of study, although there are inherent limitations to this method making them less understood than spectroscopic redshifts. Understanding these limitations and improving the calibration of photometric redshifts will be very important for future cosmological measurements. This thesis presents tests of a new technique for calibrating photometric redshifts that exploits the clustering of galaxies due to gravitational interaction. This cross-correlation technique uses the measured spatial clustering on the sky of a photometric sample that has only imaging information, with a spectroscopic sample that has secure and accurate redshifts. These tests shows that measurements of this clustering as a function of redshift can be used to accurately reconstruct the true redshift distribution of the photometric sample. In addition, this thesis shows how similar clustering measurements can be used to constrain the contamination of a high redshift candidate sample by low redshift interlopers. Finally it describes a new catalog that combines spectroscopic redshifts and deep photometry that can be used as a testbed for future photo-z studies.

TABLE OF CONTENTS

LIST OF TABLES

LIST OF FIGURES

PREFACE

First and foremost I would like to thank my advisor Jeff Newman for his patience and support throughout my years in graduate school. I also wish to acknowledge the rest of my thesis committee who helped provide direction in the completion of this thesis: Michael Wood-Vasey, Andrew Zentner, Rupert Croft and Ayres Freitas. In addition I would like to thank my collaborators who contributed to the work contained in this thesis: Alison Coil, Michael Cooper, Stephen Gwyn and Darren Croton. This work also benefited greatly from helpful discussions with Nikhil Padmanabhan, Larry Wasserman, Chris Genovese, Peter Freeman, and Chad Schafer. This thesis would not have been possible without all of their help and support. I also want to thank all of the teachers who helped me along the way in my pursuit of knowledge, as well as Michael Flatté who gave me my first opportunity to work in research as an undergraduate.

I also would like to thank my family for all of their love and support, in particular my parents who patiently waited for me to find my own way while letting me know they were always there if I needed them. I want to thank my friends and officemates throughout the years for providing support as well as welcome distractions during my time here. I also would like to thank the late Ron Tesdahl, who used his subtle teaching style and great sense of humor to teach me many lessons about work and life. He not only taught me how to work, but also that the work should never be done until you have something you are proud of. He helped me become who I am today and he is missed.

1.0 INTRODUCTION

Nearly a century ago it was first established that the Universe is expanding by noting that the spectra of almost all galaxies in all directions are redshifted to longer wavelengths, implying that they are all receding away from us at some velocity (Hubble, 1929). For decades after this discovery it was predicted that this expansion should be slowing, because if the Universe had only consisted of matter and radiation with no other agent acting to influence the expansion, then the gravitational attraction of matter should work to decrease its rate. Surprisingly, measurements of the distances to Type Ia supernovae and other observations have shown that the expansion rate is in fact accelerating (Riess et al., 1998; Perlmutter et al., 1999). This accelerating expansion is generally attributed to an unknown component of the energy density of the universe commonly referred to as "dark energy." Although the observational evidence for the existence of dark energy is conclusive, its properties are not well known. The nature of dark energy has become one of the most important unanswered questions in cosmology.

There have been many theoretical explanations for dark energy put forward over the last several years. For example, this unknown contribution to the energy density of the universe could be explained by Einstein's cosmological constant, introduced into his General Theory of Relativity to counteract the attractive force of gravity and thought to represent an intrinsic energy associated with the empty vacuum of space. It has also been proposed that the accelerated expansion may be driven by a smooth dynamical scalar field usually referred to as quintessence. There is also the possibility that dark energy does not exist and what we are interpreting as an accelerated expansion actually points to a breakdown of General Relativity at large scales.

Dark energy is generally characterized by its equation of state $w \equiv P/\rho$, where P is the

pressure and ρ is its mass density. By allowing for the evolution of w with time we can define $w_a \equiv dw/da$, where $a(t)$ is the scale factor describing the relative expansion of the universe (normalized to be 1 today) (Johri & Rath, 2007). Determining constraints on these dark energy parameters has become the goal of many current and future cosmological probes (e.g. DES, LSST, WFIRST, and Euclid) (The Dark Energy Survey Collaboration, 2005; Tyson & Angel, 2001; Green et al., 2012; Albrecht et al., 2009; Beaulieu et al., 2010). For example, the cosmological constant model of dark energy predicts an equation of state where $w = -1$ with the time derivative $w_a = 0$, and significant deviations from this would rule out that model.

In addition to supernovae surveys, other techniques are being employed to explore the expansion history of the Universe and probe the parameters of dark energy, whether it is through its effect on distance as a function of redshift, the time evolution of the expansion rate or the growth rate of structure. For instance, in the hot dense phase of the early Universe temperatures were high enough to ionize all of the baryonic matter, and so the Universe consisted of an electron-baryon plasma permeated by photons. The interplay of the photons with this plasma generated sound waves that propagated throughout the Universe, and these pressure waves are referred to as Baryon Acoustic Oscillations (BAO) (Peebles & Yu, 1970). As the Universe expanded and cooled the electrons and baryons combined to form neutral atoms, making the Universe essentially transparent to photons. This phase of the Universe occurred approximately 400,000 years after the Big Bang and is referred to as "recombination". At this time the baryonic matter decoupled from the photons, and it is expected that the slight under- and over-densities of baryons due to BAO were frozen into place at the moment of recombination and should be imprinted on the galaxy distribution today. Their existence has been verified through studying the clustering of galaxies on large scales (Eisenstein et al., 2005; Percival et al., 2010). The scale of the BAO acts as a "standard ruler", and so by measuring its size as a function of redshift it is possible to map the expansion history of the Universe.

The growth of cosmic structure will also be influenced by the presence of dark energy and can be used to study its properties. Since recombination the galaxies and clusters of galaxies we observe, along with the distribution of dark matter halos, have formed over time under the

influence of gravity, and the characteristics of this growth can be used to probe dark energy. This evolution of the galaxy and dark matter density fields can be characterized in various ways. One example is from measuring the matter power spectrum and the resulting RMS amplitude of mass fluctuations on a given scale. The evolution of this amplitude over time can be used to constrain dark energy parameters in a way that is complementary to supernovae measurements (Duran et al., 2012). Another possibility is using weak gravitational lensing measurements. The images of distant galaxies become slightly distorted due to the bending of light as it passes through the gravitational potentials of intervening large-scale structure. These distortions can be used to characterize the density field, with the advantage that it is sensitive to the dark matter distribution rather than galaxies (Bartelmann & Schneider, 2001).

In order to measure how cosmological parameters evolve with redshift, it will be necessary to determine redshifts of many objects with widely varying properties. There are two predominant methods for measuring galaxy redshifts. They can be determined using spectroscopy to finely measure the flux from a galaxy as a function of wavelength, where the shift in wavelength of sharp spectral features such as absorption and emission lines can tell you the redshift. Alternatively, redshifts can be measured using photometry where the galaxy's light is measured through only a few filters. Since the sharp features become washed out using broadband photometry, the latter method must use broader features such as spectral breaks to determine redshifts. These photometric redshifts, or photo-z's, are inherently less precise and more prone to systematic errors than redshifts measured spectroscopically due mainly to the information that is lost by measuring a galaxy's light through only a few filters. However an advantage of photo-z's is that it is possible to obtain redshifts for a much larger number of galaxies over a given time period, primarily due to the longer integration time required to obtain galaxy spectra with significant signal-to-noise. In addition, with photo-z's it is possible to obtain redshifts for objects that are too faint for spectroscopy.

Because of the difficulties in obtaining high precision photometric redshifts, many dark energy experiments are unlikely to treat the redshifts of individual objects as known. Instead, the objects will often be divided into bins in photo-z (e.g. Ma et al. 2006). In the simple case of a photo-z distribution with Gaussian scatter, the photo-z bin is characterized by the mean,

$\langle z \rangle$, and width of the bin, σ_z. However if the objects are binned using photometric redshifts, the *true* redshift distribution of objects in a given bin will be different from the photo-z distribution even if there are only random uncertainties in the photo-z's. Understanding this true distribution of objects placed into a photo-z bin by some algorithm, i.e. calibrating photometric redshifts, will be very important for obtaining accurate measurements of dark energy parameters.

Many of the cosmological measurements to be performed with future photometric surveys will require extremely well-characterized redshift distributions of the galaxy samples used for the measurements (Albrecht et al., 2006; Huterer et al., 2006; Ma et al., 2006). These surveys will be imaging a large number of objects ($\sim 10^8 - 10^9$) to very faint magnitudes (~ 28), making spectroscopic redshifts impractical. We can measure the redshifts of these objects using photometric information, e.g. by using a large set of spectroscopic redshifts to create templates of how color varies with redshift (Connolly et al., 1995). However current and future spectroscopic surveys will be highly incomplete due to selection biases dependent on redshift and galaxy properties (Cooper et al., 2006). Because of this, along with the catastrophic photometric errors[1] that can occur at a significant ($\sim 1\%$) rate (Sun et al., 2009; Bernstein & Huterer, 2010), photometric redshifts are not as well understood as redshifts determined spectroscopically.

If future dark energy experiments are to reach their goals, it is necessary to develop a method of calibrating photometric redshifts with high precision (Albrecht et al., 2006; Huterer et al., 2006; Ma et al., 2006). Current projections for LSST cosmic shear measurements estimate that the true mean redshift of objects in each photo-z bin, $\langle z \rangle$, must be known to better than $\sim 0.002(1 + z)$ (Zhan & Knox, 2006; Zhan, 2006; Knox et al., 2006; Tyson, 2006) with stringent requirements on the fraction of unconstrained catastrophic outliers (Hearin et al., 2010), while the width of the bin, σ_z, must be known to $\sim 0.003(1 + z)$ (LSST Science Collaborations: Paul A. Abell et al., 2009).

Systematic uncertainties in redshifts are expected to be dominant for many of the planned dark energy experiments, and it is therefore essential to develop a method of calibrating

---

[1]such as contamination from overlapping or unresolved objects; this is a frequent problem in deep surveys, particularly at high redshifts, cf. Newman et al. (2013b)

photometric redshifts with high precision that will also minimize the impact of systematic errors. In this thesis I present a new technique for calibrating photometric redshifts that combines information from both photometric and spectroscopic surveys. The spectroscopic sample provides us with secure and accurate redshift information for a sample of galaxies, and by measuring the clustering of these objects with the photometric sample as a function of redshift we can obtain redshift information about the photometric objects. This technique exploits the fact that objects at similar redshifts will cluster with each other due to gravitational interactions. The benefit of this cross-correlation technique is two-fold: 1) it can be used to obtain redshift information for a much larger sample size which will improve the precision of cosmological parameter measurements, and 2) it gives the *true* distribution of the photometric sample which will improve the accuracy.

In chapter 2 I present a test of this cross-correlation technique for calibrating photometric redshifts, as well as discuss the effect of weak gravitational lensing on the method. The analysis presented in sections 2.1 and 2.2 have also been published in The Astrophysical Journal (Matthews & Newman, 2010, 2012). In chapter 3 I present a technique where similar clustering measurements can be used to constrain the contamination level of a high redshift ($z \sim 4 - 8$) candidate sample by low redshift ($z \sim 2$) "interlopers". In chapter 4 I describe a new data catalog I constructed combining spectroscopic redshifts and deep photometry that can be used as a testbed for future photo-z studies. The description of this catalog has also been published in The Astrophysical Journal Supplement (Matthews et al., 2013). Finally, in chapter 5 I conclude.

2.0   CROSS-CORRELATION TECHNIQUE APPLIED TO CALIBRATING PHOTOMETRIC REDSHIFTS

In this chapter I present a new technique for calibrating photometric redshifts measured by other algorithms, which exploits the fact that objects at similar redshifts tend to cluster with each other. If there are two galaxy samples in the same region of sky, one with only photometric information and the other consisting of objects with known spectroscopic redshifts, we can measure the angular cross-correlation between objects in the photometric sample and the spectroscopic sample as a function of spectroscopic z. This clustering will depend on both the intrinsic clustering of the samples with each other and the degree to which the samples overlap in redshift. Autocorrelation measurements for each sample give information about their intrinsic clustering, which can be used to break the degeneracy between these two contributions. The principal advantage of this technique is that, while the two sets of objects should overlap in redshift and on the sky, it is not necessary for the spectroscopic sample to be complete at any given redshift. Therefore it is possible to use only the brightest objects at a given z, from which it is much easier to obtain secure redshift measurements, to calibrate photometric redshifts. Even systematic incompleteness (e.g. failing to obtain redshifts for galaxies of specific types) in the spectroscopic sample is not a problem, so long as the full redshift range is sampled. This method is effective even when the two samples do not have similar properties (e.g. differing luminosity and bias).

2.1 INITIAL TEST

To begin I describe a complete end-to-end implementation of cross-correlation methods for calibrating photometric redshifts and present the results of applying these algorithms to realistic mock catalogs. For all calculations in this chapter I assume a flat ΛCDM cosmology with Ω_m=0.3, Ω_Λ=0.7, and Hubble parameter $H_0 = 100h$ km s^{-1} Mpc^{-1}, where we have assumed h=0.72, matching the Millennium simulations, where it is not explicitly included in formulae. In §2.1.1 we describe the catalog and data sets used to test cross-correlation methods. In §2.1.2 we provide a description of the reconstruction techniques used in detail, and in §2.1.3 we provide the results of the calculation. In §2.1.4 we conclude, as well as give a more concise description of the steps taken, providing a recipe for cross-correlation photometric redshift calibration.

2.1.1 Data Sets

To test this method, it is necessary to construct two samples of galaxies, one with known redshift ("spectroscopic") and the other unknown ("photometric"). We have done this using mock DEEP2 Redshift Survey light cones produced by Darren Croton. A total of 24 light cones were constructed by taking lines-of-sight through the Millennium Simulation halo catalog (Lemson & Virgo Consortium, 2006) with the redshift of the simulation cube used increasing with distance from the observer (Kitzbichler & White, 2007). The light cones were then populated with galaxies using a semi-analytic model whose parameters were chosen to reproduce local galaxy properties (Croton et al., 2006). Each light cone covers the range $0.10 < z < 1.5$ and corresponds to a 0.5×2.0 degree region of sky. The galaxies in this mock catalog will have properties (including color, luminosity, and large-scale structure bias) which vary with redshift due to the same factors believed to affect real galaxy evolution. The semi-analytic model used is certainly imperfect, but yields samples of galaxies that pose the same difficulties (e.g. bias evolution and differences in clustering between bright and faint objects) as real surveys will exhibit; they therefore provide a realistic test of our ability to reconstruct redshift distributions of faint samples using spectroscopy of only a brighter

subset.

The spectroscopic sample is generated by selecting 60% of objects with observed R-band magnitude $R < 24.1$, which gives a sample whose characteristics resemble the DEEP2 Galaxy Redshift survey (Newman et al., 2013b). The mean number of spectroscopic objects over the 24 light cones is $35,574$. The size of this sample is comparable to the number of objects predicted to be needed for calibration using template-based methods ($\sim 10^5$ (LSST Science Collaborations: Paul A. Abell et al., 2009; Ma & Bernstein, 2008)). However, this sample differs greatly in what it contains: it consists only of relatively bright objects, rather than having to be a statistically complete sample extending as faint as the objects to which photometric redshifts will be applied (a necessity for accurate training or template development, as the spectral energy distributions of faint galaxies are observed to lie outside the range luminous galaxies cover, both at $z \sim 0$ and $z \sim 1$ (Willmer et al., 2006; MacDonald & Bernstein, 2010). Studies such as Bernstein & Huterer (2010) have assumed for such projections that 99.9% redshift success can be achieved for faint galaxy samples (e.g. of photometric-redshift outliers); however, that is a failure rate more than two orders of magnitude lower than that actually achieved by current large surveys on 10-meter class telescopes such as VVDS (Le Fèvre et al., 2005), ZCOSMOS (Lilly et al., 2007), or DEEP2 (Newman et al., 2013b), surveys which are 1.5-5 magnitudes shallower than the limits of Stage III and Stage IV surveys such as DES and LSST. In contrast, the cross-correlation techniques we focus on here do not require a complete spectroscopic sample, and hence do not require improvements in redshift success over existing projects to provide an accurate calibration.

The other sample, referred to hereafter as the photometric sample, is constructed by selecting objects in the mock catalog down to the faintest magnitudes available, with the probability of inclusion a Gaussian with $\langle z \rangle = 0.75$ and $\sigma_z = 0.20$. This emulates choosing a set of objects which have been placed in a single photometric redshift bin by some algorithm with Gaussian errors. It should be noted that, since the redshift distribution of the mock catalog we select from is not uniform, the resulting redshift distribution of the photometric sample is not a pure Gaussian. The overall redshift distribution of all objects in the catalog is fit well using a 5th degree polynomial, so the net distribution of the photometric sample can be well represented by the product of this polynomial and a Gaussian. After applying

this Gaussian selection to the mock catalog, we then randomly throw out half of the selected objects in order to cut down on calculation time. The mean number of objects in the final photometric sample over the 24 light cones is $44,053$.

The mock catalog includes both the cosmological redshift as well as the observed redshift for each object. The observed redshift shows the effects of redshift-space distortions (Hamilton, 1998), and is the redshift value used for objects in the spectroscopic sample. When plotting the redshift distribution of the photometric sample we use the cosmological redshifts for each object (differences are small). Fig. 2.1 shows the number of galaxies as a function of redshift for each sample, as well as the entire catalog. While there is complete information on the actual redshift distributions for both samples in the catalog, only the distribution of the spectroscopic sample is assumed to be known in our calculations. We assume no information is known about the redshift distribution of the photometric sample, and attempt to recover it using only correlation measurements.

2.1.2 Method

After constructing the two samples of objects from each mock catalog, we can use standard correlation measurements and exploit the clustering of galaxies to recover the redshift distribution of the photometric sample. From here on, the spectroscopic sample, with known observed redshifts, will be labeled "s", and the photometric sample, with redshifts assumed unknown, will be labelled "p".

The most fundamental correlation measurements we use are the real space two-point correlation function and the angular two-point correlation function. The real space two-point correlation function $\xi(r)$ is a measure of the excess probability dP (above that for a random distribution) of finding a galaxy in a volume dV, at a separation r from another galaxy(Peebles, 1980):

$$dP = n[1 + \xi(r)]dV, \tag{2.1}$$

where n is the mean number density of the sample. The angular two-point correlation function $w(\theta)$ is a measure of the excess probability dP of finding a galaxy in a solid angle
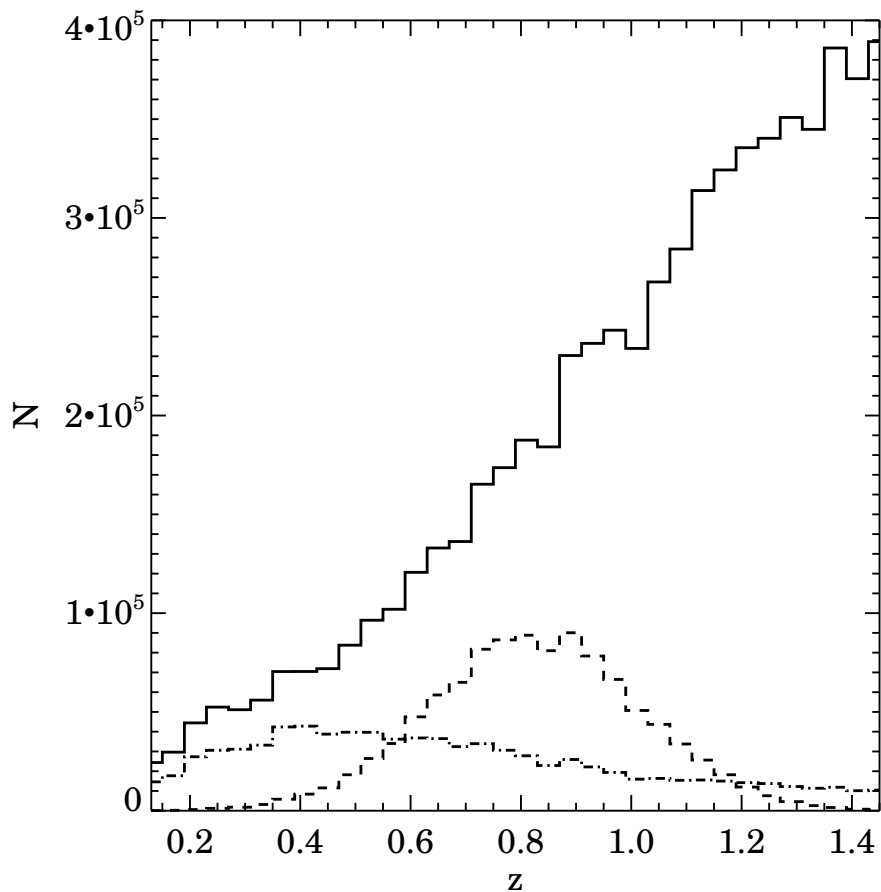
Figure 2.1 The total number of galaxies in each sample as a function of redshift, summed over the 24 fields, binned with $\Delta z = 0.04$. The solid line is the overall redshift distribution for all galaxies in the mock catalogs, the dashed line is the distribution for our photometric sample (selected from the overall sample via a Gaussian in z, emulating objects placed in a single photometric redshift bin), while the dot-dashed line is the redshift distribution for our spectroscopic sample, selected to have magnitude $R < 24.1$.

$d\Omega$, at a separation θ on the sky from another galaxy (Peebles, 1980) :

$$dP = \Sigma[1 + w(\theta)]d\Omega, \tag{2.2}$$

where Σ is the mean number of galaxies per steradian (i.e., the surface density). From the spectroscopic sample we measure the real space two-point autocorrelation function, $\xi_{ss}(r, z)$, and from the photometric sample we measure the angular two-point autocorrelation function, $w_{pp}(\theta)$. These measurements give information about the intrinsic clustering of the samples. We also measure the angular cross-correlation function between the spectroscopic and photometric sample, $w_{sp}(\theta, z)$, as a function of redshift. This is a measure of the excess probability of finding a photometric object at an angular separation θ from a spectroscopic object, completely analogous to w_{pp}.

Modeling $\xi(r)$ as a power law, $\xi(r) = (r/r_0)^{-\gamma}$, which is an accurate assumption from ~ 0.5 to $\sim 20h^{-1}$ comoving Mpc for both observed samples and those in the mock catalogs, we can determine a relation between the angular cross-correlation function $w_{sp}(\theta, z)$ and the redshift distribution. Following the derivation in Newman (2008) (cf. eq. 4),

$$w_{sp}(\theta, z) = \frac{\phi_p(z)H(\gamma_{sp})r_{0,sp}^{\gamma_{sp}}\theta^{1-\gamma_{sp}}D(z)^{1-\gamma_{sp}}}{dl/dz}, \tag{2.3}$$

where $H(\gamma) = \Gamma(1/2)\Gamma((\gamma - 1)/2)/\Gamma(\gamma/2)$ (where $\Gamma(x)$ is the standard Gamma function), $\phi_p(z)$ is the probability distribution function of the redshift of an object in the photometric sample, $D(z)$ is the angular size distance, and $l(z)$ is the comoving distance to redshift z. Hence, to recover $\phi_p(z)$ from w_{sp}, we also must know the basic cosmology (to determine $D(z)$ and dl/dz), as well as the cross-correlation parameters, $r_{0,sp}$ and γ_{sp}. It has been shown that uncertainties in cosmological parameters have minimal effect on the recovery of $\phi_p(z)$(Newman, 2008). To determine the cross-correlation parameters, we use the assumption of linear biasing, under which the cross-correlation is given by the geometric mean of the autocorrelations of the two samples, $\xi_{sp}(r) = (\xi_{ss}\xi_{pp})^{1/2}$. Thus we need to measure the autocorrelation functions for each sample and determine their parameters, r_0 and γ. The derivation of equation 2.3 is shown in more detail in Appendix A.

2.1.2.1 Autocorrelation of the Spectroscopic Sample We first need to determine how the real space autocorrelation function of the spectroscopic sample, ξ_{ss}, evolves with redshift. To do this we bin the spectroscopic objects in redshift and measure the two-point correlation function as a function of projected separation, r_p, and line-of-sight separation, π, for the objects in each bin. However, since it is affected by redshift-space distortions in the line of sight direction, it is difficult to measure the evolution of $\xi_{ss}(r)$ accurately directly from the observed $\xi(r_p, \pi)$. However, as we describe later, we can use $\xi(r_p, \pi)$ to derive the projected correlation function, $w_p(r_p)$, which is not significantly affected by redshift-space distortions. The evolution of the projected correlation function with redshift can be related to the evolution of $\xi(r)$.

To begin we measure ξ_{ss} in bins of r_p and π, using the Landy & Szalay estimator (Landy & Szalay, 1993):

$$\xi = \frac{1}{RR} \left[DD \left(\frac{N_R}{N_D} \right)^2 - 2DR \left(\frac{N_R}{N_D} \right) + RR \right], \tag{2.4}$$

where DD, DR, and RR are the number of object pairs in each bin of r_p and π – i.e., the number of cases where an object of type B is located a separation of r_p and π away from an object of type A – considering pairs between objects in the data catalog and other objects in the data catalog, between the data catalog and a random catalog, or within the random catalog, respectively; we will describe these catalogs in more detail shortly. Here N_D and N_R are the total numbers of objects in the data and random catalogs. For each object pair, we calculated the projected separation, r_p, and the line-of-sight separation, π, using the equations:

$$r_p = D(z_{\mathrm{mean}}) \Delta \theta \tag{2.5}$$

$$\text{and} \quad \pi = |z_1 - z_2| \left. \frac{dl}{dz} \right|_{z_{\mathrm{mean}}}, \tag{2.6}$$

where z_1 and z_2 are the redshifts of the two objects in a pair, $\Delta \theta$ is their angular separation on the sky, and $z_{\mathrm{mean}} = (z_1 + z_2)/2$.

We calculate DD by measuring the transverse and line-of-sight distance between every pair of objects in the data sample and binning those distances to find the number of pairs as a function of r_p and π. In this case the data sample is all of the objects in the chosen

spectroscopic z-bin. In turn, RR is the pair count amongst objects in a "random" catalog, and DR is the cross pair count calculated using pairs between data objects and random catalog objects. We construct the random catalog to have the same shape on the sky as the data catalog, but its objects are randomly distributed with constant number of objects per solid angle (taking into account the spherical geometry).

To measure the real space correlation function, the random catalog must also have the same redshift distribution as the data catalog. To produce this, we first determine a smooth function that fits the overall redshift distribution of the spectroscopic sample and construct the random catalog to match. We had difficulty finding a single function that fit the entire distribution of $R < 24.1$ galaxies in the Millennium mock from $z = 0.1$ to $z = 1.5$, so we used different functional forms over different redshift ranges. The best fit resulted from using $\phi_s(z) \sim z^2 \exp(-z/z_o)$ for $0 < z < 1.03$ and $\phi_s(z) \sim A(1+z)^\beta$ for $z > 1.03$. We bin the objects in each field into bins of $\Delta z = 0.04$. Combining the distributions of all 24 fields and fitting via least-squares gave values of $z_o = 0.232 \pm 0.003$ and $\beta = -2.74 \pm 0.18$. We then used these values, choosing a value of A to force continuity at $z = 1.03$, to define the redshift distribution used to generate the random catalogs. The random catalog for each field contained ~ 10 times the number of objects as its corresponding data catalog.

After constructing the random catalogs, we calculate the pair counts in each redshift bin. For each field, both the data and random catalogs are divided into subsamples ("z-bins") according to their redshift, and DD, DR, and RR are calculated for each bin of r_p and π using only objects within a given z-bin. In the r_p direction we binned the separations in $\log(r_p)$ over the range $-3 < \log(r_p) < 2.5$ with $\Delta \log(r_p) = 0.1$, where r_p is in h^{-1}Mpc. In the π direction we binned the separations over the range $0 < \pi < 30$ h^{-1}Mpc, with $\Delta\pi = 1.0$ h^{-1}Mpc. We calculated the pair counts in 10 z-bins covering the range $0.11 < z < 1.4$, where the size and location of each z-bin was selected so that there were approximately the same number of objects in each one.

When interpreting correlation measurements for the spectroscopic sample, we must take into account the effects of redshift-space distortions (Hamilton, 1998). Since these only affect distance measurements along the line of sight, we integrate $\xi(r_p, \pi)$ in the π direction, which gives the projected correlation function, $w_p(r_p)$. Modeling $\xi(r_p, \pi)$ as a power law and solving

for $w_p(r_p)$ analytically gives

$$w_p(r_p) = 2 \int_0^\infty \xi[(r_p^2 + \pi^2)^{1/2}] d\pi \tag{2.7}$$

$$= r_p \left(\frac{r_0}{r_p}\right)^\gamma H(\gamma), \tag{2.8}$$

where $H(\gamma)$ is defined following equation 2.3. We thus can recover $\gamma_{ss}(z)$ and $r_{0,ss}(z)$ by fitting a power-law model to $w_p(r_p)$ in each z-bin, allowing us to measure how the correlation function evolves with redshift. Because for our field geometry, signal-to-noise is poor at large scales, we fit for $w_p(r_p)$ up to $r_p = 10 \ h^{-1}$Mpc. The lower limit of r_p used for the fit varied with redshift. We found in the highest redshift bins the behavior of $w_p(r_p)$ diverged from a power law, likely due to the semi-analytic model not populating group-mass halos with enough blue galaxies compared to DEEP2 data (Coil et al., 2008). Hence, for $z < 0.8$ we fit over the range $0.1 < r_p < 10 \ h^{-1}$Mpc, while for $z > 0.8$ we fit over $1.0 < r_p < 10 \ h^{-1}$Mpc.

We cannot measure $\xi(r_p, \pi)$ to infinite line-of-sight separations, so to calculate $w_p(r_p)$ we must integrate $\xi(r_p, \pi)$ out to $\pi_{\max} = 30 \ h^{-1}$Mpc and then apply a correction for the fraction of the integral missed. In fact, in measuring $w_p(r_p)$, instead of evaluating $\xi(r_p, \pi)$ and then integrating, we simply summed the paircounts in the π direction so DD, DR, and RR are functions of r_p only; this method yielded more robust results. From equation 2.7 (integrating to $\pi_{\max}$ instead of infinity) we find

$$w_p(r_p) = 2 \left(\frac{1}{RR} \left[DD \left(\frac{N_R}{N_D}\right)^2 - 2DR \left(\frac{N_R}{N_D}\right) + RR \right]\right) \pi_{\max}, \tag{2.9}$$

where DD, DR, and RR are the paircounts summed over the π direction. For the correction, we first calculate $w_p(r_p)$ by summing the pair counts out to $\pi_{\max}$, and then fit for r_0 and γ using the analytic solution given in equation 2.8. Using those parameters, we calculate $\int_0^{\pi_{\max}} \xi(r_p, \pi) d\pi / \int_0^\infty \xi(r_p, \pi) d\pi$. We divide the observed $w_p(r_p)$ by this quantity and refit for r_0 and γ. This process is repeated until convergence is reached.

2.1.2.2 Autocorrelation of the Photometric Sample Since we assume the photometric sample contains no redshift information (or, more realistically, that any available redshift information was already exploited by placing objects into a redshift bin), we determine its autocorrelation parameters by measuring the angular autocorrelation function, $w_{pp}(\theta)$, and relating it to $r_{0,pp}$ using Limber's equation (Peebles, 1980):

$$w_{pp}(\theta) = H(\gamma_{pp})\theta^{1-\gamma_{pp}} \int_0^\infty \phi_p^2(z) r_{0,pp}^{\gamma_{pp}} \frac{D(z)^{1-\gamma_{pp}}}{dl/dz} dz, \tag{2.10}$$

where γ_{pp} may be measured directly from the shape of $w_{pp}(\theta)$. We again measure the angular autocorrelation of the photometric sample using a Landy & Szalay estimator:

$$w_{pp}(\theta) = \frac{1}{RR} \left[DD\left(\frac{N_R}{N_D}\right)^2 - 2DR\left(\frac{N_R}{N_D}\right) + RR \right], \tag{2.11}$$

where DD, DR, and RR are the paircounts as a function of separation, θ, and N_D and N_R are the number of objects in the data and random catalogs for the field. For angular correlation measurements the random catalog consists of objects randomly distributed on the sky in the same shape as the data catalog. Again, the random catalog is ~ 10 times larger than the data catalog. For each sample, we calculated the θ separation of every pair and binned them in $\log(\theta)$ over the range $-3 < \log(\theta) < 0.4$ with $\Delta \log(\theta) = 0.1$, where θ is measured in degrees.

The angular correlation function can be related to the spatial correlation function: $w_{pp}(\theta) = A_{pp}\theta^{1-\gamma_{pp}}$, where $A_{pp} \sim r_{0,pp}^{\gamma_{pp}}$ (Peebles, 1980). However, since the observed mean galaxy density in a field is not necessarily representative of the global mean density, our measurements of $w_{pp}(\theta)$ need to be corrected by an additive factor known as the integral constraint. To estimate this, we fit $w_{pp}(\theta)$ using a power law minus a constant, e.g. $w_{pp}(\theta) = A_{pp}\theta^{1-\gamma_{pp}} - C_{pp}$, where C_{pp} is the integral constraint. For measuring the parameters we fit over the range $0.001° < \theta < 0.1°$. We found that fitting over this smaller range reduced the error in the amplitude measurements, although the error in the integral constraint (which is essentially a nuisance parameter) increases. For autocorrelation measurements this has little impact. We use the measured γ_{pp}, along with the parameters of the spectroscopic sample ($\gamma_{ss}(z)$ and $r_{0,ss}(z)$) and an initial guess of $r_{0,pp}$ to determine an initial guess of $r_{0,sp}^{\gamma_{sp}}$, employing the linear biasing assumption that $r_{0,sp}^{\gamma_{sp}} = (r_{0,ss}^{\gamma_{ss}} r_{0,pp}^{\gamma_{pp}})^{1/2}$.

We expect the correlation length of the photometric sample, $r_{0,pp}$, to be a function of redshift, as both the underlying dark matter correlation function and the large-scale structure bias of the sample will evolve with z, both in the real universe and in our mock catalogs. To account for this, we assume the redshift dependence of the scale length, r_0, will be similar for both the photometric and spectroscopic samples (we considered several alternatives, but this yielded the best results); for our calculations we set $r_{0,pp}(z) \propto r_{0,ss}(z)$, with an initial guess of $r_{0,pp}(z) = r_{0,ss}(z)$. We then refine our initial guess for $r_{0,sp}^{\gamma_{sp}}$ by measuring the angular cross-correlation function in each redshift bin.

2.1.2.3 Cross-correlation and the Redshift Distribution

To find $w_{sp}(\theta, z)$, we measure the cross-correlation between objects in spectroscopic z-bins with all objects in the photometric sample. We bin the spectroscopic sample over the range $0.19 < z < 1.39$ with a bin size of $\Delta z = 0.04$ and measure $w_{sp}(\theta)$ for each bin using the estimator

$$w_{sp}(\theta) = \frac{1}{R_s R_p} \left[D_s D_p \left(\frac{N_{R_s} N_{R_p}}{N_{D_s} N_{D_p}} \right) - D_s R_p \left(\frac{N_{R_s}}{N_{D_s}} \right) - R_s D_p \left(\frac{N_{R_p}}{N_{D_p}} \right) + R_s R_p \right], \quad (2.12)$$

where $D_s D_p$, $D_s R_p$, $R_s D_p$, and $R_s R_p$ are the cross pair counts between samples as a function of θ separation, and N is the number of objects in each sample. The cross pair counts are calculated by measuring the observed number of objects from one sample around each object in another sample. For example, $D_s D_p$ is the number of objects in the photometric sample around each spectroscopic object as a function of separation. For this measurement, each sample (the objects in the spec-z bin and the photometric sample) has their own random catalog that is ~ 10 times bigger than their corresponding data catalog. These are once again constructed by randomly distributing objects on the sky in the same shape as the data catalog.

For each z-bin we measured $w_{sp}(\theta)$ in logarithmic bins of 0.1 in $\log(\theta)$ over the range $-3 < \log(\theta) < 0.4$, with θ measured in degrees. As with the autocorrelation function, we fit $w_{sp}(\theta) = A_{sp}\theta^{1-\gamma_{sp}} - C_{sp}$; the integral constraint is nonnegligible in these measurements. Again we fit over the range $0.001° < \theta < 0.1°$ to reduce the error in the amplitude measurements. In some z-bins, particularly where the amplitude, A_{sp}, is small, we found a significant degeneracy between A_{sp} and γ_{sp} when fitting. One can understand this as there being a pivot

16

scale at which clustering is best constrained; one can simultaneously vary A_{sp} and γ_{sp} and still match w_{sp} at that scale. To remove this degeneracy, we fixed γ_{sp} in each bin, and only fit for the amplitude and integral constraint. Since the clustering of the samples with each other is expected to be intermediate to the intrinsic clustering of each sample, we estimated γ_{sp} with the arithmetic mean of γ_{pp} and γ_{ss}. Using A_{sp} and γ_{sp}, as well as the initial guess for $r_{0,sp}^{\gamma_{sp}}$, we determine an initial guess of the redshift distribution $\phi_p(z)$. Rewriting equation 2.3 gives

$$\phi_p(z) = \frac{dl/dz}{D(z)^{1-\gamma_{sp}} H(\gamma_{sp}) r_{0,sp}^{\gamma_{sp}}} A_{sp}(z). \tag{2.13}$$

We then use the resulting $\phi_p(z)$, along with A_{pp} and γ_{pp}, to redetermine $r_{0,pp}$ using Equation 2.10, which we use to redetermine $r_{0,sp}^{\gamma_{sp}}$ and thus $\phi_p(z)$. This process is repeated until convergence is reached.

2.1.3 Results

For the remainder of this chapter, we will frequently refer to making a "measurement" of the correlation functions and $\phi_p(z)$. Each measurement is done by selecting four fields at random out of the 24 mock catalogs, summing their pair counts, and calculating all necessary quantities; no information on "universal" mean values of any measured quantity is used, but rather only that available from the chosen four fields. We select four fields in order to emulate redshift surveys like DEEP2 and VVDS, in which data is typically obtained from of order four separate fields; hence a "measurement" in our parlance is roughly equivalent to utilizing the information coming from a single survey. To obtain the following results, we made 10^4 measurements; we used the median values to evaluate statistical biases in a given quantity and the standard deviation to evaluate random uncertainties. In each plot following the points are the median values and the error bars are the standard deviations, which gives the error on a single measurement. Because (given the large number of measurements) these medians should closely match the mean of the 24 fields, the standard error in a plotted point should be smaller than the plotted error bars by a factor of $\sqrt{6}$.

It should be noted that we are ignoring the weak cross correlation that should result from gravitational lensing by large-scale structure (Newman, 2008; Bernstein & Huterer, 2010).

These correlations can be predicted directly from galaxy number counts (Scranton et al., 2005); planned surveys such as LSST will extend fainter than their nominal depth over limited regions of sky (LSST Science Collaborations: Paul A. Abell et al., 2009), so no extrapolation will be required. It should also be possible to use the initial estimate of $\phi_p(z)$ to predict the lensing induced cross-correlation signal at a given redshift, and therefore iteratively remove its contribution. Because these correlation effects are weak, straightforward to deal with, and not present in the mock catalogs available to us, we do not consider them further for this test of the technique. However a more detailed analysis of this contribution to the cross-correlation signal is presented in §2.3.

To determine the evolution of the autocorrelation parameters of the spectroscopic sample we measured $w_p(r_p)$ in z-bins of varying widths. Fig. 2.2 shows the median and standard deviation of $w_p(r_p)$ for 10^4 measurements in each spectroscopic z-bin, with the correction for finite π_{max} applied as described above. We then fit each measurement of $w_p(r_p)$ for the autocorrelation parameters. The solid lines in Fig. 2.2 show the results of equation 2.8 corresponding to the median $r_{0,ss}$ and γ_{ss} for all measurements in a given z-bin, while Fig. 2.3 shows the accuracy with which we can measure the evolution of $r_{0,ss}$ and γ_{ss} with redshift. Both parameters decreasing with redshift is consistent with measurements in real samples which show bluer galaxy samples have smaller r_0 and γ (Coil et al., 2008); a constant observed magnitude limit will correspond to a selection at a bluer and bluer rest frame band as redshift goes up, increasingly favoring bluer objects for selection.

The autocorrelation parameters for the photometric sample are determined from the shape of $w_{pp}(\theta)$. Fig. 2.4 shows the median and standard deviation of 10^4 measurements of $w_{pp}(\theta)$, corrected for the integral constraint. A fit to each measurement gives estimates of autocorrelation parameters. Taking the median values and standard deviations gives $A_{pp} = 5.48 \times 10^{-4} \pm 2.73 \times 10^{-4}$ and $\gamma_{pp} = 1.55 \pm 0.045$. The solid line in Fig. 2.4 corresponds to these median values. The scale length of the photometric sample, $r_{0,pp}(z)$, was assumed to be proportional to $r_{0,ss}(z)$; this yielded superior results to other simple assumptions. The proportionality constant may then be found using an initial guess of $r_{0,pp} = r_{0,ss}$ to calculate $\phi_p(z)$ using cross-correlation techniques, leading to a refined estimate of $r_{0,pp}$ using Limber's equation (eqn. 2.10). That refined $r_{0,pp}$ is then used to make an improved measurement of
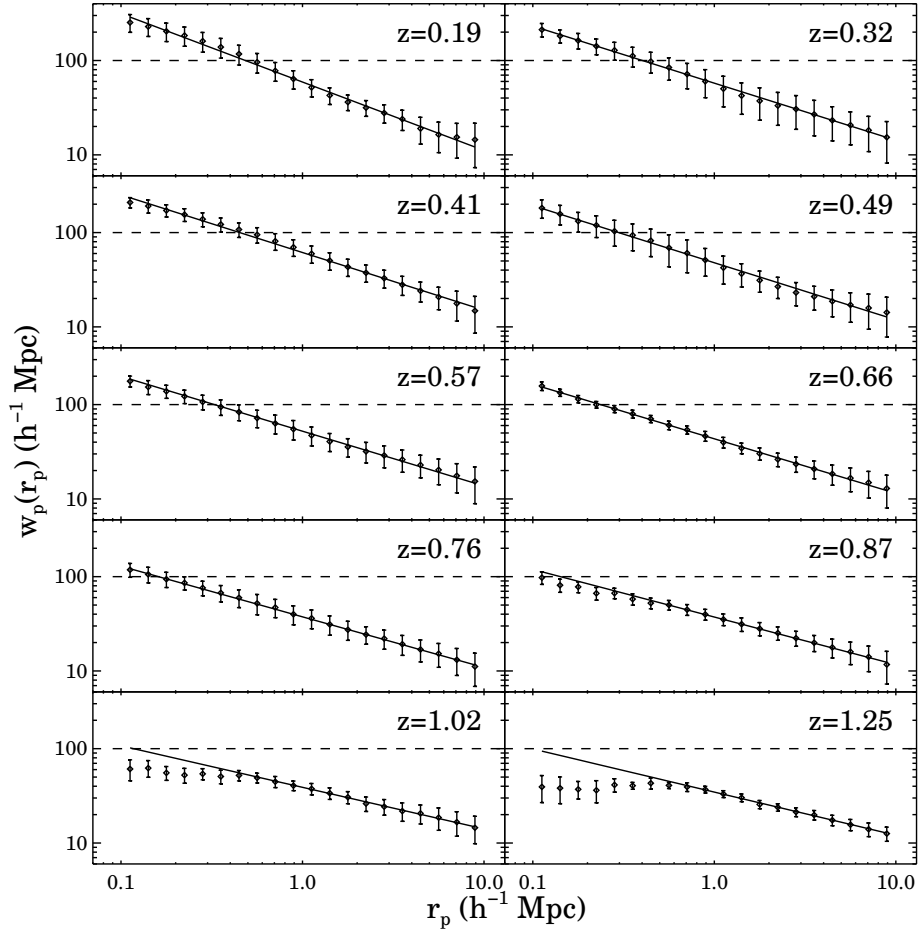
Figure 2.2 The median value of 10^4 measurements of the projected two-point correlation function of the spectroscopic sample, $w_p(r_p)$, in each redshift bin. Each measurement is made by averaging the paircounts of four fields selected at random from the 24 total fields. Error bars show the standard deviation of the measurements; i.e., they indicate the expected errors from a spectroscopic survey of four 1 square degree fields. The standard error in the plotted points is smaller than these error bars by a factor of $\sqrt{6}$ (2.45). At high redshift $w_p(r_p)$ deviates from a power law, whereas observed samples do not, due to the semi-analytic model not containing enough blue galaxies in group-mass halos. The solid line depicts a power-law model for $w_p(r_p)$, using the median values of the fit parameters $r_{0,ss}$ and γ_{ss} across the 10^4 measurements. The dashed line is the same in all panels; it is included to help make changes in the slope (i.e., γ_{ss}) and the amplitude (i.e., $r_{0,ss}$) with redshift clearer. We can see that changes in the amplitude with redshift are much more significant than changes in the slope.
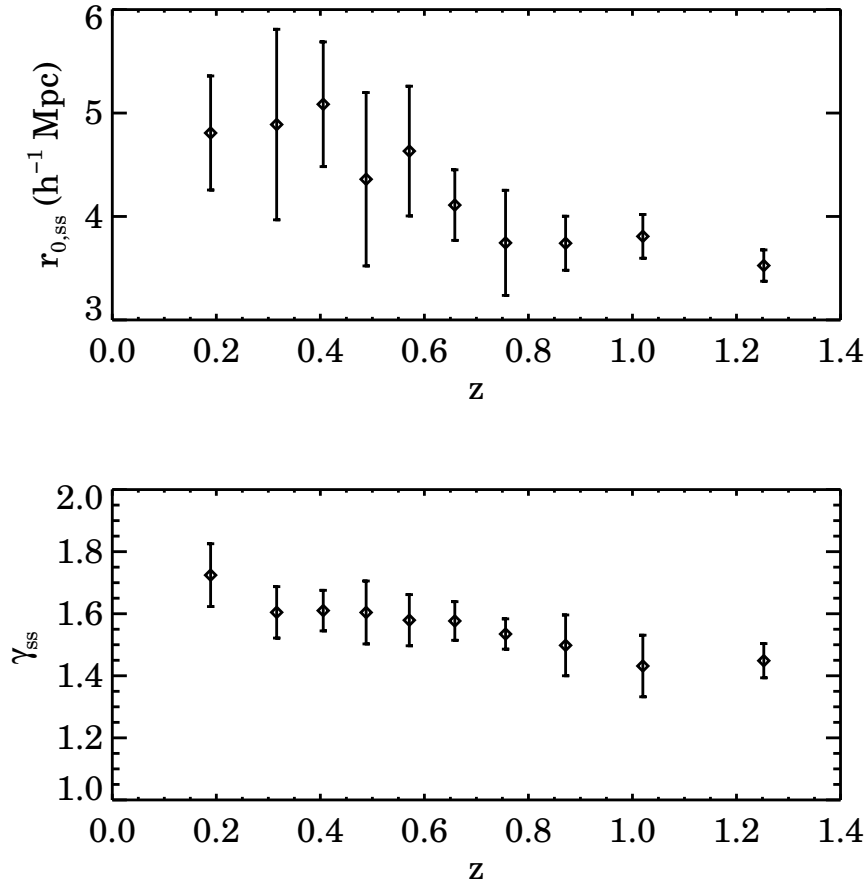
Figure 2.3 The correlation function parameters resulting from power-law fits to $w_p(r_p)$, $r_{0,ss}$ and γ_{ss}, as a function of redshift. The points are the median values of 10^4 measurements, and hence correspond to the parameters used to generate the lines in Fig. 2.2; the error bars are the standard deviation of each parameter amongst the measurements. The standard error in the plotted points is smaller than these error bars by a factor of $\sqrt{6}$ (2.45). Each measurement is made by averaging the paircounts of four fields selected at random from the 24 total fields. While both parameters decrease with redshift, we see that changes in $r_{0,ss}$ are substantially greater than changes in γ_{ss}.
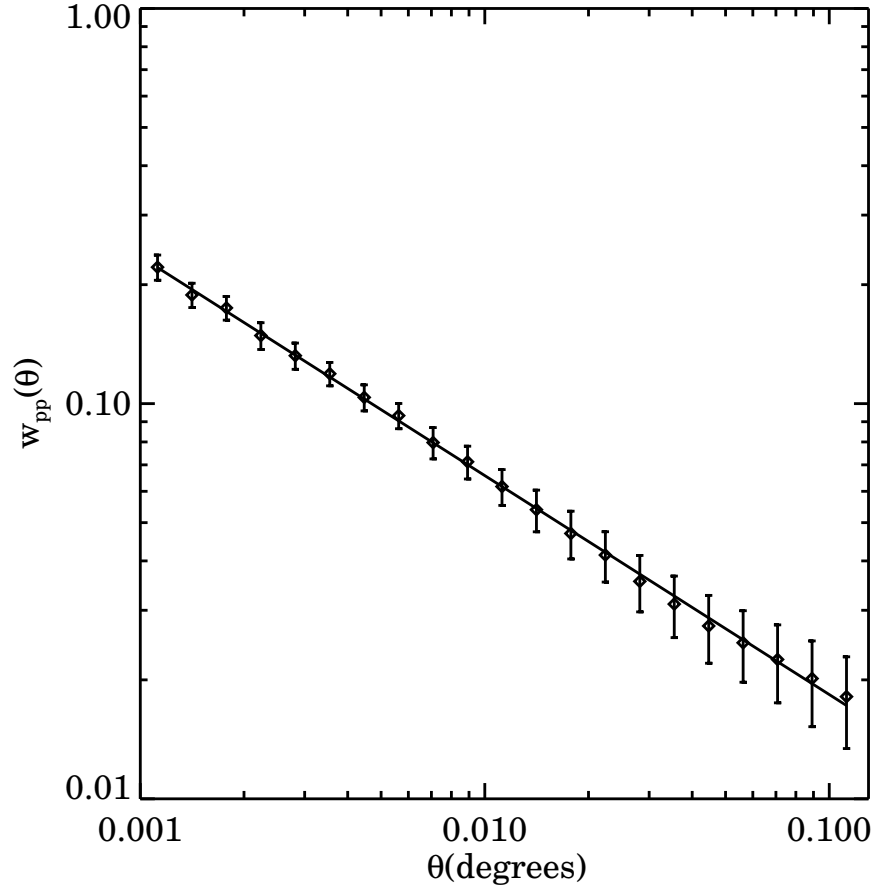
Figure 2.4 The median value of 10^4 measurements of the two-point correlation function of the photometric sample, $w_{pp}(\theta)$, corrected for the integral constraint. Each measurement is made by averaging the paircounts of four fields selected at random from the 24 mock catalogs. Error bars show the standard deviation of the measurements. The standard error in the plotted points is smaller than these error bars by a factor of $\sqrt{6}$ (2.45). The solid line is the fit to $w_{pp}(\theta)$ using the median values of the fit parameters A_{pp} and γ_{pp}; a power-law model provides an excellent fit to the data.

$\phi_p(z)$, which is used to obtain a yet-improved measure of $r_{0,pp}$, etc. After convergence was reached, we found that on average $r_{0,pp}/r_{0,ss} = 1.068$.

To determine the evolution of the cross-correlation parameters, we measure the angular cross-correlation, $w_{sp}(\theta, z)$, between objects in successive spectroscopic z-bins and the photometric sample. Fig. 2.5 shows the median and standard deviation of $w_{sp}(\theta)$ for 10^4 measurements in each z-bin, corrected for the integral constraint. Fitting each measurement for the cross-correlation parameters with fixed γ_{sp} as described above and taking the median gives the amplitude, $A_{sp}(z)$, shown in Fig. 2.6. The solid lines in Fig. 2.5 correspond to the median of the best-fit parameters from each measurement.

Combining the intrinsic clustering information from the autocorrelation parameters of each sample with the amplitude of the cross-correlation, $A_{sp}(z)$, together with the basic cosmology, gives the recovered redshift distribution. We found that a linear fit of $r_{0,ss}$ and γ_{ss} versus z resulted in a better recovery of $\phi_p(z)$ than using each bin's value directly, resulting in a $\sim 32\%$ reduction in the χ^2 of the final reconstruction as compared to the true redshift distribution. Fitting the correlation function over a limited θ range, as described in § 2.1.2.3, reduced the measured error in $\phi_p(z)$ for each z-bin by $\sim 25\%$ on average, reducing the χ^2 in comparing the reconstructed and true redshift distributions by $\sim 30\%$. We also tried modeling γ_{sp} as constant with z using the arithmetic mean of $\gamma_{ss}(z = 0.77)$ and γ_{pp}. This resulted in a $\sim 20\%$ increase in the χ^2 of the final fit.

Fig. 2.7 shows the median and standard deviation of 10^4 measurements of $\phi_p(z)$ compared to the actual distribution. To determine the actual distribution, we found the mean true distribution of the four fields corresponding to each measurement and took the median across the 10^4 measurements; this should accurately match the true mean of the redshift distributions over the 24 fields. Each measurement was normalized so that integrating $\phi_p(z)$ over the measured redshift range gives unity before the median was taken. It is important to note that the reconstruction techniques we have implemented thus far will recover the actual redshift distribution of objects in the photometric sample. This will in general deviate from the true, universal redshift distribution of objects of that type due to sample/cosmic variance. We describe and test methods for recovering the underlying universal distribution in §2.1.3.2.
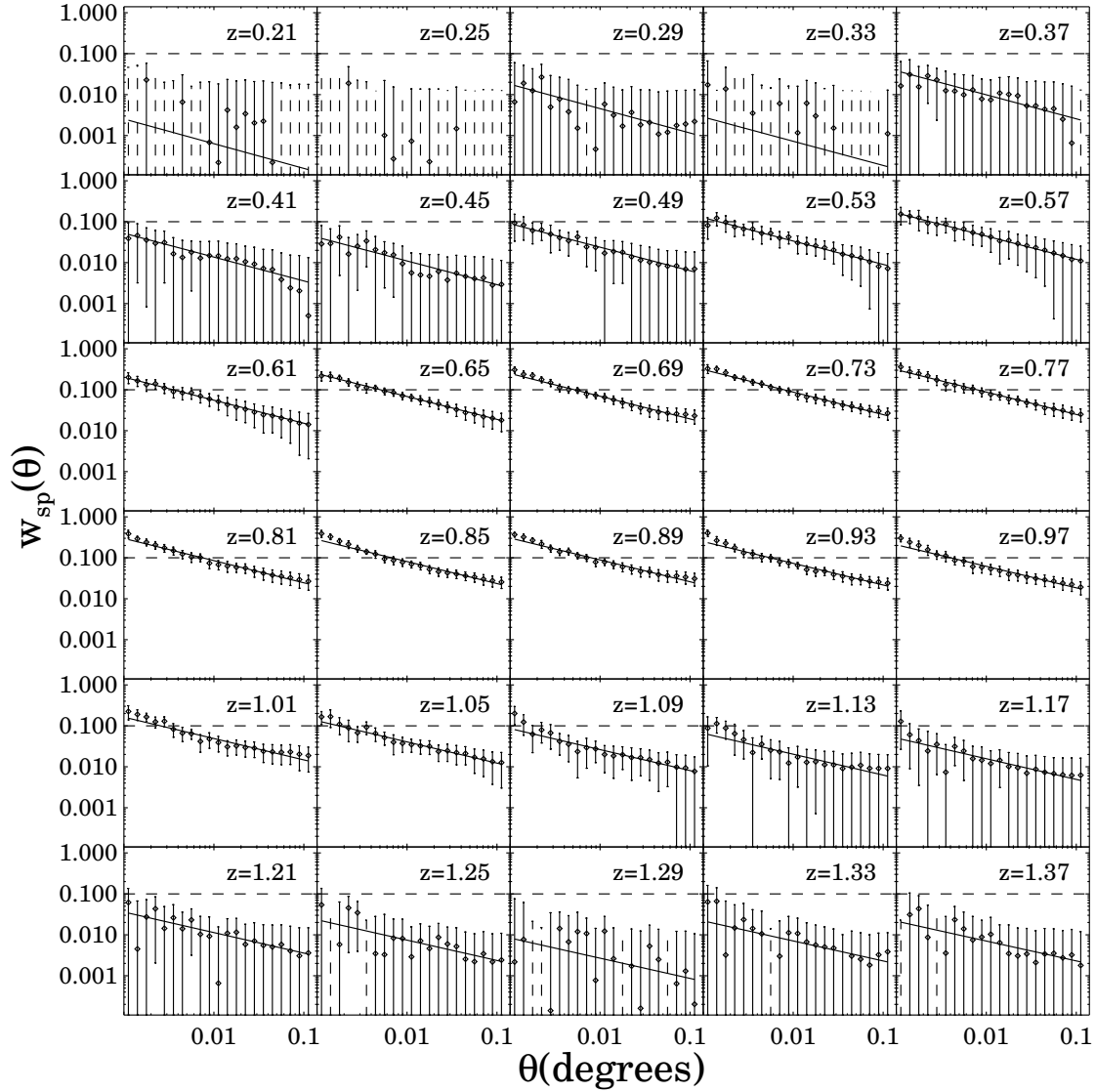
Figure 2.5 The median value of 10^4 measurements of the cross-correlation between the photometric and spectroscopic samples, $w_{sp}(\theta)$, in each redshift bin, corrected for the integral constraint. Each measurement is made by averaging the paircounts of four fields selected at random from the 24 total fields. Error bars show the standard deviation of the measurements. The standard error in the plotted points is smaller than these error bars by a factor of $\sqrt{6}$ (2.45). The solid line is the fit to $w_{sp}(\theta)$ using the median values of the fit parameters A_{sp} and γ_{sp}. The dashed line is to help make changes in the amplitude, $A_{sp}(z)$, with redshift clearer; in the fits shown the slope, $\gamma_{sp}(z)$, is forced to be constant with z. It is clear that the amplitude of the correlation is much greater in the central region of the redshift range where there are more photometric objects.
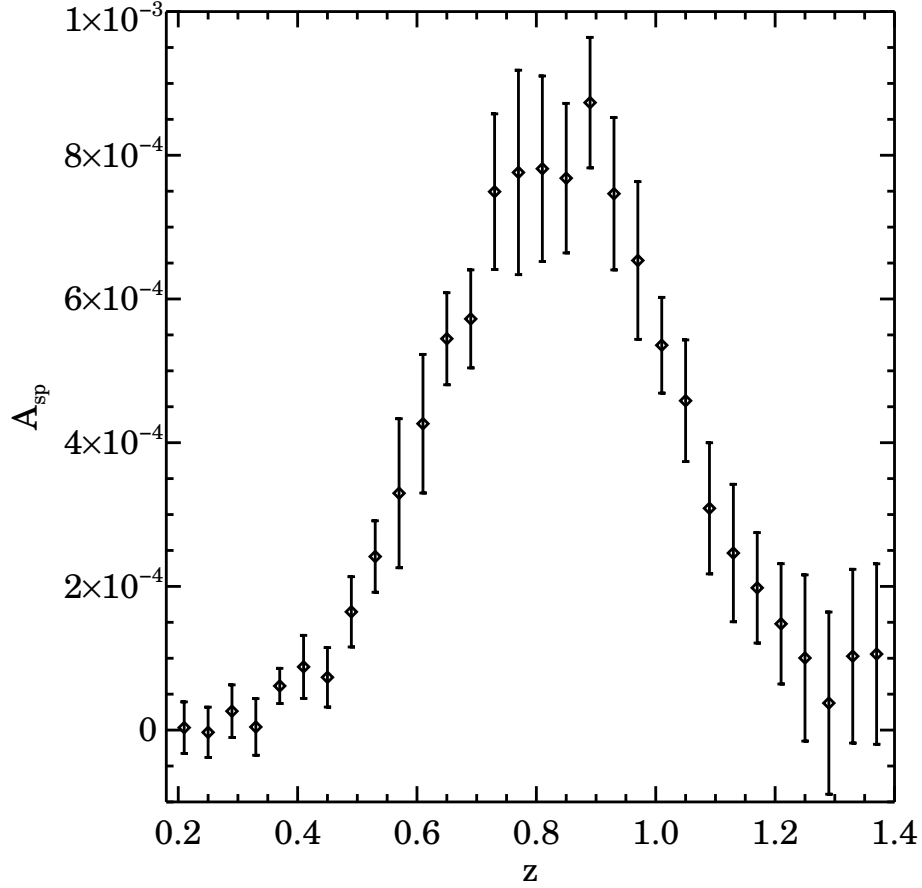
Figure 2.6 The median value of 10^4 measurements of A_{sp}, the amplitude of w_{sp}, in each redshift bin. Each plotted point corresponds to the amplitude of one of the model lines shown in Fig. 2.5. Each measurement is made by averaging the paircounts of four fields selected at random from the 24 mock catalogs. Error bars show the standard deviation of the measurements. The standard error in the plotted points is smaller than these error bars by a factor of $\sqrt{6}$ (2.45). The amplitude is larger in the central region of the redshift range where there are more photometric objects, which is expected since the degree to which the two samples overlap in redshift contributes to the strength of the cross-correlation function.
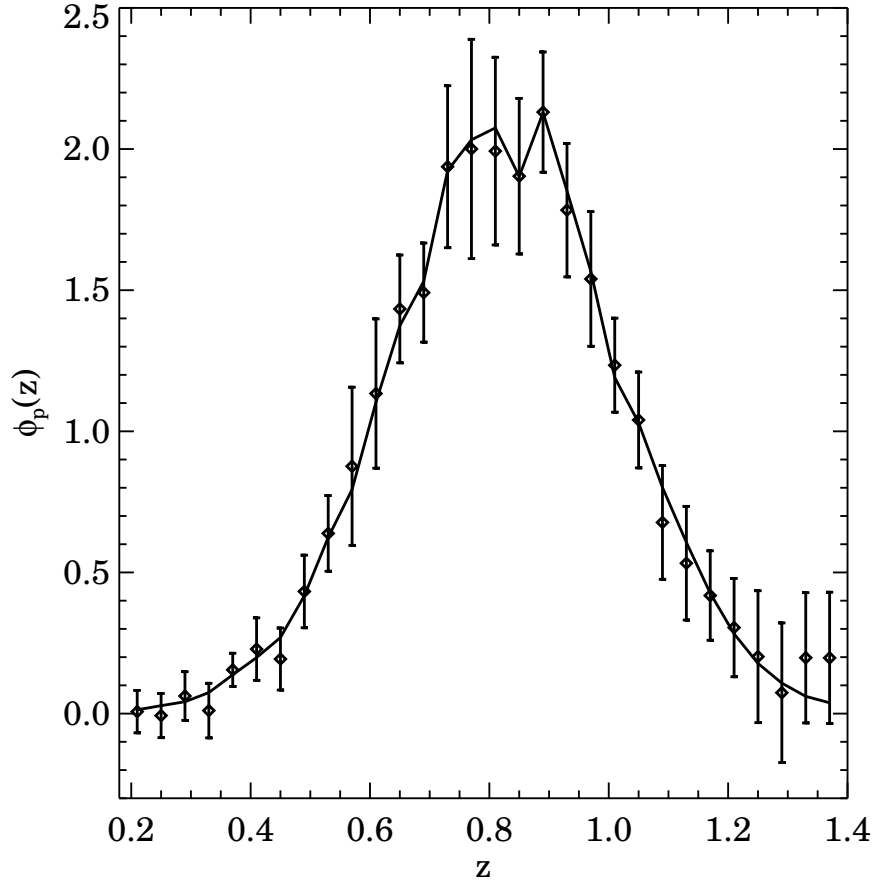
Figure 2.7 Plot of the redshift distribution recovered using cross-correlation techniques. The solid line is the actual distribution of the photometric sample (combining all 24 fields), while the points are the median reconstructed values from 10^4 measurements. Error bars show the standard deviation of the recovered distribution when performing cross-correlation reconstruction in 4 0.5×2 deg fields, emulating the data available from existing deep redshift surveys. The standard error in the plotted points is smaller than these error bars by a factor of $\sqrt{6}$ (2.45). Each measurement is made by averaging the paircounts of four fields selected at random from the 24 mock catalogs. The recovered distribution follows the true distribution closely, even picking up the irregular dip due to sample variance (also known as cosmic variance) at the peak.

We also looked at how well redshift distributions may be recovered in a single, 1 square degree field. For each field, the correlation functions were calculated using only the information from that field. To weight each bin when fitting for correlation-function parameters, the fit was calculated using errors given by the standard deviation of the correlation function in each θ bin over the 24 fields. This mimics the common situation where we have few fields with data and errors are determined from simulations. For a single field, a linear fit for the evolution of the spectroscopic-sample correlation function parameters was not a good model, so we used the calculated parameters in each z-bin. Fig. 2.8 shows the recovered distribution, $\phi_p(z)$, in each of the 24 fields, compared to the true redshift distribution of the photometric sample in that field.

2.1.3.1 Correlation Measurement Errors In the course of our calculation of the redshift distribution, we found that the error in $\phi_p(z)$ for each redshift bin was larger than expected from the error model used in Newman (2008), which uses the standard, classical weak-clustering formalism. This formalism predicts that Poisson uncertainties should dominate when the clustering strength (e.g. the value of w_{sp}) is small compared to unity (Peebles, 1980). Upon further investigation we determined that the error in all correlation function measurements were larger than expected according to this model, which led to the excess error in $\phi_p(z)$. This additional error is associated with extra variance terms identified by Bernstein (1994), which contribute significantly even in the weak-clustering limit, contrary to the classical assumption. These extra terms are dominated by the variance in the integral constraint, which has a significant impact if spectroscopic samples cover only a few square degrees of sky.

Fig. 2.9 compares the four terms of the predicted error from Bernstein's error model to our measured error for $w_{pp}(\theta)$. Bernstein's error model assumes the separation is much smaller than the field size, so we see for small θ the predicted variance does follow our measured variance closely, and then deviates as the separation becomes comparable to the field size. The integral constraint term dominates at large θ values. In order to calculate some of the variance terms of Bernstein's model we required values for q_3 and q_4, which are used to relate the three- and four-point correlation functions to the two-point correlation
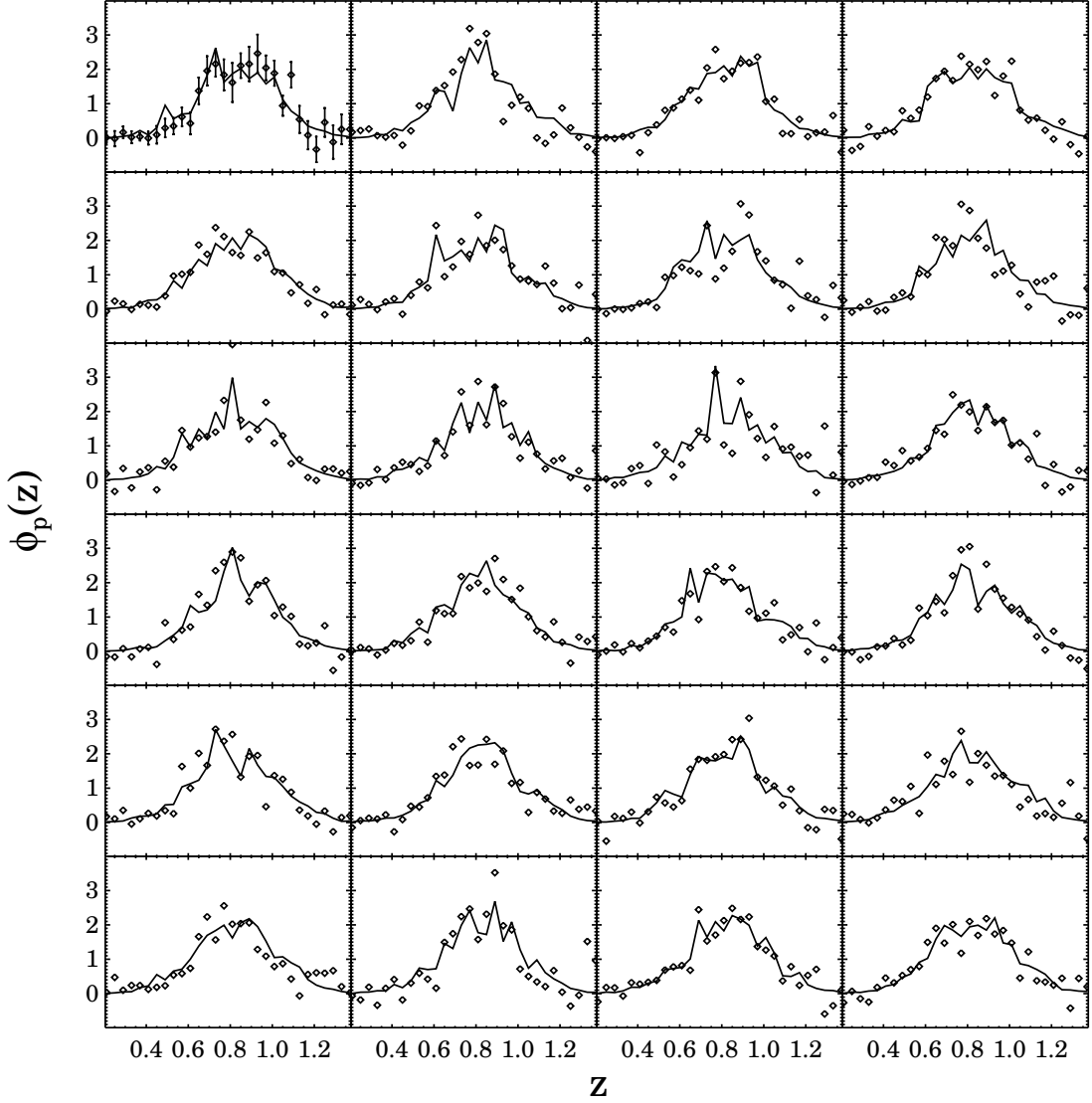
Figure 2.8 Plot of the recovered redshift distribution for each of the 24 fields, using only pair counts from a single field in the reconstruction. The error bars in the first plot are the standard deviation of $\phi_{p,\mathrm{rec}}(z) - \phi_{p,\mathrm{act}}(z)$ amongst the 24 fields; they should be representative of the expected error for each panel. For each field, all errors used in fitting are based on standard deviations across the 24 fields. This mimics a common situation where we have only one field, but use errors determined from simulations to weight points for fitting. The reconstruction generally captures the variation amongst fields due to sample/cosmic variance.
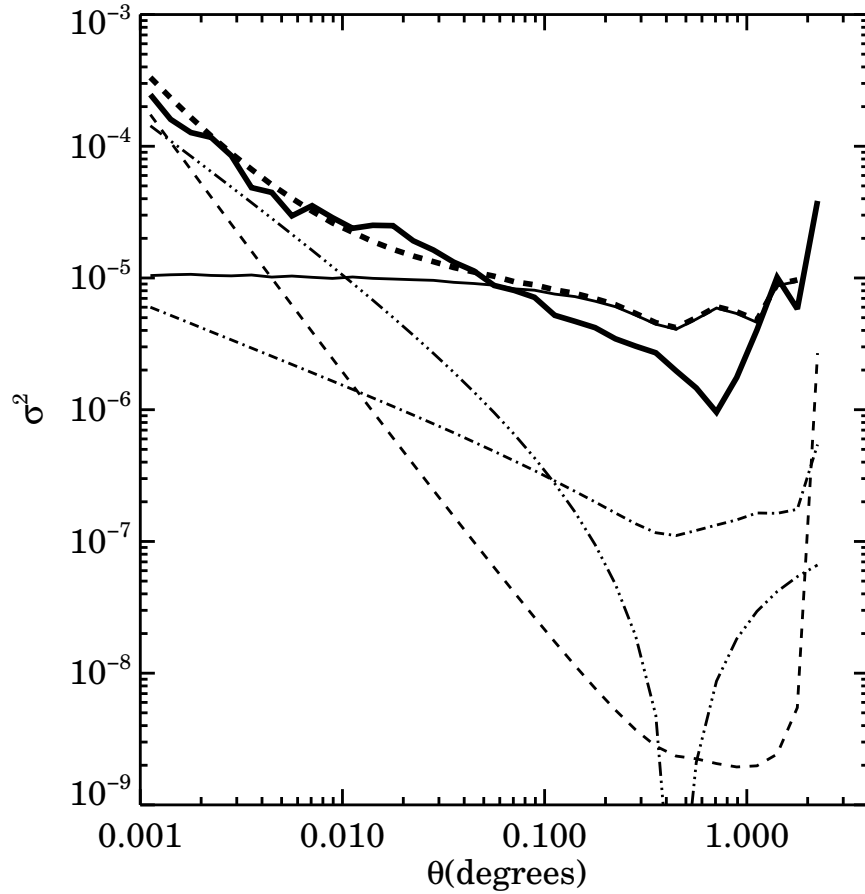
Figure 2.9 The variance of 10^4 measurements of the autocorrelation of the photometric sample, $w_{pp}(\theta)$ (thick solid line), compared to predicted error terms from Bernstein 1994. The thick dashed line shows the sum of all the variance terms; it corresponds well to the observed variance save at the largest scales, where the Bernstein 1994 model is overly conservative (a consequence of the assumption made in that work that the angular separations considered are significantly smaller than the size of the field). From equation 38 in Bernstein (1994), the thin solid black line is the term that scales as w^2, corresponding to the variance in the integral constraint, which dominates at large θ. The thin three-dot-dash line is the term that scales at w^3, and the thin dot-dash line is the term that scales as $1/N$. The thin dashed black line is the term that scales as $1/N^2$ and is comparable to the Poisson error, which dominates in the weak clustering formalism used by Newman (2008). The "observed" variance in $w_{pp}(\theta)$ is much larger than the weak clustering prediction; the same is true of $w_{sp}(\theta)$, although to a lesser degree.

function assuming hierarchical clustering. For this we used the values measured by Bernstein in simulation catalogs, $q_3 = 0.32$ and $q_4 = 0.1$ (Bernstein, 1994). This gave a better fit to our results than the values observed in local galaxy samples (Meiksin et al., 1992; Szapudi et al., 1992).

From Fig. 2.9 we see that the measured variance can be orders of magnitude larger than errors predicted using the weak-clustering assumption (though the difference is a smaller factor for w_{sp}, whose errors dominate in reconstructing $\phi_p(z)$). This excess variance will have a significant impact on the error budgets of planned dark energy experiments (see the next section for quantitative estimates); it is dominated by the variance in the integral constraint, whose effect increases with decreasing field size, so errors may be greatly reduced by surveying galaxies over a larger area ($> \sim 100$ square degrees instead of ~ 4). For instance, the proposed BigBOSS survey (Schlegel et al., 2011) would provide a near-ideal sample for cross-correlation measurements (using both galaxies and Lyman α absorption systems at redshifts up to ~ 3). We may also reduce this effect by using better correlation function estimators which reduce the effect of the integral constraint.

2.1.3.2 Error Estimates In this subsection, we investigate the impact of these excess correlation function measurement errors on our ability to recover the parameters (i.e. the mean and σ) of the true redshift distribution for the photometric sample, and compare the results to Monte Carlo tests done in Newman (2008). For each measurement we have a recovered distribution and an associated true distribution for that set of four fields. We will test the recovery both of the underlying, universal distribution used to construct the photometric sample (i.e. $\langle z \rangle = 0.75$, $\sigma_z = 0.20$) and of the actual redshift distribution of the objects selected in a given set of fields (which will differ due to sample/cosmic variance; cf. §2.1.3).

Before we can fit for Gaussian parameters, we must account for the fact that our photometric sample has a redshift distribution which differs from a true Gaussian because the total sample we drew from (with Gaussian probability as a function of z) was not uniformly distributed in redshift. One can think of the actual distribution of the photometric sample in a given bin as a product of three factors: the overall redshift distribution of all objects

in the Universe (essentially, the rising curve in 2.1); the fractional deviation from the Universal mean of the number of objects in a given field at a given redshift, i.e. sample/cosmic variance; and the Gaussian function used to select objects for the photometric redshift bin.

The first two factors need to be removed from both the true and recovered distributions if we are to test the recovery of the third; this is implemented differently for each case. For the true distribution, we divide each measurement by the overall dN/dz of all of the objects in the four fields used in that measurement. This removes the overall distribution shape as well as the fluctuations due to sample variance, and gives a true distribution that closely matches the Gaussian selection function applied to construct the sample.

In principle we could do the same for the recovered distribution, but that would not be practical in real applications, as we can determine the overall shape of the redshift distribution of the overall photometric sample using photometric redshifts, but photo-z errors will prevent measuring fluctuations in the number of objects within bins of small Δz. Hence, we correct the recovered $\phi_p(z)$ using a low-order polynomial fit to the shape of the overall sample's dN/dz, but use the fluctuations (compared to a smooth fit) in the observed redshift distribution of the spectroscopic sample dN_s/dz, which will be known from the same observations used to perform cross-correlation measurements, to correct for sample variance. This correction assumes that deviations from the mean in both samples behave similarly with redshift; we might expect their amplitude to scale with the large-scale-structure bias of a given sample, but we do not apply any correction for that here. In tests, we have found that a correction using fluctuations in dN_s/dz was as effective in constraining parameters as one based on fluctuations in the dN/dz of the overall sample our photometric subsample was selected from, and so we focus on the former, more realistic technique.

In more detail, we first divided the recovered distribution by a smooth fit (using a 5th-degree polynomial function) to the overall dN/dz of the entire simulation averaged over all 24 fields. This eliminates gradients associated with the shape of the parent sample's overall redshift distribution without removing deviations due to sample variance. To correct for the latter, we need to quantify the fluctuations in the spectroscopic sample relative to a mean distribution. For this smooth, mean distribution, $\langle dN_s/dz \rangle$, we used the same fit to the redshift distribution of the spectroscopic sample averaged over all 24 fields which

was employed to construct the random catalogs for autocorrelation measurements (§2.1.2.1). Using a fit to a given set of four fields would make little difference, as the deviation from the smooth fit at a given redshift bin due to sample variance are much larger than the deviations between the smooth fit to 4 or 24 fields. We then calculate the ratio $dN_s/dz/\langle dN_s/dz \rangle$, where dN_s/dz is the redshift distribution of the spectroscopic sample averaged over the four fields used in that measurement, and correct for sample variance by dividing each measurement of $\phi_p(z)$ by this quantity.

After applying these corrections to each distribution, each measurement is normalized so that their integral is unity, and then fit for $\langle z \rangle$ and σ_z using a normalized Gaussian fitting function. Fig. 2.10 shows the median and standard deviation of 10^4 measurements of the recovered $\phi_p(z)$ before and after correcting for sample variance. In both plots the fit to the overall dN/dz is divided out. It is clear to the eye that the distribution corrected for sample variance is a better fit to the underlying selection function; more quantitatively, it reduces errors in determining the parameters of the Gaussian selection function by $\sim 10\%$.

We assess the reconstruction of the photometric sample in two ways. First, we compare the reconstructed parameters, $\langle z \rangle$ and σ_z, of the Gaussian selection function to the true values, known by construction. Second, we compare the reconstructed parameters of the selection function to the parameters of a Gaussian fit to the actual normalized distribution of each set of four fields used. The latter method should be more robust to systematic errors in the "true" dN/dz we divide each measurement by.

For the first test, where $\langle z \rangle_{\text{true}} = 0.75$ and $\sigma_{z,\text{true}} = 0.20$, we find $\langle \langle z \rangle_{\text{rec}} - \langle z \rangle_{\text{true}} \rangle = 7.796 \times 10^{-4} \pm 7.415 \times 10^{-3}$ and $\langle \sigma_{z,\text{rec}} - \sigma_{z,\text{true}} \rangle = 8.140 \times 10^{-4} \pm 8.545 \times 10^{-3}$, where as usual the values given are the median and standard deviation of all measurements, respectively. The second test, where $\langle z \rangle_{\text{true}}$ and $\sigma_{z,\text{true}}$ are determined by a Gaussian fit to the true distribution of each measurement, we find $\langle \langle z \rangle_{\text{rec}} - \langle z \rangle_{\text{true}} \rangle = 7.259 \times 10^{-4} \pm 7.465 \times 10^{-3}$ and $\langle \sigma_{z,\text{rec}} - \sigma_{z,\text{true}} \rangle = 4.724 \times 10^{-4} \pm 8.546 \times 10^{-3}$. In all cases, the bias is not statistically significant (the standard error against which each bias estimate must be compared is smaller than the quoted standard deviations by a factor of $\sqrt{6}$), but in any event the overall bias of both parameters is considerably smaller than the associated random errors, and will therefore have little effect when added in quadrature. These errors are still larger than the estimated

(a)   (b)
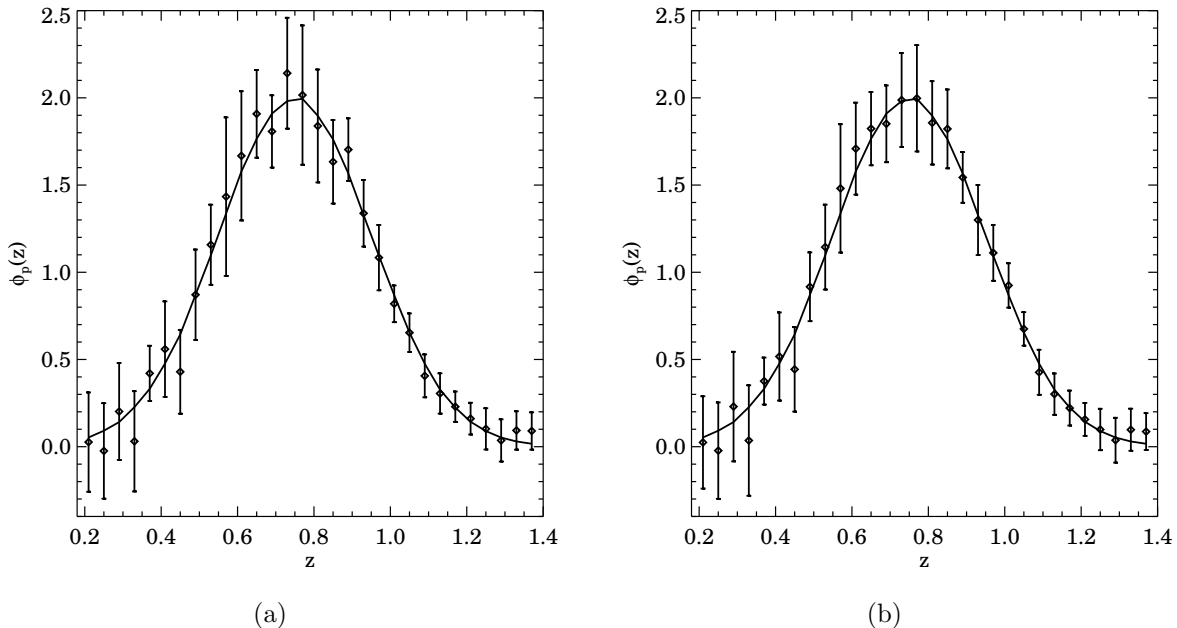
Figure 2.10 Plots of the recovered and mean true redshift distribution of the 24 fields, after the overall redshift distribution of all galaxies in the mock catalogs, dN/dz, is divided out, as described in §2.1.3.2. On the left is the reconstruction before applying a correction for sample/cosmic variance based on fluctuations in the spectroscopic redshift distribution in the fields observed, and on the right is the reconstruction after that correction. There is a significant improvement in the reconstruction. The plot on the right corresponds to the reconstruction of the probability an object falls in the photometric redshift bin as a function of its true z (or, equivalently, the reconstruction of the photometric redshift error distribution), rather than reconstructing the actual redshift distribution (affected by sample/cosmic variance) of galaxies in a particular set of fields, as was depicted in Fig. 2.7. The solid line in each panel is the true normalized distribution of the photometric sample and the points are the median values of 10^4 measurements. Error bars show the standard deviation of the recovered distribution. The standard error in the plotted points is smaller than these error bars by a factor of $\sqrt{6}$ (2.45). As shown here, if we know the amplitude of fluctuations from cosmic variance at a given redshift (using the variance in the distribution of spectroscopic galaxies), as well as the overall distribution of the parent sample (e.g. from combining red-shift distributions from all photometric redshift bins), we can accurately reconstruct the true selection probability distribution.

requirements for future surveys (i.e. $\sigma \sim 2 - 4 \times 10^{-3}$). For cross-correlation techniques to meet these requirements, this excess error will need to be reduced. We discuss a few options for this in §2.1.3.1.

A number of choices we have made on how to model and measure correlation function parameters (e.g. using a fit for the dependence of the spectroscopic sample's autocorrelation parameters on z vs. using the values for a given z-bin directly; assuming $r_{0,pp} \propto r_{0,ss}$ vs. a constant $r_{0,pp}$; or allowing $\gamma_{sp}(z)$ to decrease with redshift vs. forcing a constant γ_{sp}) can affect both the bias and error in these measurements. We have tested reconstruction with alternate methods to those described here and found that the random errors in $\langle z \rangle$ and σ_z are much more robust to these changes than the bias. When varying the three correlation parameters as described previously, the standard deviation of the measurements never varied by more than $\sim 10\%$, but the bias in some cases increased significantly. For measurements of $\langle z \rangle$, the alternative parameter models yielded biases of $0.006 - 0.009$, making them statistically significant compared to the random errors. For σ_z, the biases under the different scenarios were of similar order of magnitude as our standard method, except for the case of using the measured values for the spectroscopic correlation function parameters (r_0 and γ) in each z-bin instead of a fit. This yielded a bias in σ_z of ~ -0.009. From this we see that the methods used to measure correlation parameters need to be considered carefully, since inferior methods can cause the bias to become comparable to random errors.

From equation 13 in Newman (2008), the predicted errors in $\langle z \rangle$ using the weak clustering formalism are essentially identical to the errors in σ_z; that is true to $\sim 20\%$ in our results. This error is a function of σ_z, as well as the surface density of photometric objects on the sky, Σ_p, the number of objects per unit redshift of the spectroscopic sample, dN_s/dz, and the cross correlation parameters, γ_{sp} and $r_{0,sp}$. We use the mean values of these parameters from our catalogs and find that the predicted error on both parameters is $\sigma = 1.064 \times 10^{-3}$. This is considerably smaller than our measured error, which is not surprising given the extra error terms in the correlation function discussed in §2.1.3.1.

Our analysis throughout this paper has considered the case of a single-peaked, Gaussian selection function for placing objects in a photometric bin. However, different distributions would yield similar results, as the error in the recovery of $\phi_p(z)$ at a given redshift depends
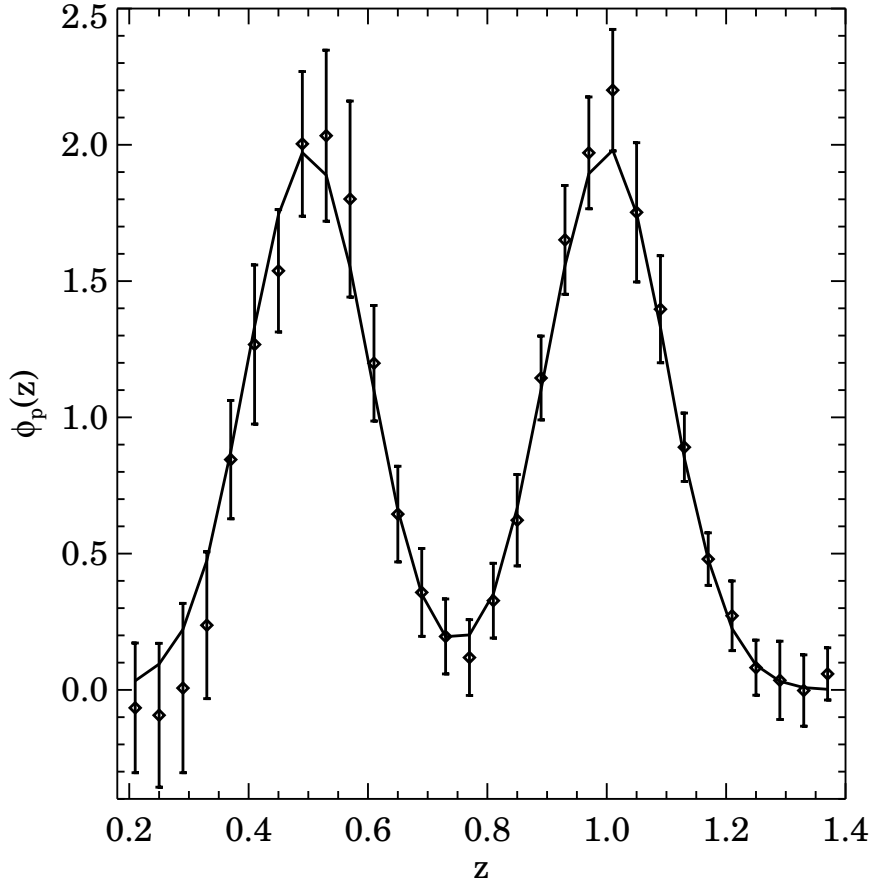
Figure 2.11 Results of cross-correlation reconstruction of a selection function consisting of two equal-amplitude Gaussian peaks centered at $z = 0.5$ and $z = 1.0$, each with $\sigma_z = 0.1$. The solid line is the true distribution of the photometric sample (combining all 24 fields), while the points are the median reconstructed values from 10^4 measurements. Error bars show the standard deviation. The standard error in the plotted points is smaller than these error bars by a factor of $\sqrt{6}$ (2.45). Each measurement is made by averaging the paircounts of four fields selected at random from the 24 mock catalogs. This plot is analogous to the right panel of Fig. 2.10; as in that case, we are reconstructing the selection function of the sample rather than its redshift distribution. The effects of bias evolution should be greater in this case, however, as the sample is less concentrated in redshift. The recovery remains accurate here, despite the larger bias evolution and very different $\phi_p(z)$.

primarily on the characteristics of the spectroscopic sample and the overall size of the photometric sample, but not $\phi_p(z)$ itself (Newman, 2008). We illustrate this in Fig. 2.11, where we have applied the same analysis techniques described above (and laid out in the recipe in §2.1.4) for a selection function that consists of two equal-amplitude Gaussian peaks centered at $z = 0.5$ and $z = 1.0$, each with $\sigma_z = 0.1$; this figure can be compared to the right panel of Fig. 2.10. We note that, since in this scenario the objects selected are less concentrated in redshift, the effects of bias evolution (as predicted by the semi-analytic models used) should be greater here than in our standard case, but our recovery remains accurate.

2.1.4 Summary

In this section we have shown that by exploiting the clustering of galaxies at similar redshifts we can accurately recover the redshift distribution of a photometric sample using its angular cross-correlation with a spectroscopic sample of known redshift distribution, using mock catalogs designed to match the DEEP2 Galaxy Redshift Survey. This test includes the impact of realistic bias evolution and cosmic variance. The error estimates for the recovered mean and standard deviation of the distribution are larger than those predicted previously, but improvements could be obtained either by using more optimal correlation function estimators or by surveying the same number of galaxies distributed over a wider area of sky. In the next section (§2.2) we describe improvements to this technique by incorporating the full covariance information of the correlation function measurements into the power-law fitting procedures.

Section 2.1.2 has described in detail the steps we took to recover the redshift distribution, $\phi_p(z)$, of a photometric sample by cross-correlating with a spectroscopic sample of known redshift distribution. We will now summarize the procedure used to make this calculation, to facilitate its application to actual data sets.

- **Obtain the necessary information for each sample; RA, dec and redshift for the spectroscopic sample, and RA and dec for the photometric sample.**

- **Create the random catalogs for each sample. (§2.1.2.1-2.1.2.3)**

- **Calculate the data-data, data-random, and random-random paircounts for each correlation function.**

  - For $w_p(r_p)$: bin the spectroscopic sample and its corresponding random catalog in redshift. In each spectroscopic z-bin, calculate Δr_p and $\Delta\pi$ for each pair and bin the pair separations into a grid of $\log(r_p)$ and π. Then sum the paircounts in the π direction. (§2.1.2.1)

  - For $w_{pp}(\theta)$: using the "p" sample and its random catalog, calculate $\Delta\theta$ for each pair and bin the pair separations into $\log(\theta)$ bins. (§2.1.2.2)

  - For $w_{sp}(\theta, z)$: bin the spectroscopic sample and its corresponding random catalog in redshift. For each spectroscopic z-bin, calculate the pair separations, $\Delta\theta$, for pairs between the "s" and "p" samples and their random catalogs and bin them into $\log(\theta)$ bins. (§2.1.2.3)

- **Use the paircounts to calculate the correlation functions using standard estimators (e.g. Landy & Szalay). (§2.1.2.1-2.1.2.3)**

- **Calculate the parameters of $w_p(r_p)$ $(r_{0,ss}(z), \gamma_{ss}(z))$ and $w_{pp}(\theta)$ (A_{pp}, γ_{pp}) by fitting as described above. (§2.1.2.1-2.1.2.2)**

- **Use the autocorrelation parameters along with an initial guess of $r_{0,pp}$ (e.g. $r_{0,pp} \sim r_{0,ss}$) to calculate $r_{0,sp}^{\gamma_{sp}}(z) = (r_{0,ss}^{\gamma_{ss}} r_{0,pp}^{\gamma_{pp}})^{1/2}$. (§2.1.2.2)** This gave a more accurate reconstruction of $\phi_p(z)$ (reducing χ^2 by 33%) than the assumption $r_{0,pp} =$ constant; in fact, a calculation of $\xi_{pp}(r)$ from the simulation sample directly showed $r_{0,pp}$ to have similar behavior to $r_{0,ss}$. Using a linear fit of $r_{0,ss}(z)$ and $\gamma_{ss}(z)$ reduced χ^2 by $\sim 32\%$ compared to utilizing the noisier reconstructed values in each z-bin.

- **Estimate $\gamma_{sp} = (\gamma_{ss} + \gamma_{pp})/2$. Using this γ_{sp}, calculate the amplitude, $A_{sp}(z)$, of $w_{sp}(\theta, z)$ by fitting as described above. (§2.1.2.3)** We fit over the range $0.001° < \theta < 0.1°$. We found that fitting over this smaller θ range resulted in smaller errors in the amplitude, $A_{sp}(z)$, which reduced the error in $\phi_p(z)$ for each z-bin by $\sim 25\%$ on average. We fix γ_{sp} because of degeneracies between γ_{sp} and A_{sp} when fitting them simultaneously. This degeneracy is especially strong in regions where $\phi_p(z)$ is small. We also tried modeling γ_{sp} as constant with z using the arithmetic mean of $\gamma_{ss}(z = 0.77)$ and γ_{pp}; however, that method increased the χ^2 of the final fit by $\sim 20\%$.

- Combining the results of the last two steps and the assumed cosmology, calculate $\phi_p(z)$ using equation 2.13. (§2.1.2.3) We also tried calculating $\phi_p(z)$ using the integrated cross-correlation function, $\tilde{w}(z)$, integrating to an angle equivalent to a comoving distance $r_{\max} = 10h^{-1}$ Mpc (Newman, 2008); however, that method produced inferior results.

- Using $\phi_p(z)$, along with the calculated A_{pp} and γ_{pp}, in equation 2.10 gives a new $r_{0,pp}$, which is then used to recalculate $r_{0,sp}^{\gamma_{sp}}(z)$. Putting this back into equation 2.13 gives a new $\phi_p(z)$. This is repeated until convergence is reached. (§2.1.2.3)

- To recover the underlying/universal distribution of objects of the type selected for the photometric sample, rather than the distribution within the specific fields chosen for observation, correct for sample/cosmic variance using the fluctuations in the redshift distribution of the spectroscopic; i.e., construct a smooth function describing the overall redshift distribution of the spectroscopic sample, $\langle dN_s/dz \rangle$, and divide $\phi_p(z)$ by the ratio $dN_s/dz/\langle dN_s/dz \rangle$. (§2.1.3.2)

2.2 INCORPORATING FULL COVARIANCE INFORMATION

Newman (2008) described a new technique for calibrating photometric redshifts (commonly referred to as photo-z's) using cross-correlations which exploits the fact that galaxies at similar redshifts tend to cluster with each other, and in §2.1 we tested this technique using realistic mock catalogs which include the impact of bias evolution and cosmic variance. We showed that for objects in a photometric redshift bin (e.g., selected using some photo-z-based algorithm), we can recover its true redshift distribution, $\phi_p(z)$, by measuring the two-point angular cross-correlation between objects in that bin with a bright spectroscopic sample in the same region of the sky, as a function of spectroscopic z.

In §2.1, we assumed for convenience that correlation function measurements in different angular/radial bins were completely independent. However, analytical models as well as simulations have shown that the covariance between bins is significant (Bernstein, 1994; Zehavi et al., 2005; Crocce et al., 2011). Incorporating all available information about this covariance should provide better constraints on the correlation function parameters used in reconstructing $\phi_p(z)$. In this section we improve on the methods of §2.1 by accounting for this covariance.

However, the inversion of covariance matrices calculated from relatively small sample sizes (e.g. a modest number of mock catalogs or jackknife regions) is not well behaved: modest noise in a covariance matrix can yield large variations in its inverse. We therefore also incorporate ridge regression, a method of conditioning covariance matrices (i.e., stabilizing the calculation of their inverse) which is common in the statistics literature but novel to correlation function analyses, into our methods. We will then optimize the reconstruction of $\phi_p(z)$ by varying the level of this conditioning.

We have implemented an additional step in the reconstruction of $\phi_p(z)$ for this section that was not employed in §2.1. For each measurement, after fixing γ_{sp} and fitting for A_{sp} and C_{sp} in each z-bin, we performed a smooth fit to the measured values of $C_{sp}(z)$ as a function of redshift. Using the same γ_{sp} but fixing C_{sp} at the predicted values for each bin, we then fit for A_{sp}. We obtained the best results from a Gaussian fit to C_{sp}, although simply smoothing the measured $C_{sp}(z)$ values with a boxcar average also resulted in significant

gains in reconstruction accuracy. We initially tested these techniques during our work on the methods presented in §2.1, but they did not improve the reconstruction, and in some z-bins made the reconstruction worse. However, after incorporating covariance information into our analyses, this additional step significantly reduced errors in the reconstruction of $\phi_p(z)$, likely because the determination of C_{sp} for each redshift bin is now more accurate.

We have also made a change in the methods used to calculate average correlation measurements from multiple light cones. In §2.1 this was done by summing the pair counts over all of the fields and using the total pair counts in the Landy & Szalay estimator. However, in the course of this work we found that this method overestimates the mean correlation by more heavily weighting those light cones which are overdense at a particular redshift: they will both contain more pairs and, generally, exhibit stronger clustering than a randomly-selected region of the universe. For this calculation, we instead determine the average correlation by calculating the correlation function in each field individually and then performing an unweighted average of those measurements. This change had little effect on the autocorrelation function of the photometric sample, $w_{pp}(\theta)$, mainly because the larger volume sampled meant that the density varies less from field to field. The projected autocorrelation of the spectroscopic sample, $w_p(r_p)$, and the cross-correlation measurements, $w_{sp}(\theta, z)$, were significantly affected by this change, however, with average decreases in the correlation strength of $\sim 10 - 20\%$.

2.2.1 Fitting Parameters Using Full Covariance Information

In §2.1 we fit for the various correlation function parameters ($r_{0,ss}$, γ_{ss}, etc.) assuming that there is no covariance between measurements in different angular/r_p bins. We determined best-fit parameters by performing a χ^2 minimization where the errors used were given by the standard deviation of the correlation function measurements in each of the 24 mock light-cones; i.e. the fitting assumed that the relevant covariance matrices were all diagonal. However, analytical models as well as simulations have shown that the off-diagonal elements of the covariance matrix are non-negligible (Bernstein, 1994; Zehavi et al., 2005; Crocce et al., 2011). We have confirmed this to be the case by calculating the full covariance matrices of

correlation function measurements in the 24 fields. Therefore, in §2.1 we were not exploiting the full covariance information when fitting for the correlation function parameters. By incorporating this information into our fitting process, we should expect to obtain more accurate results.

In order to calculate the parameters using the full covariance matrix we used χ^2 minimization as in §2.1, but in this case we calculate χ^2 values taking into account the covariance:

$$\chi^2 = (\mathbf{y} - \tilde{\mathbf{y}})^{\mathrm{T}} \mathbf{C}^{-1} (\mathbf{y} - \tilde{\mathbf{y}}) \tag{2.14}$$

where $\mathbf{C}$ is the covariance matrix, $\mathbf{y}$ is the observed correlation function data in each bin, and $\tilde{\mathbf{y}}$ is the expected value according to a given model. As an example, for $w(\theta)$ equation 2.14 becomes:

$$\chi^2 = \left[w(\boldsymbol{\theta}) - (A\boldsymbol{\theta}^{1-\gamma} - C) \right]^{\mathrm{T}} \mathbf{C}^{-1} \left[w(\boldsymbol{\theta}) - (A\boldsymbol{\theta}^{1-\gamma} - C) \right]. \tag{2.15}$$

We start by minimizing equation 2.15 for the case of fixed γ. In that case, this minimization is simply linear regression where $\theta^{1-\gamma}$ is the independent variable, and A and $-C$ are the standard "slope" and "intercept". Minimizing χ^2 analytically to obtain the parameters for a linear fit is straightforward; thus for fixed γ we can readily determine the best-fit A and C via standard formulae. Alternatively, to fit for all three parameters simultaneously we can repeat the linear fit process for different values of γ, and then determine the value of γ which minimizes χ^2. We use this fitting method to determine the parameters of the angular autocorrelation of the photometric sample, $w_{pp}(\theta)$, and of each z-bin of the angular cross-correlation, $w_{sp}(\theta, z)$. For the projected real-space autocorrelation function, we see from equation 2.8 that $w_p(r_p) \sim r_p^{1-\gamma}$ (i.e. the same as the relation between $w(\theta)$ and θ), so the fitting method is the same except that we force the intercept to be equal to zero and only fit for γ and A. We then find r_0 using the conversion $A = r_0^\gamma H(\gamma)$ from equation 2.8. Figure 2.12 compares the fit assuming no covariance for one measurement of $w_{pp}(\theta)$ from the simulation (averaging w_{pp} from 4 of the 24 mock fields) to a fit using the full covariance matrix.

The covariance matrices we use for fitting are calculated using correlation measurements from the 24 mock light-cones, and is therefore a sample covariance matrix and not the "true",
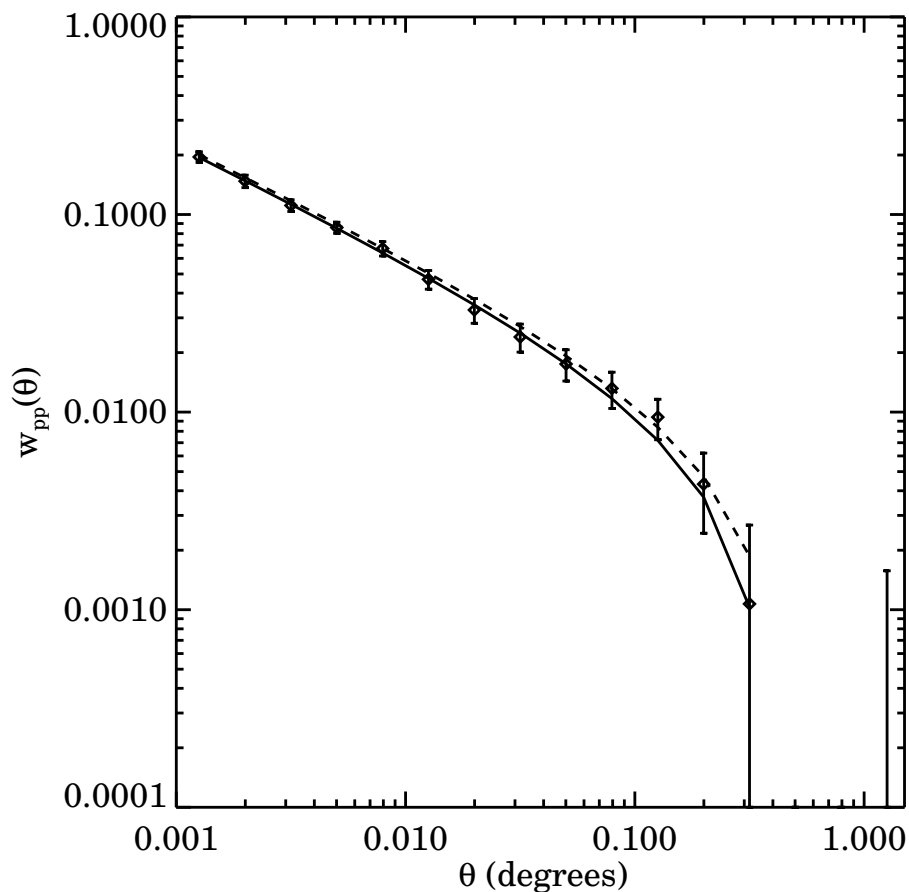
Figure 2.12 An example of fitting a power law-integral constraint model to a measurement of the angular autocorrelation of the photometric sample, $w_{pp}(\theta)$, from Millennium catalog mock light cones. The solid line is a fit assuming no covariance between angular bins, while the dashed line is a fit using the full covariance matrix, where both are fit over the range $0.001° < \theta < 1.584°$.

underlying $\mathbf{C}$. It can be shown that while the sample covariance matrix is an unbiased estimator of $\mathbf{C}$, the inverse of the sample covariance matrix is in fact a **biased** estimator for the inverse of the true covariance matrix (Hartlap et al., 2007). The amount of bias depends on the size of the sample used to calculate the covariance matrix; in our case, this is the number of mock catalogs (24). However, this bias can be corrected for (assuming Gaussian statistics and statistically independent measurements) simply by rescaling the inverse sample covariance matrix by a constant factor; this will not, therefore, affect the location of any χ^2 minimum. We apply a bias correction where relevant in our analysis below.

2.2.2 Conditioning the Covariance Matrix

Since we are using a covariance matrix calculated from a modest number of light cones–in effect a "measured" covariance matrix with only a limited number of samples–noise and numerical instabilities cause difficulties when calculating $\mathbf{C}^{-1}$. We found the inversion of $\mathbf{C}$ to be much more well behaved when using coarser bins in θ and r_p than employed in §2.1. For both $w_p(r_p)$ and $w(\theta)$ we doubled the bin size in log space, i.e. we use bins with $\Delta \log(r_p) = 0.2$ and $\Delta \log(\theta) = 0.2$. Increasing the bin size further did not yield significant improvements.

To reduce the impact of noise in our measured covariance matrix further, we investigated several methods of conditioning the matrix (i.e., modifying the covariance matrix to improve the robustness of its inversion), and looked at how varying the conditioning improved the reconstruction. One commonly-applied method involves performing a singular value decomposition (SVD) of the covariance matrix and setting the singular values below some threshold (and their inverse) equal to zero (Jackson, 1972; Wiggins, 1972). This is equivalent to performing an eigenmode analysis and trimming any unresolved modes, as is done, for instance, in McBride et al. (2011).

We also tried conditioning the covariance matrix using a technique commonly known as ridge regression (Hoerl & Kennard, 1970). This involves adding a small value to all of the diagonal elements of the covariance matrix before inverting, which reduces the impact of noise in the off-diagonal elements and makes the inversion more stable. We parameterized

this conditioning by calculating the median of the diagonal elements of the covariance matrix and adding a fraction f of that median value to the diagonal. We obtained better results from ridge regression than from zeroing out singular values (see §2.2.3.1 below), and it is therefore the primary method used throughout the rest of this section.

At first glance it may seem that applying ridge regression to the covariance matrix should be detrimental to determining the actual values of correlation function parameters: we are effectively assuming by fiat that the effective covariance matrix to be used in calculating χ^2 differs from what was measured. Since ridge regression yields larger values for the diagonal elements of the covariance matrix than the data themselves would suggest, the results are equivalent to a situation with larger nominal measurement uncertainties (and hence broader χ^2 minima) than implied by the original covariance matrix.

However, when $\mathbf{C}$ is determined from a limited set of measurements, $\mathbf{C}^{-1}$ tends to differ significantly from the true inverse. Hence, using the standard covariance matrix in fitting should lead to measurements with nominally tighter errors than ridge regression techniques, but those measurements may in fact be significantly offset from the true value of the parameter we are attempting to determine. This can cause the parameter results to have larger spread about the true value than optimal. When we add some degree of ridge regression, the inverse of the covariance matrix is better behaved, and hence is less likely to yield a discrepant result. By varying the strength of the ridge regression conditioning, we can choose different tradeoffs between the bias and variance of parameter estimates. In general, we want both of these contributions to be small; in the next section we investigate what degree of conditioning minimizes their sum.

2.2.3   Risk Optimization

In this section we will evaluate how the conditioning of the covariance matrix affects the determination of correlation function parameters and ultimately the reconstruction of $\phi_p(z)$. By doing so, we will be able to optimize the reconstruction of the true redshift distribution of the photometric sample. We assess this by measuring the integrated mean squared error, i.e. the variance plus the bias squared. This is commonly referred to in statistics literature

43

as the "risk". By focusing on the risk in some quantity we are optimizing for the minimum combined effect of variance and bias: either large random errors or large bias would lead to a large risk. We hence define the risk to be $\mathcal{R}(X) = \langle (X - X_{\text{true}})^2 \rangle$, where $X - X_{\text{true}}$ is the difference between the measured parameter value and its true value . At times we will also refer to the fractional risk of a parameter, which we define as $\tilde{\mathcal{R}}(X) = \langle (X - X_{\text{true}})^2 \rangle / X_{\text{true}}^2$. Since we utilize three different types of correlation measurements in the reconstruction of $\phi_p(z)$, we look at how changing the level of conditioning of the covariance matrix affects each one individually.

2.2.3.1 Optimizing Fits To $w_{pp}(\theta)$ We optimized the conditioning of the covariance matrix for the autocorrelation of the photometric sample using a Monte Carlo simulation where we use the covariance matrix of w_{pp} calculated from the 24 fields (i.e., the 24 different light cones) as our "true" covariance matrix, and then use it to generate realizations of correlated noise about a selected model. To do this we first find the eigenvalues and eigenvectors of the covariance matrix. We create uncorrelated Gaussian noise with variances equal to the eigenvalues, and then apply the transformation matrix constructed from the eigenvectors to this noise. This technique yields mock data with correlated noise corresponding exactly to the "true" covariance matrix (here, the covariance matrix of the 24 mock fields). For the true model we use $A_{\text{true}} = 4.0 \times 10^{-4}$, $\gamma_{\text{true}} = 1.58$, and $C_{\text{true}} = 6.5 \times 10^{-3}$, which are approximately the mean parameters measured from the simulation.

In §2.1 we used the 24 mock light-cones to generate 10^4 "measurements" by randomly selecting four fields at a time and finding the average $w(\theta)$ for those fields. In order to simulate this we used the method for generating correlated noise described above to create 24 realizations of single-field $w(\theta)$ measurements, and then generated 10^4 randomly selected "pick-4 measurements" from those 24 realizations; we will refer to each set of 24 new realizations (and its derived products) as a "run" below. For each run we use the set of 24 realizations to calculate a measured covariance matrix, which will differ from the true covariance matrix used to generate the noise. The uncertainty in an estimate of the covariance matrix from the 24 realizations should be worse than the errors in realistic applications, making this treatment conservative. This is because the area covered by photometric sur-

44

veys will in general be much larger than for the spectroscopic sample, which will result in a better constrained covariance matrix for the autocorrelation of the photometric sample; however, for the mock catalogs used here the spectroscopic and photometric areas are identical. The resulting "measured" covariance matrix for a given run is then used to fit for the parameters of a power-law fit in each of that run's pick-4 measurements by minimizing χ^2 (cf. equation 2.14). For this and all other correlation function fits described herein we used the IDL code POWERFIT, which I have developed and has been publicly released at http://www.phyast.pitt.edu/~janewman/powerfit. A more detailed description of the code is given in Appendix B.

We begin by evaluating how the reconstruction of the amplitude, A, changes as we vary the conditioning. The integral constraint exhibits similar behavior to the amplitude since it is proportional to the correlation strength; we are in any event not as concerned with the behavior of C since it is essentially a nuisance parameter. For simplicity, we fix γ at the true value for each run and only fit for A and C. We calculate the risk on A by performing 10^4 runs, where for each run we:

1. Created 24 realizations of $w(\theta)$ as described above

2. Generated 10^4 pick-4 measurements, randomly selecting four realizations at a time from the 24 and calculating their mean $w(\theta)$

3. Fit each pick-4 measurement for A and C using the covariance matrix calculated from the 24 realizations created in step 1

4. Calculated the mean fractional risk on A over the 10^4 pick-4 measurements, $\tilde{\mathcal{R}}(A) = \langle (A - A_{\text{true}})^2 \rangle / A_{\text{true}}^2$.

We can perform the fits and calculate the fractional risk on A while applying varying levels of conditioning on the covariance matrix. We parameterize the ridge regression conditioning using a variable f, which we define as the fraction of the median value amongst diagonal elements of the covariance matrix which is added to the diagonal elements; i.e., we replace the i,i element of the covariance matrix, $\mathbf{C}_{ii}$, by $\mathbf{C}_{ii} + f \times \text{median}(\mathbf{C}_{ii})$. For comparison, we also calculate the fractional risk on A while varying the singular value threshold for the SVD conditioning described in §2.2.2, where all singular values below the threshold and their

inverses are set to zero.

Figure 2.13 shows the square root of the median and maximum fractional risk amongst the 10^4 runs as a function of both f and the singular value threshold. In both cases we see that the conditioning has a much stronger effect on the maximum risk than it does on the median. We therefore perform a minimax optimization; i.e., we choose the conditioning that minimizes the maximum risk. Looking at the level of conditioning corresponding to this minimax optimization for each method, we see that the median and maximum risk are both smaller for the ridge regression conditioning. In addition, with the SVD method the maximum risk is much more sensitive to changes in the threshold around its optimized value. Small changes from the optimized threshold value in either direction can have a significant effect on the maximum risk, while the maximum risk curve for the ridge regression method is relatively flat in the vicinity of the optimized value. We therefore use ridge regression conditioning for the remainder of the calculations. By adding a few percent conditioning to our covariance matrix with the ridge regression method, we can significantly decrease the maximum risk without significantly worsening the median risk. The optimized value for f strikes a balance between the need for conditioning to stabilize inversion and the desire not to distort the relative impact of diagonal and off-diagonal covariance matrix elements, which would lead to inappropriate weighting of different data points in calculating χ^2.

Figure 2.14 shows a contour plot of the median values of $A - A_{\text{true}}$ vs. $C - C_{\text{true}}$ amongst all pick-4 measurements for each of the 10^4 runs using the optimized conditioning ($f = 3\%$). In §2.1, although we had measured the correlation function out to a separation $\theta \sim 1.584°$, we only fit over the range $0.001° < \theta < 0.1°$. In that case, fitting over this smaller range reduced the error in A, and thus improved the reconstruction. When using the full covariance matrix for the fit we found that fitting over the full range of θ yielded even smaller parameter errors, as seen in Figure 2.14. By utilizing covariance information in our fitting, we can robustly incorporate correlation measurements from larger scales which were useless (or even detrimental) when ignoring the covariance.

2.2.3.2 Optimizing Fits To $w_p(r_p)$ We used a different method to optimize the conditioning for the projected correlation function of the spectroscopic sample. As described
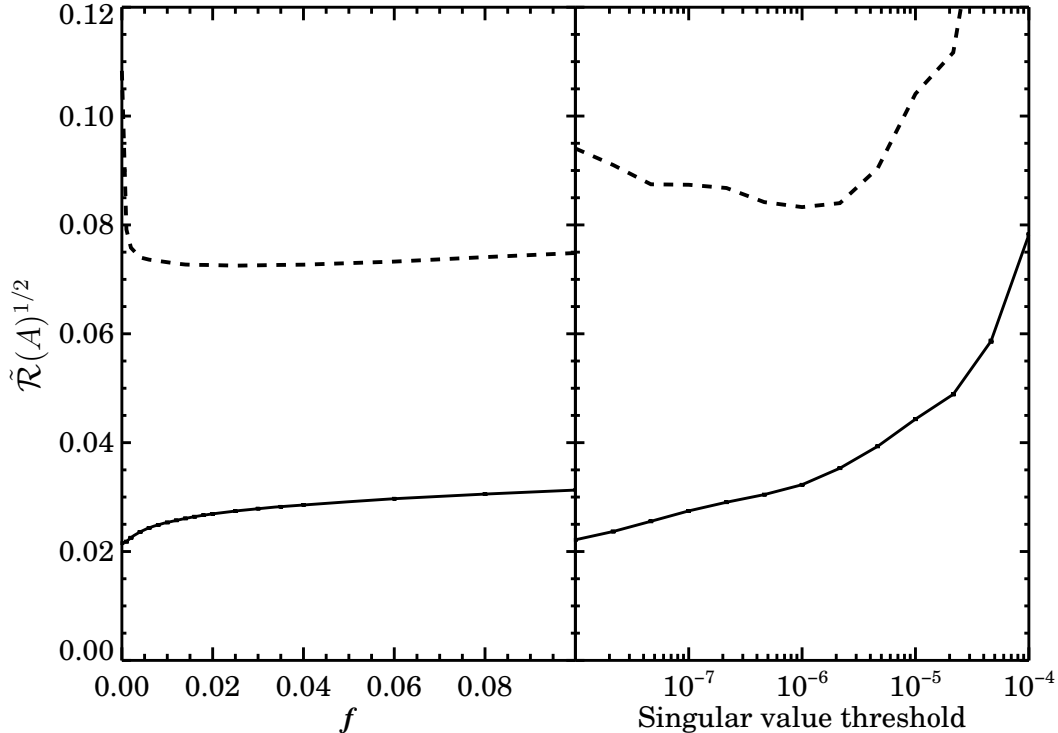
Figure 2.13 A test of the impact of the conditioning of the covariance matrix on the results from fitting the amplitude of the correlation function, A. We plot the square root of the fractional median risk (solid line) and of the maximum risk (dashed line) on A as a function of the degree of conditioning. We define the risk as the total mean squared error; i.e., the variance plus bias squared. (Left panel) We condition using ridge regression; we add a fraction f of the median of the diagonal covariance matrix elements to all diagonal elements in order to stabilize the inversion of the covariance matrix. (Right panel) We condition by inverting using singular value decomposition (SVD), setting all singular values below some threshold to zero. The median values are from a single set of 10^4 runs, but the maximum risk line is the mean of the results from 10 sets of 10^4 runs, as the maximum risk varied significantly from run to run. Errors on the median are plotted, but are very small and not visible. The conditioning has a much larger effect on the maximum risk, and we therefore use a minimax optimization: i.e., choose the parameter values which make the maximum risk as small as possible. Using ridge regression, both the median and maximum optimized risk are smaller than for the SVD method. We therefore use ridge regression as our primary conditioning technique; the optimum results in fitting $w_{pp}(\theta)$ are achieved for $f \sim 3\%$.
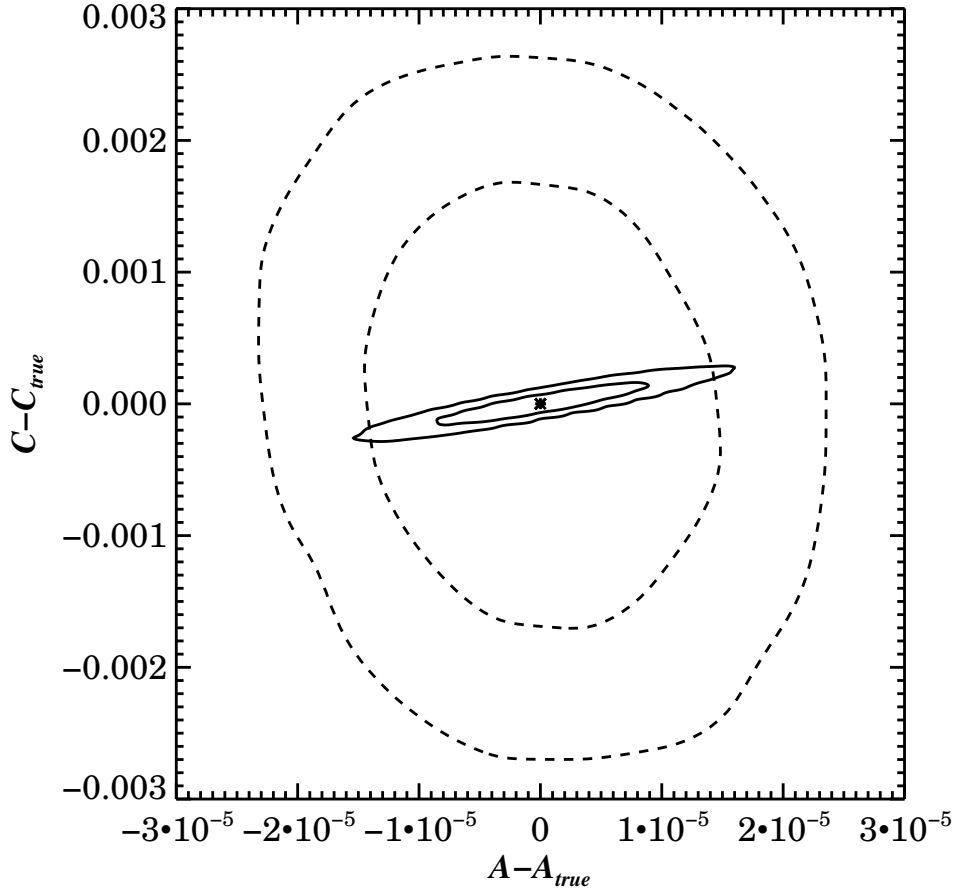
Figure 2.14 Contour plot showing the distribution of the median values of $A - A_{\text{true}}$ and $C - C_{\text{true}}$ from each of 10^4 runs as described in §2.2.3.1, where A and C are the fit parameters for $w(\theta) = A\theta^{1-\gamma} - C$. For our model we used $A_{\text{true}} = 4.0 \times 10^{-4}$ and $C_{\text{true}} = 6.5 \times 10^{-3}$. For each distribution we show the 1σ and 2σ contours. The solid lines are the fit parameters when using the full covariance matrix with the optimized conditioning ($f = 3\%$). The dashed lines show the distribution resulting from fits with the same techniques as §2.1, where we assume no covariance and fit over a smaller θ range. We are most concerned with errors in the amplitude; it is clear there is a significant improvement in the recovery of the actual value of A when the full covariance information is exploited.

in §2.1.1, this sample was constructed by selecting 60% of the objects with $R < 24.1$. We calculated the risk for the autocorrelation parameters by creating multiple samples where a different 60% of the objects are chosen each time, and comparing these to the results for a sample containing 100% of the objects. This differs from the method used in §2.2.3.1 in that we are actually performing the correlation measurements using the simulations rather than generating model noise based on a covariance matrix calculated from the simulation. In the case of $w_{pp}(\theta)$ it was more difficult to determine the true values of $w(\theta)$ (required for calculating the risk) to significantly greater accuracy than individual measurements, and therefore we relied on synthetic techniques for that analysis. Here, we have a "truth" measurement which is much better than the fits resulting from any set of 60% of the bright objects in only four fields, so we can measure the risk robustly without relying on simulated measurements. When calculating the reconstruction of $\phi_p(z)$ we measure the parameters of a fit to $w_p(r_p)$ in multiple redshift bins. For simplicity, in this section we focus on a single z-bin in the middle of the redshift range, $0.613 < z < 0.704$; we expect similar results for the other redshift bins.

To begin we generate 10^4 pick-4 measurements of $w_p(r_p)$ from the full sample and fit each measurement to the functional form given in equation 2.8, employing the full covariance matrix calculated from the 24 fields to determine r_0 and γ. As in §2.1, we fit over the range $0.1 < r_p < 10\ h^{-1}\mathrm{Mpc}$. Since the covariance matrix calculated from the full sample should be more stable than for the 60% subsets due to its smaller noise, we initially performed the fits with zero conditioning and used that as our "truth". The median values of the parameter measurements for the full sample amongst the 24 different fields were used as estimates of the true parameter values. We then calculate the risk on r_0 and γ by performing 100 runs, where for each run we:

1. Constructed samples from each of the 24 mock fields by randomly selecting 60% of the objects with $R < 24.1$

2. Generated 10^4 pick-4 measurements, randomly selecting four fields at a time from the 24 and calculating their mean $w_p(r_p)$

3. Fit each pick-4 measurement for r_0 and γ using the covariance matrix calculated from

the $w_p(r_p)$ values measured using the 24 samples constructed in step 1[1]

4. Calculated the mean fractional risk on both parameters, $\tilde{\mathcal{R}}(r_0) = \langle (r_0 - r_{0,\text{true}})^2 \rangle / r_{0,\text{true}}^2$ and $\tilde{\mathcal{R}}(\gamma) = \langle (\gamma - \gamma_{\text{true}})^2 \rangle / \gamma_{\text{true}}^2$, over the 10^4 pick-4 measurements.

In step 3 we calculate the covariance matrix from 24 fields, which is more fields than we would actually have if we were to do cross-correlation reconstruction with current datasets at $z \sim 1$. However, it is likely comparable to the level to which we should be able to determine the covariance matrix using current-generation deep mock catalogs, particularly since fit results will be sensitive to the relative values of covariance matrix elements, but not their absolute normalization. For each run we calculate the fractional risk on both parameters for varying levels of conditioning. Figure 2.15 shows the square root of the median and maximum fractional risk on r_0 and γ amongst the 100 runs as a function of the conditioning. For both parameters we see a slight dip in the median risk over the 100 runs at $f \sim 0.5\%$, but this represents only a minimal improvement. Once again we see the conditioning has a much more significant impact on the maximum risk. We optimize our fits by choosing the conditioning value that minimizes the maximum risk ($f \sim 3.5\%$).

2.2.3.3   Optimizing $\phi_p(z)$ Reconstruction   After optimizing the fits for the autocorrelation measurements, we then looked at how conditioning the cross-correlation covariance matrices affects the overall reconstruction of $\phi_p(z)$. Since the uncertainty in $\phi_p(z)$ is dominated by the uncertainty in $w_{sp}(\theta, z)$, this conditioning should have the greatest impact on the reconstruction. We generate 10^4 pick-4 measurements by averaging the correlation measurements from four randomly selected fields out of the 24, which we then use to calculate $\phi_p(z)$. For calculating the risk, we know the true redshift distribution in each field perfectly from the simulation, so we do not need to rely on synthetic techniques as in §2.2.3.1. Since the fits for both $w_{pp}(\theta)$ and $w_p(r_p)$ were best with a few percent ridge regression conditioning (§2.2.3.1, §2.2.3.2), for simplicity we adopt f=3.5% as the optimal conditioning in both cases.

---

[1] In §2.1, we corrected $w_p(r_p)$ for the fact that $\xi_{ss}(r_p, \pi)$ is not in actuality measured to infinite line-of-sight separation. This was not done for this test, as the correction will affect the parameters of the full sample and its subsets in a similar way, so any trends in the risk should not be affected. This saved significant calculation time.
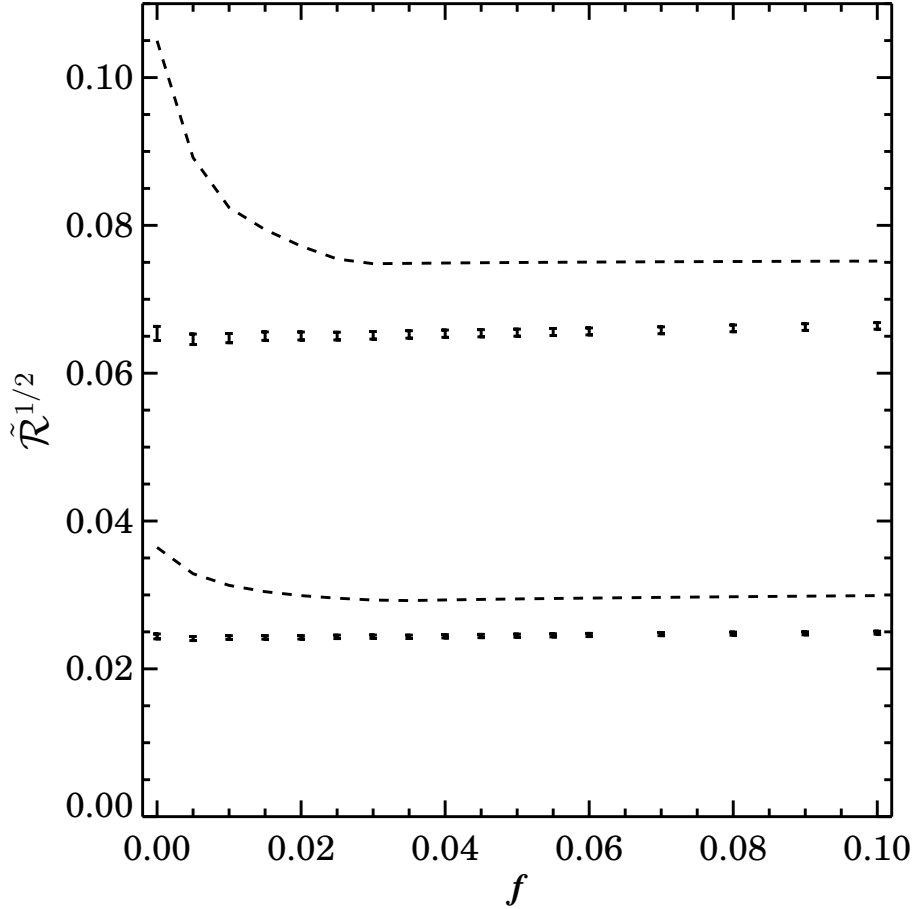
Figure 2.15 The square root of the fractional median risk (error bars) and maximum risk (dashed line) on $r_{0,ss}$ (upper curves) and γ_{ss} (lower curves) as a function of the degree of conditioning used for 100 runs, where 60% of objects with $R < 24.1$ were selected at random for each run, as described in §2.2.3.2. The conditioning has a much larger effect on the maximum risk for both parameters, and we therefore use a minimax optimization, i.e. $f=3.5\%$.

For each pick-4 measurement, we determine the autocorrelation parameters of the photometric sample by fitting the $w_{pp}(\theta)$ from the selected 4 fields using the optimally conditioned covariance matrix calculated from the 24 fields. All three parameters (A_{pp}, γ_{pp}, and C_{pp}) are left free and fit simultaneously. To measure the evolution of the correlation function parameters of the spectroscopic sample, we calculated $w_p(r_p)$ in 10 z-bins covering the range $0.11 < z < 1.4$, where the size and location of each z-bin was selected such that there were approximately the same number of objects in each one. In each z-bin we calculate the covariance matrix from the 24 fields and fit each pick-4 measurement using the optimal conditioning to determine $r_{0,ss}(z)$ and $\gamma_{ss}(z)$.

In one redshift bin ($0.11 < z < 0.268$), the values of $r_{0,ss}$ and γ_{ss} obtained with these methods were significantly different from the values determined when assuming no covariance. We investigated the likelihood contours in detail and found they were not well behaved; not only were the median parameter values different from the result with no covariance, the standard deviation of the 10^4 pick-4 measurements proved to be an underestimate of the uncertainty in that bin, which had significant effects when performing an error-weighted linear fit to $r_{0,ss}(z)$ and $\gamma_{ss}(z)$. We attempted a variety of methods for estimating the errors in that bin with poor results. However, we found that fitting over the shorter range $0.25 < r_p < 10~h^{-1}\mathrm{Mpc}$, rather than $0.1 < r_p < 10~h^{-1}\mathrm{Mpc}$, gave more well behaved values (more consistent with the values in other redshift bins or those obtained when ignoring covariance) and improved the reconstruction. For consistency we fit over this range for all bins where $z < 0.8$. As in §2.1 we continue to fit over the range $1.0 < r_p < 10~h^{-1}\mathrm{Mpc}$ for $z > 0.8$, as in the Millennium simulations (though less so in real datasets) $w_p(r_p)$ diverges significantly from a power law at $0.1 < r_p < 1~h^{-1}\mathrm{Mpc}$.

While the conditioning of the fits for the autocorrelation parameters was kept the same for each measurement, we varied the conditioning of the cross-correlation fits to see how it affects the reconstruction. We bin the spectroscopic sample over the range $0.19 < z < 1.39$ with a bin size of $\Delta z = 0.04$ and measure $w_{sp}(\theta)$ in each bin. At each level of conditioning we:

1. Calculated the covariance matrix of $w_{sp}(\theta)$ in each redshift bin from the 24 fields and apply the ridge regression conditioning to each matrix

2. Generated 10^4 pick-4 measurements, randomly selecting four fields at a time from the 24 and calculating their mean $w_{sp}(\theta, z)$

3. In each z-bin, fit the pick-4 measurements for A_{sp} and C_{sp}, fixing γ_{sp} as described in §2.2.1, using the covariance matrices calculated in step 1

4. Combined $A_{sp}(z)$ and the optimized autocorrelation parameters for each pick-4 measurement to calculate the probability distribution function, $\phi_p(z)$, applying equation 2.3

5. For each pick-4 measurement, we calculated the mean risk on $\phi_p(z)$, $\mathcal{R}(\phi_p(z)) = \langle (\phi_p(z) - \phi_{p,\text{true}}(z))^2 \rangle$, over the range $0.4 < z < 1.2$. This was done in two ways:

   a. Using the overall mean $\phi_p(z)$ of the 24 fields as $\phi_{p,\text{true}}(z)$

   b. Using the mean $\phi_p(z)$ from the particular 4 fields used in a given measurement as $\phi_{p,\text{true}}(z)$

6. Calculated the mean $\mathcal{R}(\phi_p(z))$ over the 10^4 pick-4 measurements for both types of risk

In step 5, we calculate the risk over a slightly limited redshift range to eliminate bins where noise dominates the measurements, which diluted our ability to assess the impact of ridge regression.

Figure 2.16 shows both mean risks as a function of the conditioning, compared to the risk using methods identical to §2.1. We optimized for the mean risk over the redshift range rather than the maximum risk as the latter was dominated by random outliers (due to the smaller number of objects in the redshift bins used, errors in $w_{sp}(\theta, z)$ are much larger, and hence random excursions extend further, than for the autocorrelations). Both techniques indicate that the minimum risk is obtained at around a few percent conditioning. There is a substantial improvement in both measures, but particularly in the risk comparing the redshift distribution for the four chosen fields to the overall (e.g. universal) mean. Figure 2.17 shows the reconstruction for 3.5% conditioning (i.e. the same for all three fits) as well as the variance and bias, and compares to the reconstruction using methods identical to §2.1. The decrease in the variance is significant in each redshift bin while the bias is relatively unchanged in all but a few z-bins. By incorporating full covariance information and ridge regression methods, the square root of the fractional risk is $< 40\%$ smaller than that resulting from our prior methods.
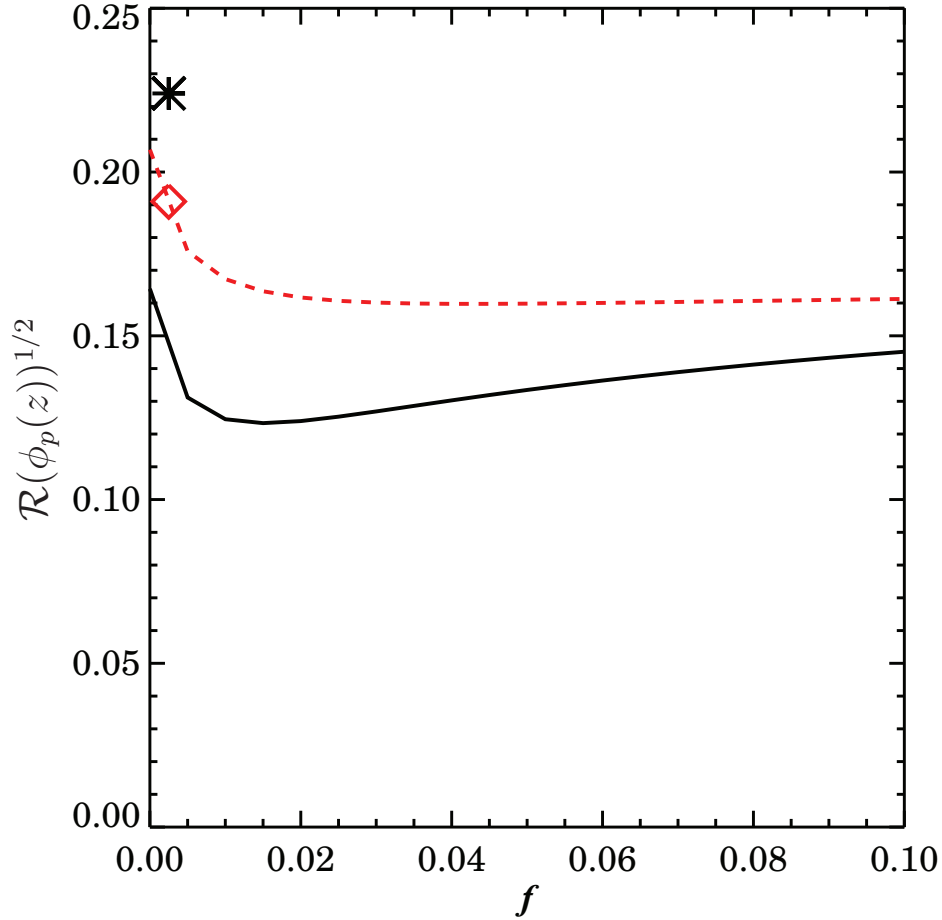
Figure 2.16 The square root of the mean risk over the range $0.4 < z < 1.2$ for the reconstruction as a function of the degree of conditioning applied to the covariance matrix of $w_{sp}(\theta)$ in each redshift bin. The solid line is the risk compared to the overall mean of the 24 fields, and the star symbol is the corresponding risk using the methods of §2.1. The dashed red(gray) line is the risk defined from comparing each measurement to the mean redshift distribution of the particular 4 fields used, and the red(gray) diamond symbol is the corresponding risk using the previous method. Both are at or near their minimum value at a conditioning of a few percent. The decrease in the risk when comparing to the overall mean is much greater, though improvements are significant regardless of the measure used.
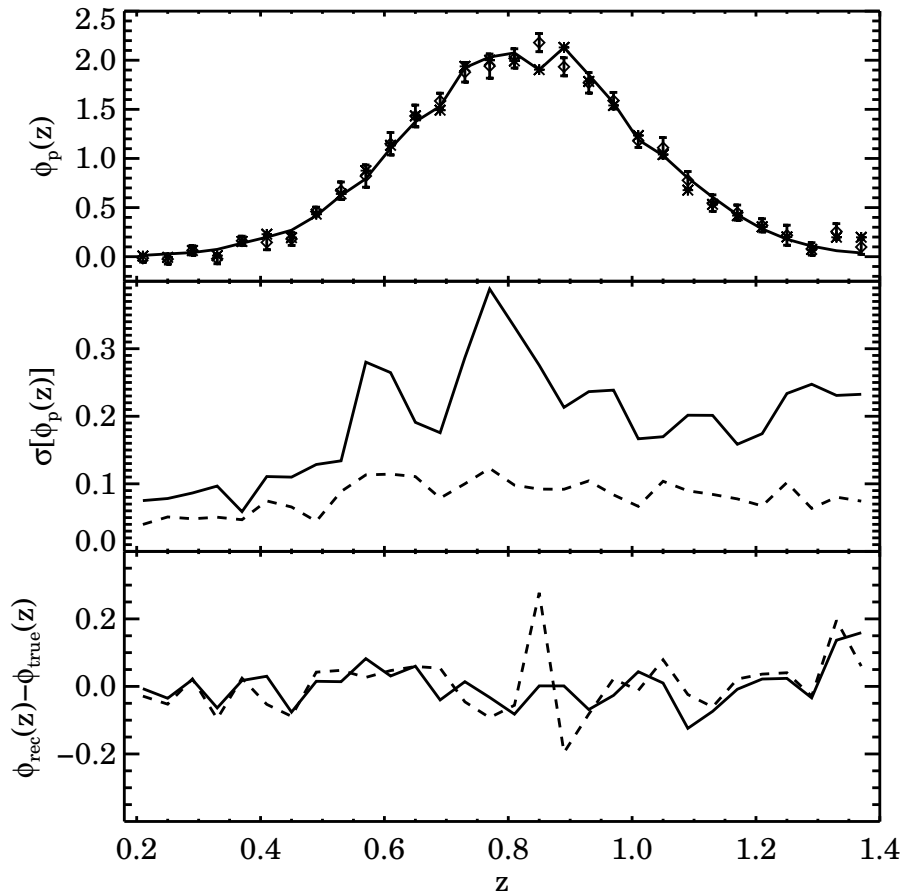
Figure 2.17 The reconstruction of $\phi_p(z)$ using 3.5% conditioning for fits to all three correlation measurements, (i.e. $w_{pp}(\theta)$, $w_p(r_p)$, $w_{sp}(\theta, z)$). In the top panel, the solid line is the mean true distribution of the 24 fields, the star symbols are the median values of the 10^4 pick-4 measurements obtained using the methods of §2.1, and the diamonds are the median values for the optimized reconstruction using the full covariance matrix for the fits (with error bars). The middle panel compares the standard deviation of the 10^4 pick-4 measurements in each bin using the methods from §2.1 (solid line) to the improved reconstruction (dashed line), while the bottom panel compares the bias. The errors are significantly smaller in each bin, while the bias is comparable when full covariance information is used. These results are not significantly changed for moderate changes in f.

2.2.4 Summary

In this section we have improved on the cross-correlation techniques presented in §2.1 by incorporating full covariance information. In addition, we have demonstrated the improvements that result from incorporating ridge regression in fitting for correlation function parameters. Conditioning using ridge regression allowed us to obtain a more stable inversion of the covariance matrix by reducing the impact of noise in the off diagonal elements, resulting in better estimates of the correlation function parameter values; results were significantly better than with other commonly-used methods such as zeroing out small singular values in a singular value decomposition of the covariance matrix. We analyzed how this conditioning affected the integrated mean squared error, i.e. the risk, for these parameter measurements, and in doing so optimized the cross-correlation technique for recovering the redshift distribution of a photometric sample with unknown redshifts. We also found that we gain significant improvement in the reconstruction by adding a step to the recipe described in §2.1.4: we now perform a smooth fit for the amplitude of the integral constraint of the cross-correlation measurements as a function of redshift, $C_{sp}(z)$. We then refit for the amplitude of the cross-correlation, A_{sp}, with C_{sp} fixed at the smooth fit value in each z-bin.

We tested the effect of the ridge regression technique on the calculation of parameter values for both $w(\theta)$ and $w_p(r_p)$ and found that it had a much more significant impact on the maximum risk found over multiple runs than on the median risk. In other words, it yields a great improvement in the worst-case errors, but smaller improvements in more typical cases. For $w(\theta)$ the square root of the maximum fractional risk in the amplitude, A, for fixed γ decreased by $\sim 35\%$ on average at a few percent conditioning. For $w_p(r_p)$ we found a similar decrease for $r_{0,ss}$ ($\sim 29\%$), while the decrease for γ_{ss} was somewhat smaller ($\sim 20\%$)–although still significant. After implementing the changes described above to the recipe described in §2.1.4 we found that adding just a few percent of the ridge regression conditioning to each covariance matrix used in the calculation resulted in a significant improvement in the cross-correlation reconstruction. When conditioning all covariance matrices at the level of 3.5% there was $\sim 42\%$ decrease in the mean of the square root of the risk on the recovered $\phi_p(z)$ compared to the overall (i.e. universal) mean $\phi_p(z)$, and $\sim 16\%$ decrease when comparing

the recovered $\phi_p(z)$ to the mean of the actual $\phi_p(z)$ for the particular four fields used in the measurement.

2.3 INDUCED CORRELATION FROM WEAK LENSING

When measuring the cross-correlation between two galaxy samples in real data sets, there is a contribution to the signal from weak gravitational lensing by the large scale structure along the line of sight, even if the two samples are widely separated in redshift. If one sample is at a higher redshift, the objects at higher redshift can be lensed by the objects in the lower redshift sample, which causes a magnification bias that induces a correlation signal (Broadhurst et al., 1995; Bartelmann & Schneider, 2001). This effect is not included in the simulation used in the previous tests described in this chapter, but it will need to be accounted for in real galaxy samples.

Magnification bias occurs when gravitational lensing changes the observed number density of galaxies, and its contribution is determined by two competing effects. First, scattering of light rays by the intervening large scale structure increases the observed area on the sky. In addition, galaxies that would have been too faint to be included in a magnitude limited sample are magnified by gravitational lensing and are therefore included. The combination of these two effects can change the number density of galaxies in a given patch of sky which can induce a correlation. The effect of magnification bias on the angular correlation function is well known (Moessner & Jain, 1998; Ménard & Bartelmann, 2002; Jain et al., 2003; Scranton et al., 2005; Loverde et al., 2008).

2.3.1 Calculating the weak lensing signals

To calculate the induced correlation from lensing we follow the derivation in Moessner & Jain (1998), but write the final result in terms of the galaxy correlation function instead of the dark matter power spectrum. This simplifies the calculation by avoiding the calculation of the power spectrum, and we can readily get the parameters for the power-law form of

the correlation function from the simulation. In general, for two distributions of galaxies the lensing correlation signal due to sample 2 (described by a probability distribution $\phi_2(z)$) being lensed by sample 1 (described by a probability distribution $\phi_1(z)$) may be written as

$$w_{[1,l]2}(\theta, z) = 3\Omega_m \left(\frac{H_o}{c}\right)^2 \frac{2.5s_2 - 1}{b_2} \int_0^\infty \phi_1(z) \frac{g_2(z)}{a} dz \int_{-\infty}^{+\infty} \xi_{12}\left(\sqrt{\pi^2 + D(z)^2\theta^2}\right) d\pi,$$

(2.16)

where a is the scale factor, $\xi_{12}(r)$ is the real-space cross-correlation of the two samples, b_2 is the linear bias factor of sample 2 and s_2 is the slope of the number counts of galaxies with limiting magnitude m, where

$$s_2 = \frac{d\log N_2(m)}{dm}.$$

(2.17)

The notation $[1, l]$ simply denotes that sample 1 is acting as the lens. The lensing kernel of sample 2, $g_2(z)$, is defined by

$$g_2(z) = D(z) \int_z^\infty \frac{D(z') - D(z)}{D(z')} \phi_2(z') dz'.$$

(2.18)

The lensing kernel is a radial weight function that describes the strength of the lensing effect on objects in $\phi_2(z)$ by perturbations at redshift z. It is a maximum at around midway between between the observer and the typical redshift of $\phi_2(z)$ (e.g. $\langle z \rangle$ if $\phi_2(z)$ is Gaussian). If we assume a power-law for the cross-correlation signal, $\xi_{12} = (r/r_{0,12})^{-\gamma_{12}}$, it can be shown that

$$w_{[1,l]2}(\theta, z) = 3\Omega_m \left(\frac{H_o}{c}\right)^2 \frac{2.5s_2 - 1}{b_2} H(\gamma_{12})\theta^{1-\gamma_{12}} \int_0^\infty r_{0,12}^{\gamma_{12}} \phi_1(z) \frac{g_2(z)}{a} D(z)^{1-\gamma_{12}} dz. \quad (2.19)$$

2.3.2 Induced correlation when applying the cross-correlation technique

In the case of the cross-correlation technique there are two significant contributions to the lensing signal. The first, $w_{[s,l]p}(\theta)$, is the signal induced by the photometric sample being lensed by objects in the narrow spec-z bin used in calculating $w_{sp}(\theta)$, where again the $[s, l]$ indicates the spectroscopic objects are acting as the lens. This signal is strongest when the spec-z bin is at lower redshift than the majority of the photometric objects (i.e. less than the mean of the photometric distribution). The second, $w_{s[p,l]}(\theta)$, is the signal induced by objects in the spec-z sample being lensed by the photometric sample. This signal is strongest when

the spec-z bin is at higher redshift than the photometric sample. There is also a signal due to the spectroscopic and photometric objects being lensed by dark matter in the foreground of both samples, but this is negligible compared to the other two terms.

Next we calculate the induced correlation from weak lensing for the same configuration used to test the cross-correlation technique in §2.1 and §2.2, where we determined the cross-correlation of a narrow spectroscopic redshift bin with a Gaussian photometric sample. We approximate the distribution of each narrow spectroscopic z-bin as a delta function located at $z = z_s$. This simplifies the calculation significantly, and the difference between using a bin of finite width (e.g. $\Delta z = 0.04$ as used previously) and a delta function was small. So for each distribution we have

$$\phi_s(z, z_s) = \delta(z - z_s) \tag{2.20}$$

$$\phi_p(z) = \frac{1}{\sqrt{2\pi\sigma_z^2}}\exp\left[-\frac{(z - \langle z\rangle)^2}{2\sigma_z^2}\right], \tag{2.21}$$

and using equation 2.18 we calculate their corresponding lensing kernels:

$$g_s(z, z_s) = \begin{cases} D(z)\dfrac{D(z_s) - D(z)}{D(z_s)}, & z \le z_s \\[2mm] 0, & z > z_s \end{cases}, \tag{2.22}$$

$$g_p(z) = \frac{D(z)}{\sqrt{2\pi\sigma_z^2}}\int_z^\infty \frac{D(z') - D(z)}{D(z')}\exp\left[-\frac{(z' - \langle z\rangle)^2}{2\sigma_z^2}\right]dz'. \tag{2.23}$$

Using equation 2.19 we can determine the signal due to the photometric sample being lensed by a spectroscopic bin at $z = z_s$:

$$
\begin{aligned}
w_{[s,l]p}(\theta, z_s) &= 3\Omega_m\left(\frac{H_o}{c}\right)^2\frac{2.5s_p - 1}{b_p}H(\gamma_{sp})\theta^{1-\gamma_{sp}}\int_0^\infty r_{0,sp}^{\gamma_{sp}}\,\phi_s(z, z_s)\frac{g_p(z)}{a(z)}D(z)^{1-\gamma_{sp}}dz \\
&= \left[3\Omega_m\left(\frac{H_o}{c}\right)^2\frac{2.5s_p - 1}{b_p}H(\gamma_{sp})r_{0,sp}^{\gamma_{sp}}\frac{g_p(z_s)}{a(z_s)}D(z_s)^{1-\gamma_{sp}}\right]\theta^{1-\gamma_{sp}}. \tag{2.24}
\end{aligned}
$$

The signal due to the spectroscopic bin being lensed by the photometric sample is written as

$$
\begin{aligned}
w_{s[p,l]}(\theta, z_s) &= 3\Omega_m\left(\frac{H_o}{c}\right)^2\frac{2.5s_s - 1}{b_s}H(\gamma_{sp})\theta^{1-\gamma_{sp}}\int_0^\infty r_{0,sp}^{\gamma_{sp}}\frac{g_s(z, z_s)}{a(z)}\phi_p(z)D(z)^{1-\gamma_{sp}}dz \tag{2.25} \\
&= \left[3\Omega_m\left(\frac{H_o}{c}\right)^2\frac{2.5s_s - 1}{b_s}H(\gamma_{sp})\int_0^{z_s} r_{0,sp}^{\gamma_{sp}}\,\phi_p(z)\frac{D(z_s) - D(z)}{a(z)D(z_s)}D(z)^{2-\gamma_{sp}}dz\right]\theta^{1-\gamma_{sp}}.
\end{aligned}
$$

To determine the slopes of the number counts of galaxies we assume the Schechter function for describing the number density of galaxies in the luminosity interval from L to $L+dL$ (Schechter, 1976),

$$N(L)dL = V^* \phi^* \left(\frac{L}{L^*}\right)^\alpha \exp\left[-\frac{L}{L^*}\right] dL, \tag{2.26}$$

where V^*, ϕ^* and L^* are fit parameters. This has been shown to be a reasonable approximation to the luminosity functions of typical galaxy samples (Johnston, 2011). Using equation 2.26 to calculate $s = d(\log N)/dm$ we obtain

$$s = \frac{d\log N}{dm} = \frac{d\log N}{dL}\frac{dL}{dm} = -0.4\left(\alpha - \frac{L}{L^*}\right). \tag{2.27}$$

For the case of the photometric sample being lensed by objects in the spec-z bin, $w_{[s,l]p}(\theta, z_s)$, the typical luminosity will be much less than L^*, as the photometric sample will go much fainter. Because of this we use the approximation $s_p \approx -0.4\alpha$ in equation 2.24. In practice s_p can be calculated from the sample, but for the purposes of this analysis we are just looking for an approximation of how the lensing signal compares to the cross-correlation due to physical clustering. For the case of objects in the spec-z sample being lensed by the photometric objects, $w_{s[p,l]}(\theta, z_s)$, typical luminosities of galaxies observed in spectroscopic surveys are $\sim L^*$ so we use the approximation $s_s \approx -0.4(\alpha - 1)$.

Recent literature has found typical values of the faint-end slope to be $-1.5 \lesssim \alpha \lesssim -0.5$ for various galaxy samples, with α differing for red (~ -0.5) and blue (~ -1.5) samples (Faber et al., 2007; Ryan et al., 2007; Loveday et al., 2012). For galaxy samples not separated by color $\alpha \sim -1.3$. For the linear bias factors, b_p and b_s, we expect them to be of order unity and so we set them both equal to 1 for baseline calculations. As seen in equations 2.24 and 2.26, both signals scale as b^{-1}. For the parameters of the power-law correlation function we use $\gamma = 1.6$ and $r_0 = 5h^{-1}Mpc$, which are typical values from the simulation used in the previous sections. Changing the power-law parameters had no effect on the strength of the lensing signal relative to the cross-correlation signal from physical clustering as described in the next section.

2.3.3 Comparison to the cross-correlation from physical clustering

Next we compare the induced correlation signal from lensing to the cross-correlation due to the physical overlap of the two distributions for the reconstruction technique. Using Limber's approximation for the distributions in equations 2.20 and 2.21 and a power-law assumption for ξ_{sp}, we calculate the cross-correlation signal due to the physical overlap of the samples:

$$
\begin{aligned}
w_{sp}(\theta, z_s) &= \int_0^\infty \phi_s(z, z_s)\phi_p(z)\frac{1}{dl/dz}dz \int_{-\infty}^{+\infty} \xi_{sp}\left(\sqrt{\pi^2 + D(z)^2\theta^2}\right) d\pi \\
&= H(\gamma_{sp})\theta^{1-\gamma_{sp}} \int_0^\infty r_{0,sp}^{\gamma_{sp}} \phi_s(z, z_s)\phi_p(z)\frac{D(z)^{1-\gamma_{sp}}}{dl/dz}dz \\
&= \left[H(\gamma_{sp})r_{0,sp}^{\gamma_{sp}} \phi_p(z_s)\frac{D(z_s)^{1-\gamma_{sp}}}{dl/dz|_{z=z_s}} \right] \theta^{1-\gamma_{sp}}.
\end{aligned} \tag{2.28}
$$

This cross-correlation due to physical clustering as a function of a spec-z bin at $z = z_s$ can be compared to the induced correlation from weak lensing using equations 2.24 and 2.26, for a given θ separation on the sky.

Figure 2.18 shows the induced correlation due to weak lensing for each of the terms described above compared to the cross-correlation signal from physical clustering for $\alpha = -1.3$. We have also included the signal due to the samples being lensed by dark matter in the foreground to show that this signal is many orders of magnitude weaker and can be ignored. Figure 2.19 shows each of the weak lensing signals compared to the cross-correlation signal for three values of α over the range found in real galaxy samples, $-1.5 \lesssim \alpha \lesssim -0.5$. Both lensing signals vary significantly over this range in α, making it important to constrain the slope of the number counts of galaxies when predicting the induced correlation due to lensing in real galaxy samples.

The signal from the photometric sample being lensed by the spec-z bin is the weaker of the two dominant contributions due to our assumption that the typical luminosity in the photometric sample is much smaller than L^*, making the pre-factor of $w_{[s,l]p}$ (eqn. 2.24) smaller compared to $w_{s[p,l]}$ (eqn. 2.26) for the same value of α (i.e. $s_p < s_s$ from equation 2.27). It is still significant enough to bias the parameters of the reconstructed redshift distribution determined from the cross-correlation signal, but it should be possible to remove this signal iteratively by using the initial reconstruction to predict the lensing signal and subtract it out.
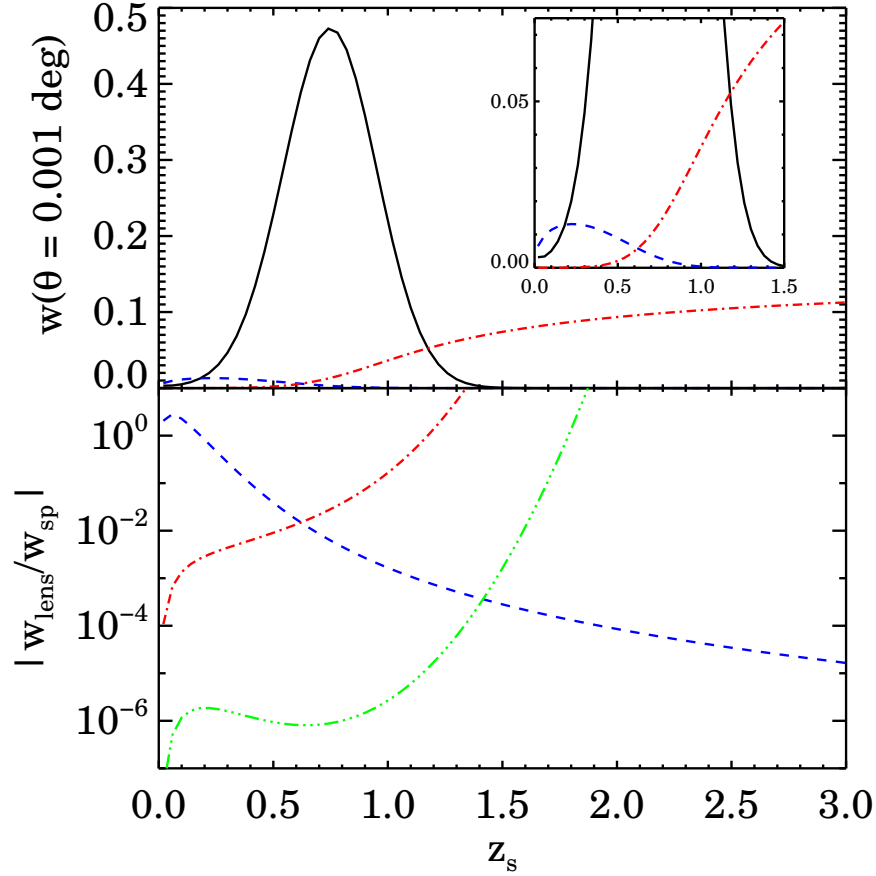
Figure 2.18 The top panel shows the cross-correlation, w_{sp}, of a spec-z bin at $z = z_s$ with a Gaussian photometric sample as a function of z_s (black line), compared to the signal from the photometric sample being lensed by objects in the spec-z bin, $w_{[s,l]p}$ (blue dash line), as well as the signal from the spec-z bin being lensed by the photometric objects, $w_{s[p,l]}$ (red dot-dash line), for $\alpha = -1.3$, a typical value for real galaxy samples. The bottom panel shows the ratio of each lensing signal to the cross-correlation. Both signals are significantly smaller than w_{sp}, but they are large enough to affect the recovery of $\phi_p(z)$ and will need to be accounted for when using real datasets. We also show the signal due to the lensing of spectroscopic and photometric objects by dark matter in the foreground of both samples to show that it is negligible compared to the other two lensing signals (green 3-dot-dash line).
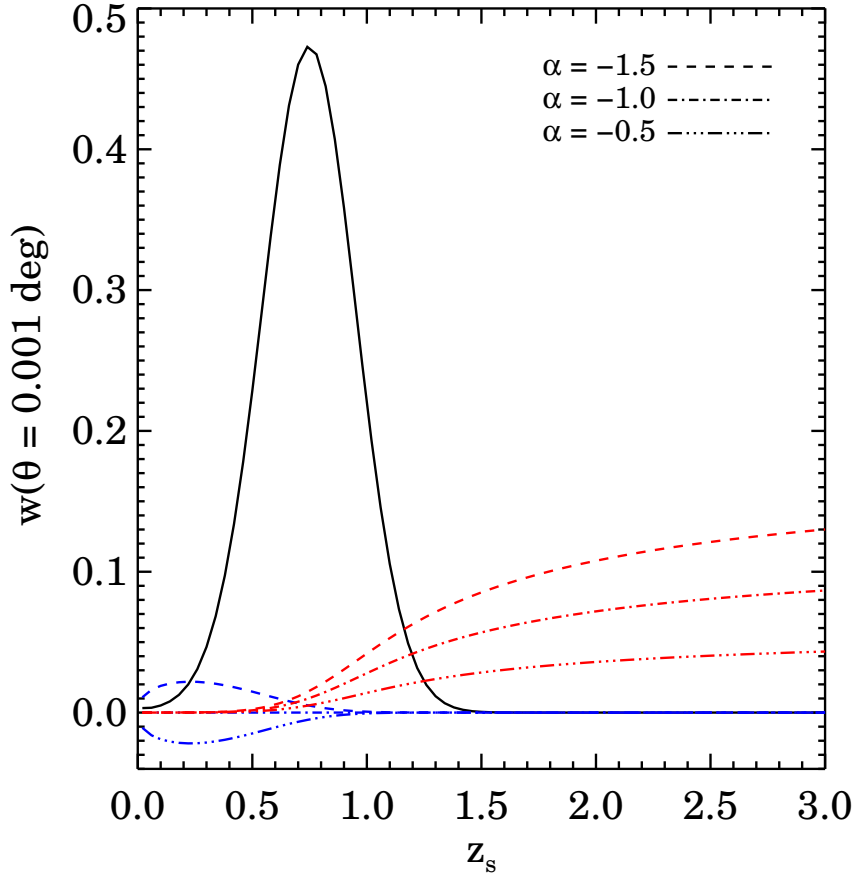
Figure 2.19 The cross-correlation, w_{sp}, of a spec-z bin at $z = z_s$ with a Gaussian photometric sample as a function of z_s (black line), compared to the signal from the photometric sample being lensed by objects in the spec-z bin, $w_{[s,l]p}$ (blue lines), as well as the signal from the spec-z bin being lensed by the photometric objects, $w_{s[p,l]}$ (red lines), for a range of values of α found in real galaxy samples. Changing α does have a significant effect on the strength of the induced correlation due to lensing, and so constraining the slope of the number counts of galaxies will be important in predicting the lensing signal in real samples.

The lensing signal from the objects in the spec-z bin being lensed by the photometric sample is stronger so it may need to be mitigated in other ways. One possibility is using a volume limited sample rather than a magnitude limited sample as this will eliminate the possibility of objects that are normally below the magnitude limit being included in the sample due to lensing magnification. Another possibility is to select a subsample of the spectroscopic objects that are evenly distributed on the sky for just the cross-correlation measurement. This will make it so the density of spec-z objects in a given region will not be allowed to increase due lensing effects.

This is only a rough calculation of the lensing signals and more refined calculations will need to be done which could vary depending on the properties of a particular dataset. But we can see from this that both of the lensing signals described above are significantly smaller than $w_{sp}(\theta)$, but they are large enough to affect the recovery of the parameters of $\phi_p(z)$ (e.g. $\langle z \rangle$ and σ_z). These signals will need to be accounted for and mitigated when applying the cross-correlation technique to real datasets in the future.

2.4   CONCLUSION

In this chapter we tested a technique for calibrating photometric redshifts that exploits the clustering of galaxies at similar redshifts using mock catalogs designed to match the DEEP2 Galaxy Redshift Survey. We found that by measuring the angular cross-correlation of a sample of galaxies that has secure and accurate spectroscopic redshifts with a sample of galaxies that only has photometric information in the same region of sky, we can obtain an accurate reconstruction of the redshift distribution of the photometric sample. We showed that the reconstruction can be improved by incorporating the full covariance information of the correlation measurements when fitting for the correlation function power-law parameters. We also found that the inversion of covariance matrices calculated from a small sample size can be unstable, and this instability can be mitigated by conditioning the covariance matrix using a "ridge regression" technique. We also estimated the impact of lensing magnification on the cross-correlation signal and discussed possibilities for reducing its effect.

There has been considerable other work done with reconstructing redshift distributions using the cross-correlation technique as well as its effect on the constraints of cosmological parameters. In Schulz (2010), cross-correlation techniques were applied to mock data generated by populating a single time slice of an N-body dark matter simulation using various halo models. They develop a pipeline for calculating the redshift distribution of a photometric sample using cross-correlation measurements and the autocorrelation of a spectroscopic sample, $\xi_{ss}(r, z)$. They do not attempt to model the bias although they do examine how varying the bias of the two samples affects the reconstruction (i.e. using radically different halo models). The catalogs constructed to test their method are significantly larger in volume than our individual mock catalogs, and while the number of objects in their photometric sample is comparable to ours, their spectroscopic sample is much smaller, which would be expected to lead to larger errors (Newman, 2008), as observed. Another major difference is the use of a smoothness prior in reconstruction, which was not done here. While Schulz (2010) found that cross-correlation techniques were generally successful in reconstructing redshift distributions, these conclusions were primarily qualitative due to the limited sample sizes and source densities of the mock samples used, along with less-optimal correlation measurement techniques. In this chapter, we have used simulations which include much less massive halos, allowing us to perform quantitative tests of cross-correlation techniques using sample sizes and source densities comparable to those which will be used in realistic applications.

Several techniques for calibrating photometric redshifts using only photometric data have also been developed (Schneider et al., 2006; Zhang et al., 2010; Benjamin et al., 2010; Quadri & Williams, 2010); in general, such techniques require priors or assumptions on biasing which can be relaxed or tested in spectroscopic cross-correlation measurements. In Quadri & Williams (2010), spectroscopic/photometric cross-correlation techniques have now been applied to real data using the COSMOS dataset. Using data from a single field, they are able to determine typical photo-z uncertainties well, even when ignoring the effects of bias evolution. However, when constraining catastrophic photo-z errors, methods which ignore these effects should break down, as bias evolution should be a much greater problem over broad redshift intervals than in the core of the photo-z error distribution.

3.0 CONSTRAINING THE INTERLOPER FRACTION USING CROSS-CORRELATION

The study of high redshift galaxies is important for our understanding of the Universe as it gives insight into the early stages of galaxy evolution. Advances in telescope technology and observational techniques in the last decade have made the study of the first billion years of the history of galaxy evolution possible, including the clustering of high redshift galaxies (e.g. Ouchi et al. 2001, 2004, 2010; Jose et al. 2013), the evolution of their luminosity function and star formation rates (e.g Ouchi et al. 2008; Bouwens et al. 2007, 2008, 2012), as well as the epoch of reionization when early galaxies ionized the surrounding neutral hydrogen (e.g. Ouchi et al. 2010; Bunker et al. 2010; Yan et al. 2010). One of the key challenges in observational cosmology is identifying these high redshift objects from photometric measurements so they may be selected out from larger datasets for further study. Various techniques have been developed for distinguishing high redshift objects in photometric datasets. A common approach is to look for photometric "drop-out", or objects with significant decreases in flux in adjacent bands, indicating a spectral break (Bouwens et al., 2006, 2007; Yan et al., 2010, 2012). For example, in some high redshift galaxies there is a spectral feature at 1216 Å due to Lyman-α absorption, where there is a significant drop in flux shortward of this wavelength. At a redshift of 6 this feature is seen in the infrared at ~ 8500 Å. For the common $ugriz$ photometric system consisting of 5 passbands covering wavelengths from the visible to the near-infrared, the z-band is centered around 8500 Å and the i-band is centered at a shorter wavelength ~ 7750 Å, and so for a given galaxy if there is a significant decrease in flux in the i-band compared to the z-band, it is likely due to this spectral break and the galaxy becomes a high redshift candidate. Work has also been done with selecting high-z objects using template fitting photometric redshift measurements (McLure et al., 2011; Finkelstein

et al., 2012).

One potential issue with selecting high redshift objects using these techniques is contamination of the sample from lower redshift objects whose photometry resembles that of the high-z objects, e.g. confusing the 4000 Å break in low-z galaxies with the Lyman break. In the past, these interlopers have generally been identified via extremely deep imaging at other bands or via spectroscopy (Shimasaku et al., 2003; Kovač et al., 2007). However, due to long exposure times required for deep imaging and spectroscopy, both of these avenues become less practical for faint dropout samples. A powerful alternative is to exploit the clustering of galaxies to determine the interloper fraction. Low-z interlopers will cluster with easier-to-identify, bright low redshift objects, whereas true high-z galaxies will not. Hence, by measuring the two-point angular cross-correlation between objects in a sample of high-z candidates and objects with known spectroscopic redshifts, we can constrain the interloper fraction even if it includes objects too faint for spectroscopy.

In this chapter we describe how to calculate the interloper fraction from the cross-correlation of a high-z candidate sample with a low-z spectroscopic sample. In §3.1.1 we derive the relation between the interloper fraction and the observables along with the other unknown quantities that will need to be modeled in order to constrain the interloper fraction. In §3.1.2 we describe the calculation of the uncertainty in the interloper fraction as a function of the modeled parameters, and in §3.1.3 we present the results of this error analysis. In §3.2 we conclude.

3.1   METHOD

There are two samples of galaxies used in this calculation. The high redshift candidate sample consisting of objects identified as being at high redshift via some method, e.g. photometric dropout techniques, and a low redshift spectroscopic sample that has secure and accurate redshifts. For the purposes of this calculation we assume that the high-z candidate sample has a redshift distribution described by two top hat distributions widely separated in redshift, with a low-z spectroscopic sample, also a top hat distribution, overlapping the interlopers in

z. Figure 3.1 shows an example of the two distributions. The observables used are the two point angular autocorrelation of the high-z sample, $w_{pp}(\theta)$, and the two point angular cross-correlation of the spectroscopic sample with the high-z sample, $w_{sp}(\theta)$, where the angular correlation function is defined in §2.1.2.
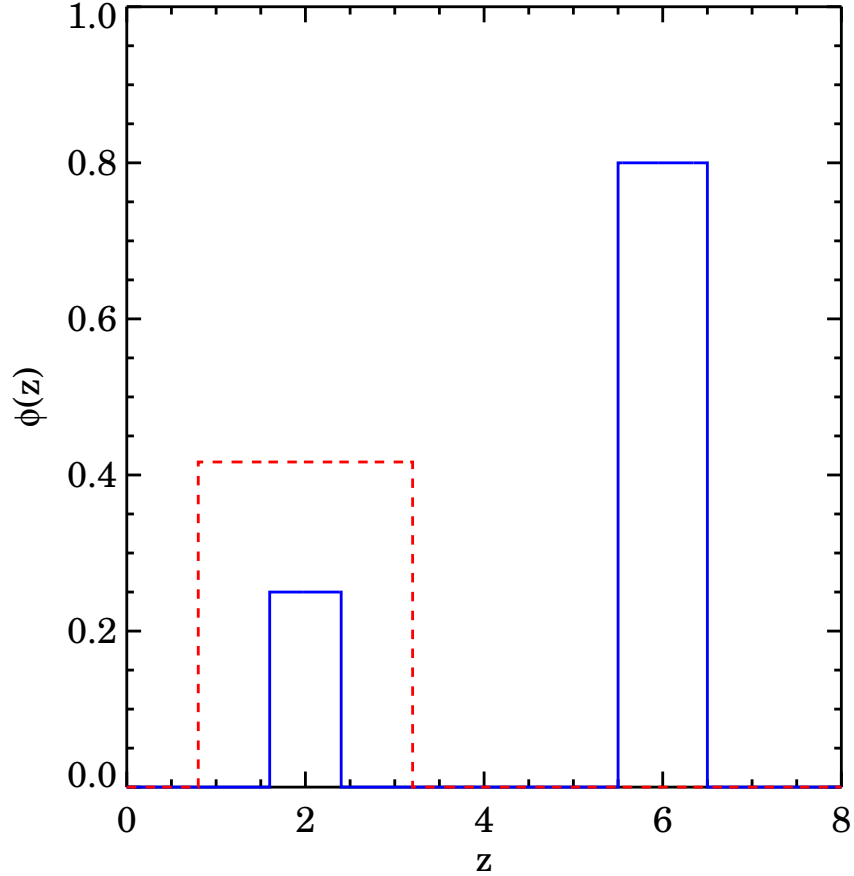
Figure 3.1 An toy model example of a high redshift sample contaminated with interlopers (solid blue line), along with a low redshift spectroscopic sample that only overlaps the interlopers (dashed red line). For the calculation we assume top hat distributions for both samples.

3.1.1 Observables and the Interloper Fraction

Writing the angular autocorrelation function for an angular separation θ in terms of the density contrast, $\delta(\theta) = (\rho(\theta) - \langle\rho\rangle)/\langle\rho\rangle$, which describes the 2-D dimensionless density

perturbation field gives

$$w_{pp}(\boldsymbol{\theta}) = \langle \delta_p(\boldsymbol{\theta_o})\delta_p(\boldsymbol{\theta_o} + \boldsymbol{\theta}) \rangle, \qquad (3.1)$$

(Peebles, 1980) where the angle brackets indicate an average over a solid angle Ω. The 2-D perturbation field will have contributions from both low and high redshift perturbations, and writing it in terms of these components gives

$$\delta_p = f_i\delta_i + (1 - f_i)\delta_h, \qquad (3.2)$$

where f_i is the interloper fraction, and δ_i and δ_h are the density contrasts associated with the low-z interlopers and the objects truly at high redshift, respectively. Putting this into equation 3.1 and expanding gives

$$w_{pp}(\boldsymbol{\theta}) = f_i^2\langle\delta_i\delta_i'\rangle + (1 - f_i)^2\langle\delta_h\delta_h'\rangle + f_i(1 - f_i)\left[\langle\delta_i\delta_h'\rangle + \langle\delta_h\delta_i'\rangle\right] \qquad (3.3)$$

where the " $'$ " indicates the density contrast at $\boldsymbol{\theta_o}+\boldsymbol{\theta}$ (equation 3.1). By comparing to equation 3.1 we see that the two quantities $\langle\delta_i\delta_h'\rangle$ and $\langle\delta_h\delta_i'\rangle$ are simply the angular cross-correlation of the low redshift interlopers with the objects truly at high redshift, and thus are zero since the interlopers and high-z objects are widely separated in redshift and not physically associated with each other. Also analogous to equation 3.1, the quantity $\langle\delta_i\delta_i'\rangle$ is the autocorrelation of only the low-z interlopers, w_{ii}, and $\langle\delta_h\delta_h'\rangle$ is the autocorrelation of the objects truly at high redshift, w_{hh}. So for the angular autocorrelation of the high-z candidate sample we can write

$$w_{pp}(\theta) = f_i^2 w_{ii} + (1 - f_i)^2 w_{hh}. \qquad (3.4)$$

Similarly, for the cross-correlation of the low-z spectroscopic sample with the high-z candidate sample we can write

$$w_{sp}(\boldsymbol{\theta}) = \langle \delta_s(\boldsymbol{\theta_o})\delta_p(\boldsymbol{\theta_o} + \boldsymbol{\theta}) \rangle. \qquad (3.5)$$

Using equation 3.2 it can be shown that

$$w_{sp}(\boldsymbol{\theta}) = f_i\langle\delta_s\delta_i'\rangle + (1 - f_i)\langle\delta_s\delta_h'\rangle. \qquad (3.6)$$

69

Again comparing to equation 3.1 we see that $\langle \delta_s \delta_i' \rangle$ is the angular cross-correlation of the low-z spectroscopic sample with just the interlopers, w_{si}, and $\langle \delta_s \delta_h' \rangle$ is the cross-correlation of the spectroscopic sample with the objects truly at high redshift, w_{sh}. The second term will be zero, again because the spec-z sample and objects at high-z in the candidate sample are widely separated in redshift. So for the cross-correlation of the spectroscopic sample with the high-z candidate sample we can write:

$$w_{sp}(\theta) = f_i w_{si}. \tag{3.7}$$

There will also be a contribution to the measured cross-correlation from weak gravitational lensing where the high-z objects are lensed by the low-z spectroscopic sample, as described in §2.3. In general this induced correlation will be small compared to the true w_{sp}, although as the interloper fraction gets smaller its relative contribution will increase. However, the lensing signal will mainly contribute to uncertainty in w_{sp}, and as we describe in §3.1.2.1 this uncertainty is not the dominant factor in the error in f_i.

By modeling the real-space two-point correlation function, $\xi(r)$, as a power law (i.e. $\xi(r) = (r/r_0)^{-\gamma}$), it is possible to determine an analytic solution to the relation between w_{si} and the redshift distribution of the interlopers. Using Limber's approximation with the power law assumption we can write

$$w_{si} = H(\gamma_{si})\theta^{1-\gamma_{si}} \int_0^\infty \phi_s(z)\phi_i(z)r_{0,si}^{\gamma_{si}}\frac{D(z)^{1-\gamma_{si}}}{dl/dz}dz \tag{3.8}$$

(Peebles, 1980), where $H(\gamma) = \Gamma(1/2)\Gamma((\gamma-1)/2)/\Gamma(\gamma/2)$ ($\Gamma(x)$ is the standard Gamma function), and $\phi_s(z)$ and $\phi_i(z)$ is the probability distribution function for the redshifts of the spectroscopic sample and interlopers respectively. The angular size distance, $D(z)$, and the comoving distance to redshift z, $l(z)$, can be determined from the basic cosmology, but as we see later, these quantities are not present in our final expression used for determining f_i. The parameters $r_{0,si}$ and γ_{si} are the power-law parameters that characterize the intrinsic clustering of the interlopers with the low-z spectroscopic sample.

The redshift distribution of the interlopers can also be related to the angular autocorrelation of the interlopers, w_{ii}, through Limber's equation as

$$w_{ii} = H(\gamma_{ii})\theta^{1-\gamma_{ii}} \int_0^\infty \phi_i^2(z)r_{0,ii}^{\gamma_{ii}}\frac{D(z)^{1-\gamma_{ii}}}{dl/dz}dz, \tag{3.9}$$

70

where $r_{0,ii}$ and γ_{ii} are the power-law parameters for the autocorrelation of the interlopers. Combining equations 3.8 and 3.9 and using top-hat redshift distributions for ϕ_i and ϕ_s, with widths Δz_i and Δz_s and assuming $\Delta z_s \geq \Delta z_i$ (as seen in figure 3.1), it can be shown that

$$w_{ii} \approx \frac{r_{0,ii}^{\gamma_{ii}}}{r_{0,si}^{\gamma_{si}}} \left[\frac{\int_0^\infty \phi_i^2(z)dz}{\int_0^\infty \phi_s(z)\phi_i(z)dz} \right] w_{si} = \frac{r_{0,ii}^{\gamma_{ii}}}{r_{0,si}^{\gamma_{si}}} \frac{\Delta z_s}{\Delta z_i} \frac{w_{sp}}{f_i} \tag{3.10}$$

where we have used equation 3.7 to relate w_{si} to the observable w_{sp}. For the following calculations we set $\Delta z_s = \Delta z_i$, but in principle the quantity in brackets would need to be calculated for each particular case to obtain an accurate value for f_i. The quantity $r_{0,ii}^{\gamma_{ii}}/r_{0,si}^{\gamma_{si}}$ is essentially the ratio of the bias of the interlopers to the spec-z sample bias, where the bias is the proportionality relating the spatial distribution of galaxies and the underlying dark matter density field. If we define the quantity $b_r = r_{0,ii}^{\gamma_{ii}}/r_{0,si}^{\gamma_{si}}$, and combine equations 3.4 and 3.10 we obtain

$$w_{pp} = f_i b_r w_{sp} + (1 - f_i)^2 w_{hh} \tag{3.11}$$

This gives a relation between the interloper fraction, f_i, and our observables w_{pp} and w_{sp}. If we can accurately model the bias ratio, b_r, and the angular autocorrelation of a pure high-z sample with no interlopers, w_{hh}, we can determine the fraction of interlopers in the sample.

3.1.2 Uncertainty in f_i

We looked at how the uncertainty in the interloper fraction, f_i, scales with the uncertainty in the two parameters that must be modeled, b_r and w_{hh}. For all calculations we assume the uncertainty in the observables, w_{pp} and w_{sp}, are small compared to the uncertainty in the modeled parameters. We employ two separate approaches for calculating the uncertainty in f_i: first we determine an analytical solution by applying simple propagation of errors to equation 3.11 and then compare the results to a Monte Carlo simulation.

3.1.2.1 Analytical Solution Applying propagation of errors to equation 3.11 assuming that all uncertainties are in the two parameters that must be modeled gives

$$\sigma_{f_i}^2 = \frac{f_h^2}{4\left(1 - \frac{1}{2}\frac{f_i}{f_h}\frac{w_{ii}}{w_{hh}}\right)^2} \left[\frac{\sigma_{w_{hh}}^2}{w_{hh}^2} + \left(\frac{w_{ii}}{w_{hh}}\right)^2 \left(\frac{f_i}{f_h}\right)^4 \frac{\sigma_{b_r}^2}{b_r^2} \right] \tag{3.12}$$

where f_h is just $1 - f_i$. For small f_i we see that the second term within the brackets is small compared to the first, so in this regime the uncertainty in the modeled autocorrelation of a pure high-z sample is going to dominate the uncertainty in f_i, with σ_{f_i} approximately half of the fractional error in w_{hh}. We must also characterize the quantity w_{ii}/w_{hh}, but this factor also becomes less important in the limit of small f_i. This ratio of the clustering strength at low and high redshift is expected to be of order unity, in part because the comoving clustering scale length (i.e. r_0) for galaxy populations does not vary strongly with redshift, as has been observed in galaxy samples at various redshifts (e.g. Coil et al. 2008; Ouchi et al. 2004). In addition, the comoving separations used in calculating the correlation function at the low and high redshifts of interest only differ by at most a factor of a few. Because of this we set this ratio of the correlation functions equal to 1 for all calculations in this paper.

We note that if we apply propagation of errors on all quantities in equation 3.12, the uncertainty in w_{sp} will not significantly contribute to the uncertainty in f_i, as it will have similar dependence as the bias ratio b_r (i.e. it will have a factor of $(f_i/f_h)^4$ in front of the fractional error in w_{sp}). As we described in §3.1.1, this reduces the impact of the uncertainty in w_{sp} due to the induced correlation from weak lensing.

3.1.2.2   Monte Carlo simulations   For the Monte Carlo simulation the inputs are the true value of f_i we are trying to recover, as well as nominal values for the mean b_r and w_{hh}. We then use equations 3.4 and 3.11 to calculate mean values of w_{pp} and w_{sp}, where we set $w_{ii}/w_{hh} = 1$. The results of our analysis are insensitive to changes in the mean values of b_r and w_{hh}. By fixing w_{pp} and w_{sp} at their mean values and adding random Gaussian noise to $\langle b_r \rangle$ and $\langle w_{hh} \rangle$, we can then apply equation 3.11 to calculate the resulting f_i for a large number of simulations.

In the MC simulation, for each value of $\sigma_{w_{hh}}/w_{hh}$ and σ_{b_r}/b_r we generate 10^7 realizations and solve equation 3.11 for each. Since equation 3.11 is quadratic in f_i, for large uncertainties the random noise can cause some of the realizations to give non-real solutions for f_i, and ignoring these realizations would highly bias our results. For this reason we treated b_r and w_{hh} as lognormal variables where we instead added random noise to $\ln x$ with $\sigma_{\ln x} = \sigma_x/\langle x \rangle$. For small f_i, this gave stable results with no non-real solutions even for large uncertainties.

For larger values of f_i ($\gtrsim 0.5$) we ran into other issues which we describe later.

For each set of 10^7 realizations, we make robust measurements of the bias and uncertainty in f_i. To determine the recovered f_i from the MC simulation we take the median of the 10^7 realizations. We use the median to reduce the impact of outliers, and also because for random variables with lognormal distributions the median is an unbiased estimator of the mean of an equivalent random Gaussian distribution. To calculate the bias we simply subtract this median from $f_{i,\text{true}}$, the true value of the interloper fraction we initially input into the simulation. We determined the uncertainty using the IDL function DJSIG[1] that can occur at a significant ($\sim 1\%$) rate (Sun et al., 2009; Bernstein & Huterer, 2010), which calculates the standard deviation with iterative sigma clipping, reducing the impact of outliers.

3.1.3   Results

Since the error in w_{hh} will be the dominant factor in the error in f_i, for the following analysis we fix the fractional error of the bias ratio, σ_{b_r}/b_r, and look at how varying the fractional error in the modeling of the autocorrelation of a pure high-z sample, $\sigma_{w_{hh}}/w_{hh}$, affected the uncertainty in f_i.

Figure 3.2 shows the bias and uncertainty in f_i as a function of the fractional error in w_{hh}, for f_i=0.1 and 0.4, where we have set $\sigma_{b_r}/b_r = 0.10$. For f_i=0.1 we see that the recovered interloper fraction is unbiased, even out to large fractional error in w_{hh}. As the interloper fraction gets larger we start to see a very small systematic bias. This is likely due to the bias that results when adding variables with lognormal distributions, as is necessary when solving equation 3.11 for f_i. The sum of lognormal variables is not exactly lognormal, and the recovered median of the sum is biased compared to the sum of the individual medians. The magnitude of this bias depends on the properties of each distribution, particularly the uncertainty $\sigma_{\ln x}$. However, for the values of interest in this analysis, the bias on the median of the sum is generally at the sub-percent level, much smaller than the expected uncertainties in the modeled parameters. This bias is not apparent for the case of f_i=0.10, because for small f_i, i.e. a weak cross-correlation signal, the terms in the solution for f_i that contain b_r

---

[1]Part of the IDLUTILS package available at `http://www.astro.princeton.edu/~schlegel/code.html`.
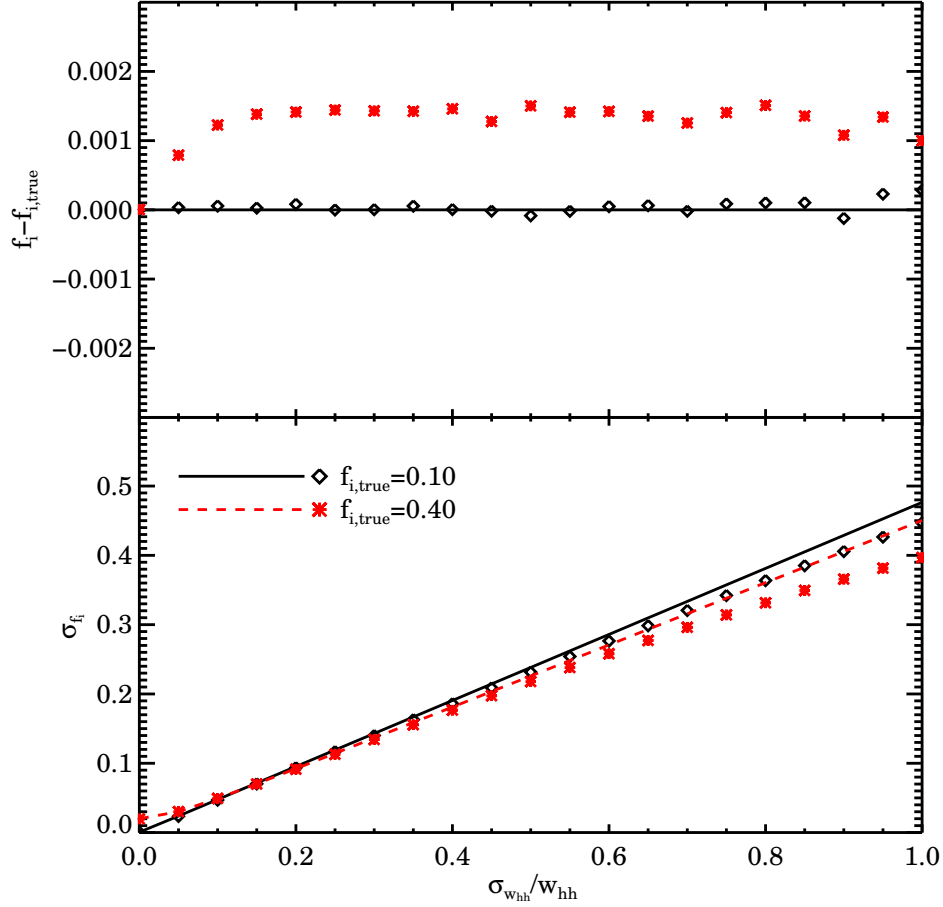
Figure 3.2 The top panel shows the bias of the interloper fraction, f_i, recovered from the Monte Carlo simulation described in §3.1.2.2 as a function of the fractional error in w_{hh} for two values of f_i. As f_i gets larger there is a systematic bias in the recovered f_i from summing lognormal variables as described in §3.1.3, although this bias is much smaller than the uncertainty in f_i. The bottom panel shows the uncertainty in f_i as a function of the fractional error in w_{hh} for both the analytic solutions (solid and dashed lines), and the Monte Carlo simulation results (points), for the same two values of f_i. Especially for small values of f_i, the uncertainty does not strongly depend on the value of f_i.

are small compared to the term that contains only w_{hh}, and so this bias is negligible. As f_i becomes larger, the b_r terms become significant, which leads to the bias from summing lognormal variables. In any case, for reasonable values of the fractional uncertainty in b_r this bias is small compared to the expected uncertainty in f_i.

From the plot of the uncertainty in f_i we see that for $\sigma_{w_{hh}}/w_{hh} \lesssim 0.6$ the analytical solution closely follows the results of the Monte Carlo simulation, and above that they diverge slightly. We also see in this same range that the uncertainty is not strongly sensitive to changes in f_i. This shows that if we can determine the modeled autocorrelation of a pure high-z sample to $10 - 30\%$, then the uncertainty in the interloper fraction will be $\sigma_{f_i} \sim 0.05 - 0.15$ over a wide range in f_i. As the interloper fraction increases above ~ 0.5 we again run into issues with non-real solutions in the MC simulation, as well as the coefficient in front of equation 3.12 blowing up in this range due to the denominator going to zero. We found this calculation to be reliable up to $f_i \sim 0.5$, which is well above the expected interloper fraction in a given high-z candidate sample.

3.2 CONCLUSION

In this chapter we have shown that the level of contamination of a high redshift candidate sample by low redshift interlopers can be constrained by cross-correlating the high-z sample with galaxies at low redshift that have secure and accurate redshifts. We found that in addition to measuring the angular cross-correlation of the two samples and the angular auto-correlation of the high-z candidate sample, it will also be necessary to model the ratio of the bias of the interlopers to the bias of the spectroscopic sample, as well as the autocorrelation of a pure high-z sample with no contaminants.

We also found that the uncertainty in the modeled autocorrelation of the pure high-z sample will be the dominant source of error when determining the interloper fraction. Some work has previously been done to model the the clustering of high redshift galaxies. In Jose et al. (2013) they use a physically motivated semi-analytic model to predict the clustering of high redshift Lyman-α emitters. They predict the 2-D autocorrelation function, $w(\theta)$,

for Ly-α emitters at $z = 6.6$ and find and are able to reproduce the observations in Ouchi et al. (2010), although as we discuss later, the sample used in Ouchi et al. (2010) is not necessarily a pure high-z sample. Constraining the interloper fraction more tightly should lead to a better comparison to the models, with the possibility of iteratively removing the contribution of the interlopers using a first estimation of $w_{hh}=w_{pp}$.

A related method was applied in Morrison et al. (2012) as a null test where they cross-correlated a $z \sim 4$ sample of Lyman break galaxies from the Deep Lens Survey with lower redshift ($z \sim 0.2-1$) spectroscopic objects from the PRIMUS survey (Coil et al., 2011). They had removed possible contaminants of the high-z sample by other means and were simply testing for interlopers via cross-correlation and measured no signal, indicating that there was not significant contamination of the high-z sample. This just showed that the contamination was either nonexistent or was too small to detect given their measurements. With improved measurements and modeling of clustering parameters, the technique described in this chapter will be able to constrain the value of f_i to greater accuracy.

Previous attempts to constrain the interloper fraction have generally not been successful or have been subject to large uncertainties. For example in Ouchi et al. (2010) they measured the properties of 207 Lyman-α emitters at $z = 6.6$ which were selected by looking for excess flux in a narrow band filter centered at 9192 Å, compared to deep broadband imaging. They selected 30 of the objects for follow-up spectroscopy and were able to obtain secure spectroscopic redshifts for 19 of them. None of the 19 were determined to be interlopers, and by reasoning that any of the objects that they were unable to obtain spectroscopic redshifts for could possibly be low-z interlopers they estimated the interloper fraction as ranging anywhere from 0-30%. However, a measured interloper fraction of 11/30 is consistent at 2σ significance with an interloper fraction as large as 55%. As high-z candidate samples go fainter obtaining spectroscopy becomes even more difficult, and so being able to constrain the interloper fraction to ± 0.10-0.15 would be a significant improvement.

4.0 EXTENDED PHOTOMETRY FOR THE DEEP2 GALAXY REDSHIFT SURVEY: A TESTBED FOR PHOTOMETRIC REDSHIFT EXPERIMENTS

Future wide-area photometric surveys will obtain imaging for a very large number of galaxies ($\sim 10^8 - 10^9$), and many of the cosmological measurements to be performed with this data will require redshift information for these objects. It is not feasible to measure spectroscopic redshifts for this many objects, mainly due to the integration time required to obtain spectra, and in addition, many of the galaxies are too faint for spectroscopy. As an example, to follow up the 3×10^9 $i < 25.3$ mag galaxies from LSST with a 10-m telescope that could take 5,000 spectra at once would take $\sim 35,000$ years (Newman et al., 2013a). This is clearly not a practical human endeavor. To meet this challenge, many techniques have been developed for estimating redshifts from photometric information, where the flux from the galaxy is measured in a few broadband filters. Because our knowledge of the true spectral energy distributions of the full range of galaxies is limited, a training set of objects with accurate spectroscopic redshifts is generally used to determine or refine relations between photometric observables and z (e.g., Connolly et al. 1995; Gerdes et al. 2010; Ilbert et al. 2006). However, the combination of deep photometry in many bands with deep spectroscopy for calibration purposes is available in only a few fields.

The DEEP2 (Deep Extragalactic Evolutionary Probe 2) Galaxy Redshift Survey (Newman et al., 2013b) obtained secure and accurate redshifts for more than 38,000 objects in four widely separated fields. However, the photometry used for DEEP2 targeting was obtained in the B, R, and I filters, while the deepest datasets to date utilize measurements in $ugriz$. We have now constructed a catalog combining DEEP2 spectroscopic redshifts with data from two $ugriz$ photometric surveys which have covered the same fields: the Canada-France-Hawaii Legacy Survey (CFHTLS) (Gwyn, 2012) and the Sloan Digital Sky

Survey (SDSS) (Ahn et al., 2012; Abazajian et al., 2009). In this chapter, we present the details of this catalog and make it publicly available as a testbed for algorithm development for future photometric redshift studies. These catalogs can be downloaded at http://deep.ps.uci.edu/DR4/photo.extended.html.

In §4.1 we describe the three different data sets used to construct this catalog. This new catalog also provides astrometry tied to SDSS DR9 (rather than USNO-A2.0) as a reference; the corrections required are described in §4.2. In §4.3.1 we describe how we constructed the catalog for DEEP2 Field 1, commonly known as the Extended Groth Strip (EGS). In the course of this we derive improved photometric calibrations for CFHTLS photometry in all pointings that overlap DEEP2 Field 1 (§4.3.1.1). We also determine color transformations between the DEEP2 BRI and the CFHTLS $ugriz$ photometric systems for this field, allowing us to use CFHTLS data to predict BRI magnitudes for a subset of DEEP2 objects which had poorer measurements originally (§4.3.1.2). In §4.3.2 we describe how we constructed the combined $ugriz$/redshift catalog for DEEP2 Fields 2, 3, and 4. In §4.4 we provide details of the parameters that are included in the resulting catalogs, and in §4.5 we conclude and provide summary statistics for this new sample.

4.1   DATA SETS

The DEEP2 Galaxy Redshift Survey is a magnitude-limited spectroscopic survey of objects with $R_{AB} < 24.1$ (Newman et al., 2013b). Data was taken in four separate fields, with photometry in each field from CFHT 12K BRI imaging (the *"pcat"* catalogs). Subsets of each *pcat* catalog were targeted for spectroscopy in order to obtain redshifts (the *"zcat"* catalogs). DEEP2 Field 1 is part of the Extended Groth Strip (EGS), where the *pcat* photometry was measured in four overlapping $0.5° \times 0.7°$ pointings of the 12K camera (labeled as pointings 11-14). For the DEEP2 spectroscopic survey in this field (*zcat* catalog), objects were targeted in a $0.25° \times 2.0°$ window which spans all four pointings. In DEEP2 Fields 2, 3, and 4, the *pcat* and *zcat* catalogs cover the same area on the sky, where data was taken in $0.5° \times 2.0°$ rectangular fields, with each field divided up into three separate pointings (labeled as 21-23,

etc.). In Field 2, pointing 23 is not included in this catalog since it was not observed with the DEIMOS spectrograph in DEEP2 and also has inferior BRI photometry. We include all of pointing 43 in Field 4 in this catalog although only part of this pointing was actually observed with DEIMOS and have redshifts. See Coil et al. (2004) and Newman et al. (2013b) for details of both the *pcat* and *zcat* catalogs.

To provide *ugriz* photometry for objects in DEEP2 Field 1, we used the publicly-available CFHTLS Wide Field *i*-band selected unified catalog, as well as the CFHTLS Deep Field *i*-band selected catalog (Gwyn, 2012) where it overlaps the DEEP2 pointings. Photometry was obtained using the wide field optical imaging camera MegaCam. We selected objects in the Wide catalog from the seven pointings that overlap DEEP2 Field 1 (each pointing $\sim 0.9° \times 0.9°$), where each *ugriz* band reaches depths of $u = 24.6 - 25.8$, $g = 26.0 - 26.4$, $r = 25.2 - 26.2$, $i = 24.7 - 25.2$, and $z = 23.8 - 24.8$ (span shows the range of depths over all seven pointings). Here we have defined the depth in each pointing as the magnitude at which the errors in each band correspond to a 5σ flux measurement. The CFHTLS Deep Field D3 ($\sim 1.0° \times 1.0°$) partially overlaps DEEP2 pointings 11-13 and reaches depths of $u = 27.1$, $g = 27.7$, $r = 27.5$, $i = 27.2$, and $z = 25.7$. For the *ugriz* magnitudes we used the Kron-like elliptical aperture magnitudes designated by MAG_AUTO in the catalog.

For *ugriz* photometry in DEEP2 Fields 2-4 we used data from the SDSS catalogs. Where SDSS overlaps DEEP2 Field 2 we select both stars and galaxies that are flagged as having clean photometry in the DR9 data release (Ahn et al., 2012). Where SDSS overlaps DEEP2 Fields 3 and 4 we select sources flagged as having clean photometry in Stripe 82, which goes deeper than typical SDSS fields due to co-adding repeated imaging scans (designated by runs 106 and 206 in the Stripe82 database in DR7) (Abazajian et al., 2009). In all three fields we use model magnitude photometry. The depths reached for DR9 (Stripe 82) objects that overlap DEEP2 Fields 1 and 2 (3 and 4) are given by $u = 21.6 - 22.1$ $(23.3 - 23.5)$, $g = 23.0 - 23.2$ $(24.7 - 24.8)$, $r = 22.7 - 23.1$ $(24.3 - 24.5)$, $i = 22.0 - 22.5$ $(23.8 - 23.9)$, and $z = 20.5 - 20.9$ $(22.0 - 22.4)$.

4.2 CORRECTED ASTROMETRY

The DEEP2 astrometry measurements were determined using stars from the USNO-A2.0 system. The USNO-A2.0 astrometry contained a number of known systematic errors, which have been propagated into the DEEP2 astrometry. Additionally, the `imcat`-produced data reductions (Kaiser et al., 1999; Kaiser, 2011) tend to have larger systematic astrometric errors at the edges of each pointing, presumably due to a lack of astrometric calibration stars beyond field edges. The net result is that systematic astrometric errors vary over scales of $5-10'$, and can reach values of $\sim 1''$ in the worst cases. It should be noted that these errors are referring to the absolute astrometry, and the relative astrometry at small scales ($\lesssim 1'$) will be much more accurate than this. For objects separated by more than $1'$, there will be systematic offsets in the relative astrometry increasing with separation. In addition, the public *pcat* catalogs for field 1 (EGS) that are available do include an astrometric correction that ties them to SDSS, and so the absolute astrometry is better than this in those catalogs. For consistency in these catalogs, we perform the same astrometric corrections in all fields, including field 1.

In order to allow improved comparisons to external catalogs, we have calculated corrected astrometry for each object in DEEP2 using the superior absolute astrometry from SDSS as a reference frame rather than USNO-A2.0. The SDSS astrometry is calibrated against the Second Data Release of USNO CCD Astrograph Catalog (UCAC2), which measured the positions and proper motions for millions of stars, where the precision of measured positions are $\sim 15 - 70$ mas, with systematics estimated to be < 10 mas (Zacharias et al., 2004). For consistency in the catalog, we also performed corrections on the CFHTLS astrometry. The size and direction of the deviations from the SDSS astrometry varied significantly across each DEEP2 pointing; therefore, it was necessary to calculate a correction which is dependent upon position, rather than a single offset.

In each pointing of each field we first identified matching objects between DEEP2 and SDSS. This was done by selecting each DEEP2 object and searching for SDSS objects within a given search radius, and in cases where multiple matches are found, the closest object is selected as the match. This general matching procedure was used for all catalog matching.

For most all matching procedures we used a search radius of $0.75''$, as that is approximately the resolution in the DEEP2 survey. However, for the astrometric corrections, we used a larger initial search radius of $1''$ to allow for systematic errors. For every matched pair of DEEP2 and SDSS objects, we calculated $RA - RA_{SDSS}$ and $dec - dec_{SDSS}$ on a grid by binning in RA and dec and calculating the median difference between DEEP2 and SDSS astrometry in each bin. For any bins where these differences are poorly constrained, i.e. too few objects to compute a median or with the error in the bin $\gtrsim 0.5''$ (of order the typical correction factor), we instead use values interpolated from adjoining bins. We then smoothed the gridded offsets to obtain the required corrections to be applied to the original RA and dec values in each pointing to bring them onto the SDSS reference frame. The correction factors for each object were calculated by interpolating on the smoothed grid of values; the results were subtracted from the original positions to yield SDSS-equivalent positions. The refined astrometry was then used to re-match catalogs using our standard $0.75''$ search radius. These corrections resulted in a significant increase in the number of matches found between the two catalogs, ranging from ~ 40–60 more matches in the shallow SDSS pointings (an increase of ~ 150 matches per square degree to a depth of $r \approx 22.8$ mag in those fields), up to thousands of matches in some of the deeper fields (~ 3000 matches per square degree to a depth of $r \approx 25.2$ mag). We investigated iterative refinement of the corrections using this closer match radius beyond the first iteration, but the results did not show significant improvement.

Ideally, we would like to perform corrections which can vary on very small scales, in order to capture all possible structure in the astrometric offsets. However, that would cause only a few objects to be used to determine the correction at any given position, yielding noisy results. We therefore must adopt a grid scale which balances these two needs. In order to determine how finely we should bin in RA and dec in order to accurately describe the real deviations at a given position without excessive noise due to using only a small set of objects, we investigated how varying the number of bins we divided the pointing area into affected the rms variation in $RA - RA_{SDSS} - \Delta_{RA}$ and $dec - dec_{SDSS} - \Delta_{dec}$ for all matches, where Δ is the correction factor described above. We repeated the calculation while increasing the number of bins, and in each case smoothed the grid by performing a boxcar average over a

width of 5 bins. We started by dividing the pointing area up into 10 bins, and found that in all pointings, the rms variation decreased significantly until reaching around 40-60 bins, where it leveled off. For all astrometric corrections we set the number of bins equal to 50 (corresponding to $\sim 35 - 50''$ per bin), as this provided the best balance between fidelity of reconstruction and noise.

As an example, the left panel of Figure 4.1 shows the astrometric corrections determined for pointing 31 in DEEP2 Field 3. Table 4.1 describes the improvement in astrometry for both CFHTLS-Wide and DEEP2 catalogs resulting from this process. We list the median and robust standard deviation of $RA_{SDSS} - RA$ and $dec_{SDSS} - dec$, both before and after corrections are applied. All standard deviations quoted in this table are derived using a robust estimator, which utilizes the median absolute deviation as an initial estimate and then weights points using Tukey's biweight (Hoaglin et al., 1983). In every case, there are large improvements in the agreement with SDSS astrometry; the standard deviation of the residuals is dominated by measurement errors, not systematics. This can be seen in the right panel of Figure 4.1 which shows a plot of the astrometric residuals for each calibration object in pointing 31, as well as histograms of their projected distributions in right ascension and declination, both before and after the correction. The improvement is much greater for DEEP2, but still detectable for the CFHTLS-Wide astrometry. We utilize the SDSS-reference-frame astrometry for both DEEP2 and CFHTLS in matching objects for the remainder of this chapter.

4.3 SUPPLEMENTAL PHOTOMETRIC INFORMATION FOR DEEP2

4.3.1 DEEP2 Field 1

In DEEP2 Field 1 we provide catalogs for DEEP2 pointings 11, 12, 13 and 14. The BRI photometry for pointings 11, 12, and 13 are taken directly from the DEEP2 catalogs described in §4.1. These measurements are identical to those provided in DEEP2 Data Release 4 (Newman et al., 2013b). The DEEP2 BRI photometry in pointing 14 had both inferior

(a)   (b)
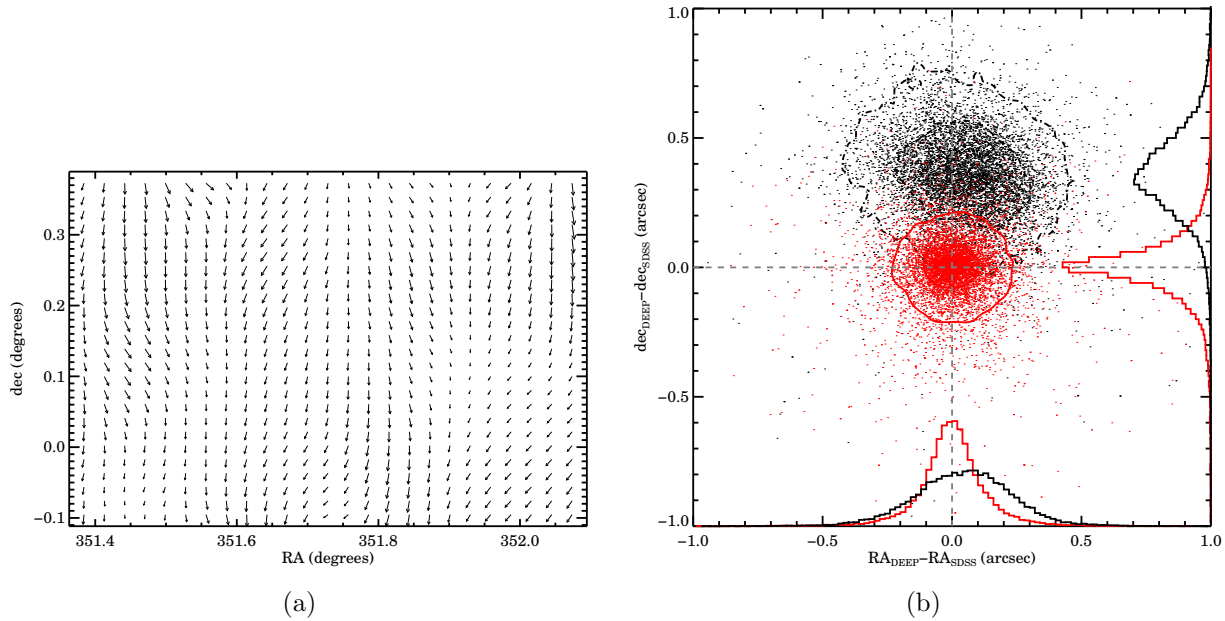
Figure 4.1 The left panel is an arrow plot showing the size and directions of the astrometric corrections applied in pointing 31, where a $0.03°$-long arrow indicates a $1''$ difference. Both the size and direction vary significantly over the field, making that depend on position on small scales necessary. The right panel shows the difference between the DEEP2 and SDSS astrometry for matches in the same pointing, both before (black) and after (red) the correction, where the contour lines correspond to 32% and 5% of the peak density, respectively. The projected distributions of each residual are shown on the bottom and right side of the plot, with all histograms normalized to have the same integral. The points show a random subset of all matches, while the contour lines and histograms were constructed using the full set of matches. There is a significant improvement in both the bias and spread after correction for both RA and declination; these differences are quantified for all pointings in Table 4.1.

depth and calibration quality to that obtained in other survey fields due to poor observing conditions when the data were taken. As a result, a purely R-selected sample was targeted in that region (Newman et al., 2013b). However, due to the wide range of multiwavelength data covering that area (Davis et al., 2007), the redshifts obtained there are quite valuable, and it is desirable to have as uniform a photometric sample as possible. We have therefore developed improved BRI photometry for the problematic region by using CFHTLS-Wide $ugriz$ photometry to predict DEEP2 BRI. We do this using transformations determined from data in DEEP2 pointings 11 and 12, as described below. We did not use pointing 13 because we found for the DEEP2 data the stellar locus in the color-color relation for that pointing to be not as well determined. In this catalog we also provide the $ugriz$ photometry for all DEEP2 sources that have a matching object (determined as described in §4.2) within either CFHTLS-Wide or Deep. More details of how the $ugriz$ photometry is assigned in described in §4.4.

4.3.1.1 Improved photometric zero point calibration for CFHTLS data The CFHTLS-Wide photometry overlapping DEEP2 Field 1 proved to have systematic zero point errors that varied amongst the individual MegaCam pointings. Hence, it was necessary to recalibrate each CFHTLS-Wide pointing overlapping with DEEP Field 1 in order to provide a uniform dataset. We found that the zero point errors in each band (assessed by comparison to SDSS) varied significantly from pointing to pointing. The typical offset for a pointing ranged in magnitude from $\sim 0.01 - 0.13$ with typical scatter within a pointing of $\sim 2 - 4 \times 10^{-2}$, except for in the u-band where the scatter was significantly larger (~ 0.2). These calculations are described in detail below. There are seven CFHTLS-Wide MegaCam pointings that overlap the four CFHT 12K pointings in DEEP Field 1: W3-1-2, W3-1-3, W3+0-1, W3+0-2, W3+0-3, W3+1-1, W3+1-2. We calibrated each pointing using objects identified as stars in SDSS DR9 data with $18 < r < 20$. For each of these stars we determined if there is a match in CFHTLS-Wide by searching for objects within the normal $0.75''$ search radius, finding an average of 737 matches per pointing. After finding matches in each catalog

we then calculated a linear fit to the magnitude difference between the two bands:

$$u_c - u_s = a_{0,u} + a_{1,u}(u_s - g_s) \tag{4.1}$$

$$g_c - g_s = a_{0,g} + a_{1,g}(g_s - r_s) \tag{4.2}$$

$$r_c - r_s = a_{0,r} + a_{1,r}(r_s - i_s) \tag{4.3}$$

$$i_c - i_s = a_{0,i} + a_{1,i}(i_s - z_s) \tag{4.4}$$

$$z_c - z_s = a_{0,z} + a_{1,z}(i_s - z_s) \tag{4.5}$$

where the "c" subscript denotes CFHTLS-Wide photometry, the "s" subscript denotes SDSS DR9 photometry, and a_0 and a_1 indicate the constant term and slope parameters from the fit. This regression, as well as all other fits were done using the IDL procedure POLY_ITER from the SDSS idlutils library, which is an iterative fitting procedure that uses outlier rejection. Adding quadratic color terms did not significantly improve the fits. Figure 4.2 plots the relations in equations 4.1-4.5 as well as the linear fits for pointing W3-1-3. For the u-band relation, we used only objects with $u_s < 22$ for the fit since u-band measurements in SDSS are extremely noisy fainter than this limit, as is evident in the first panel of Figure 4.2. On average this cut eliminated $\sim 57\%$ of the objects from the sample used for fitting. The values for a_0 and a_1 from the overall fits for each band are listed in Table 4.2. We estimated the uncertainties in these parameters by bootstrapping and found for a_0 the errors in the $griz$ bands are $\sim 2 - 6 \times 10^{-3}$ and $\sim 1 - 3 \times 10^{-2}$ in the u-band. For a_1 the uncertainties in the gri bands are $\sim 2 - 6 \times 10^{-3}$ and $\sim 10^{-2}$ and the u and z bands.

If both the CFHT and SDSS photometry were on the AB filter system in their native passbands, we would expect there to be no difference between the magnitudes measured in the two systems for an object with the AB defining spectrum ($F_\nu = 3.631 \times 10^{-20}$ erg s^{-1}Hz^{-1}cm^{-2}), which should have the same magnitude in all bands and hence zero color. Therefore, if a_0 is non-zero, u_c and u_s cannot both be on the AB system. Although SDSS magnitudes are not quite AB, they are very close (Fukugita et al., 1996; Stoughton et al., 2002), and hence we can use the a_0 values to determine how the zero points of the CFHTLS-Wide photometry must be changed to place them on a uniform AB system. In principle, we could perform this fit over small ranges in right ascension and declination to determine the spatial variation in
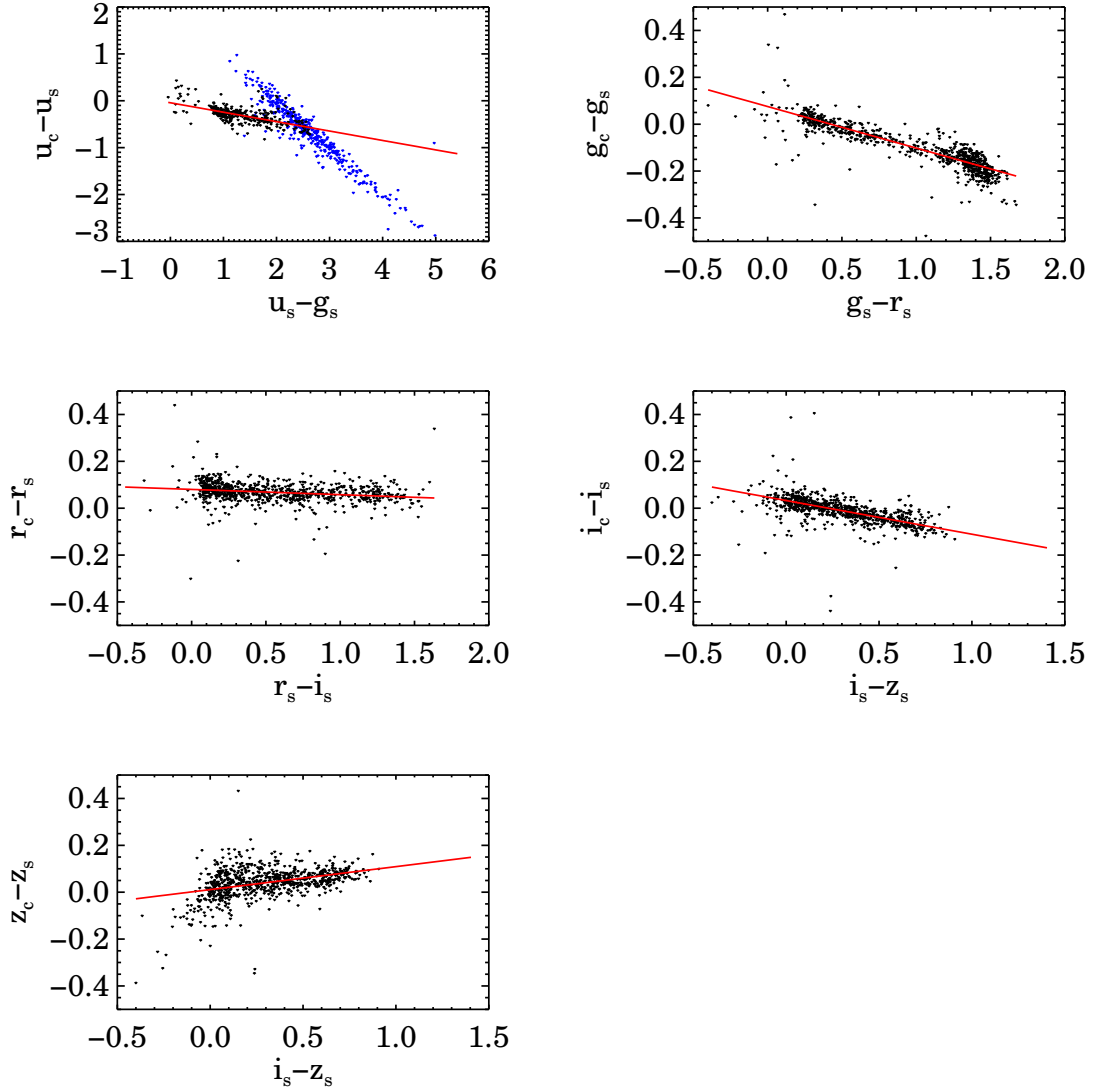
Figure 4.2 Plots of the difference between CFHTLS-Wide and SDSS magnitudes difference as a function of SDSS color term for each $ugriz$ band, utilizing objects identified as stars in SDSS with $18 < r < 20$ that overlap CFHTLS-Wide pointing W3-1-3. The red lines are the linear fits whose coefficients are listed in Table 4.2. In the top left plot we see that there are points that scatter along a second diagonal that does not follow the linear fit. This is due to the large u-band measurement errors for objects faint in u in SDSS. We performed a magnitude cut ($u_s < 22$) for objects used in the linear fit for this band so that the objects in the second diagonal would not influence the fit, as described in §4.3.1.1. Blue points are objects that were not used in the fit.

CFHTLS zero point errors; however, in practice SDSS stars are too sparse to measure a_1 robustly in small bins of position on the sky.

Instead, we adopt the strategy of using a fixed a_1 value for each pointing and determining variation only in a_0. We use a pointing's a_1 value for a given band (specified by the above relations) to calculate the quantities

$$\Delta_u = (u_c - u_s) - a_{1,u}(u_s - g_s) \tag{4.6}$$

$$\Delta_g = (g_c - g_s) - a_{1,g}(g_s - r_s) \tag{4.7}$$

$$\Delta_r = (r_c - r_s) - a_{1,r}(r_s - i_s) \tag{4.8}$$

$$\Delta_i = (i_c - i_s) - a_{1,i}(i_s - z_s) \tag{4.9}$$

$$\Delta_z = (z_c - z_s) - a_{1,z}(i_s - z_s) \tag{4.10}$$

for each object. By the same argument given above, if m_c and m_s are AB magnitudes, its offset Δ_m should be zero everywhere (modulo measurement errors). For all bands except the u-band, we construct a two dimensional map of Δ_m in RA and dec for each pointing. We expect Δ_m to vary slowly across the field, and so we determine the map by fitting a 2-D second order polynomial, i.e.

$$\Delta_m(\text{RA}, \text{dec}) = b_{0,m} + b_{1,m}(\text{RA}) + b_{2,m}(\text{RA})^2 + b_{3,m}(\text{RA})(\text{dec}) + b_{4,m}(\text{dec}) + b_{5,m}(\text{dec})^2. \tag{4.11}$$

The b coefficients are calculated separately for each CFHTLS-Wide pointing and for each passband ($g/r/i/z$). We can then obtain AB-calibrated CFHT photometry in a given band, m_c', by setting $m_c' = m_c - \Delta_m(\text{RA}, \text{dec})$. For the u-band, we obtained better results by calculating a mean Δ_u in each pointing to obtain $u_c' = u_c - \langle\Delta_u\rangle$, rather than fitting a 2-D polynomial over RA and dec. This was most likely due to noise in the u-band measurement affecting the fit. We have used the robust Hodges-Lehmann estimator of the mean to calculate $\langle\Delta_u\rangle$ in each pointing.

We also found it necessary to recalibrate the CFHTLS-Deep photometry in order for it to have consistent zero points with the refined CFHTLS-Wide photometry. We performed this calibration by applying the same techniques used for the Wide survey u-band data; i.e., we employ a constant zero point offset, $m_c' = m_c - \langle\Delta_m\rangle$. We adopt this method to make it

simple to transform back to the original CFHTLS-Deep photometry, facilitating the use of our catalog to calibrate photo-z's for all of the CFHTLS-Deep fields. We again used the robust Hodges-Lehmann estimator of the mean to calculate $\langle\Delta_m\rangle$. For each band the correction is $\langle\Delta_u\rangle$=-0.01941, $\langle\Delta_g\rangle$=0.07374, $\langle\Delta_r\rangle$= 0.03056, $\langle\Delta_i\rangle$=0.04441, and $\langle\Delta_z\rangle$=0.03282. The values for a_0 and a_1 (Equations 4.1-4.5) calculated for CFHTLS-Deep photometry are listed in Table 4.2.

These corrections have been applied to the CFHTLS-Wide and Deep $ugriz$ photometry for all objects in this catalog. Table 4.3 shows the improvement in the zero-point offset estimate for each pointing by showing the median and standard deviation of this offset amongst all SDSS reference stars before and after this calibration, and Figure 4.3 shows the distribution of these offsets for all $ugriz$ bands in pointing W3-1-3 both before and after the calibration. All standard deviations quoted in the table are calculated using the robust estimator described in §4.2. Median offsets become negligible after correction; zero point errors that in some cases approached 0.2 mag are $\lesssim$ 0.01 after correction. The standard deviation is dominated by random uncertainties, but still is reduced in all but one case, indicating that our spatially-varying zero point correction has improved the match between CFHTLS-Wide and SDSS photometry compared to a uniform offset.

The a_1 coefficients calculated from the linear fits in Equations 4.1-4.5 can also be used to transform between the CFHTLS and SDSS photometry systems. For example, due to how we have defined the zero point offset for our new calibrated CFHTLS photometry, the transformation for the u-band is defined as $u'_c = u_s + \langle a_{1,u}\rangle(u_s - g_s)$, where we have calculated $\langle a_{1,u}\rangle$ from the average $a_{1,u}$ values over all seven CFHTLS-Wide pointings and the single CFHTLS-Deep pointing. The color terms used in the transformations for all other bands can be determined from Equations 4.1-4.5, and the values of $\langle a_1\rangle$ for each band are listed in Table 4.2. This transformation can be applied to bring SDSS photometry into the same filter system as CFHTLS. In addition, solving for the SDSS magnitude in the above equation allows for the transformation of the CFHTLS photometry from this catalog into the same system as SDSS. Either transformation can bring the entire catalog into the same $ugriz$ system for photo-z tests.

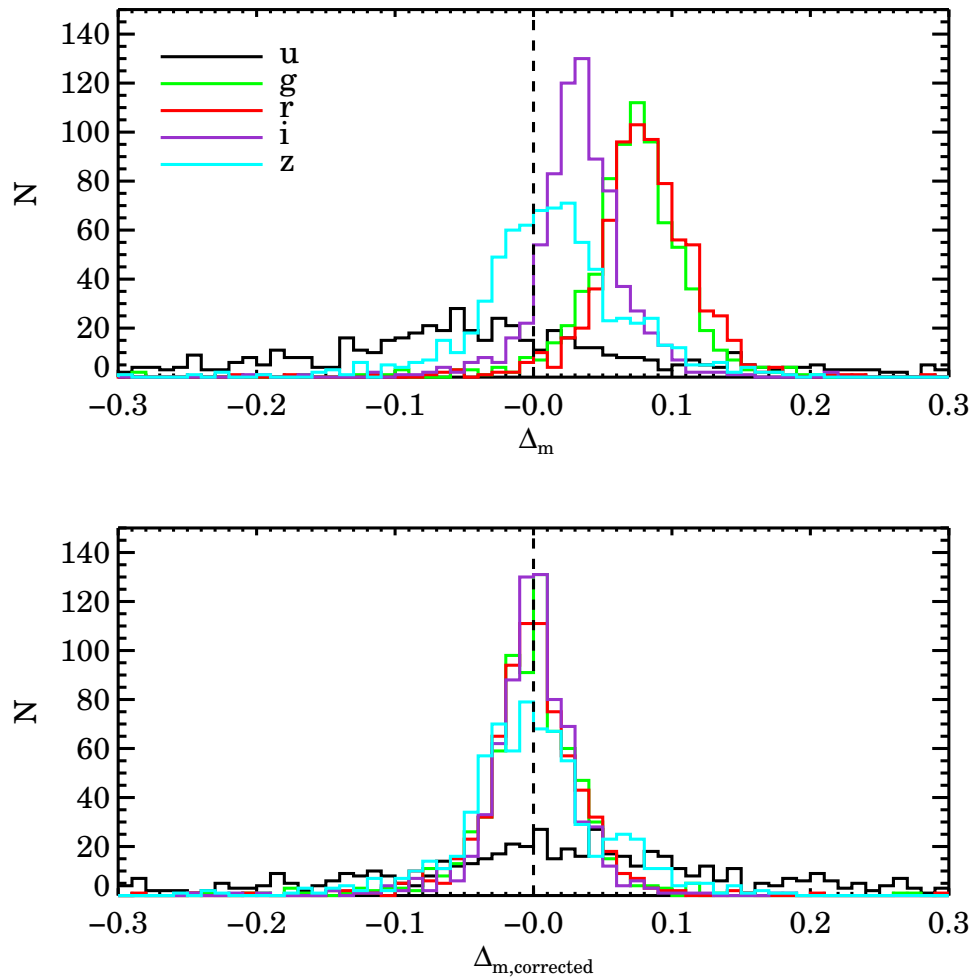Figure 4.3 The distributions of the zero-point offsets for the CFHTLS-Wide photometry in pointing W3-1-3 relative to SDSS DR9 (Δ_m in equations 4.6-4.10) for the bright stars $(18 < r < 20)$ in each band before and after the improved calibration. After the corrections to the $ugriz$ photometry, the systematic offsets in each band are removed. This improvement is shown quantitatively for all pointings in Table 4.3.

4.3.1.2 Predicting photometry of DEEP pointing 14 Due to the inferior photometry in DEEP2 pointing 14, we used the CFHTLS-Wide *ugriz* photometry for objects in pointings 11 and 12 to predict the *BRI* photometry in DEEP pointing 14. To determine the transformation between the two systems, we chose sources identified as stars in the DEEP2 catalog with $18.2 < R < 21$. This range was selected in order to obtain a sample of bright stars which are also above the saturation limit of the DEEP2 survey.

The *BRI* photometry in the DEEP2 catalogs have been corrected for Galactic dust extinction (Schlegel et al., 1998). However in the CFHTLS-Wide catalog, magnitudes have not been adjusted for this. Hence, before determining color transformations, we removed the extinction correction from the DEEP2 *BRI* photometry, using the same Schlegel et al. (1998) reddening estimates (SFD_EBV) and R values that were employed to make the original DEEP2 catalogs.

We matched these sources to CFHTLS-Wide objects again using a $0.75''$ search radius, and calculated the parameters of the relations

$$B - g = c_{0,B} + c_{1,B}(g - r) + c_{2,B}(g - r)^2 \tag{4.12}$$

$$R - r = c_{0,R} + c_{1,R}(r - i) + c_{2,R}(r - i)^2 \tag{4.13}$$

$$I - i = c_{0,I} + c_{1,I}(i - z) + c_{2,I}(i - z)^2. \tag{4.14}$$

Figure 4.4 plots the relations in equations 4.12-4.14 as well as the quadratic fit for pointings 11 and 12. We then use these parameters to calculate the predicted photometry for all objects in DEEP pointing 14, including sources identified as galaxies. By plotting the residuals of all objects as a function of r-band half light radius as determined in the CFHTLS-Wide catalog, we found there is a contribution from the source size. We represented this contribution with a linear fit to these residuals, which gives the final predicted photometry as

$$B = g + c_{0,B} + c_{1,B}(g - r) + c_{2,B}(g - r)^2 + d_{0,B} + d_{1,B}(\mathrm{R}_r) \tag{4.15}$$

$$R = r + c_{0,R} + c_{1,R}(r - i) + c_{2,R}(r - i)^2 + d_{0,R} + d_{1,R}(\mathrm{R}_r) \tag{4.16}$$

$$I = i + c_{0,I} + c_{1,I}(i - z) + c_{2,I}(i - z)^2 + d_{0,I} + d_{1,I}(\mathrm{R}_r) \tag{4.17}$$

where R_r is the r-band half light radius (designated as r_flux_radius in the catalog). Table 4.4 lists all of these coefficients for pointings 11-13 as well as the coefficients calculated from

combining pointings 11 and 12. Errors in this predicted photometry were calculated using simple propagation of errors using the errors in $g, r, i,$ and z from CFHTLS-Wide. In order to maintain consistency with DEEP2 photometry in other fields, we then apply a correction for extinction in the same manner as for the other DEEP2 magnitudes.

Figure 4.5 shows color-color plots for the bright stars in pointings 11 and 14 that were used to determine the $griz$ to BRI transformation described above, both before and after applying the transformation. We see that the stellar locus in pointing 11 is relatively unaffected by the transformation compared to pointing 14. We also see the improved calibration of the pointing 14 photometry in that the locus in 14 is tighter and more consistent with the locus in 11 after the transformation. We note that although we applied the transformation to obtain predicted BRI photometry in pointing 11 for this plot, in the final catalog the transformation is only applied to pointing 14.

4.3.2 DEEP2 Fields 2, 3 and 4

We are also providing catalogs with improved astrometry (cf. §4.2) and $ugriz$ photometry added for objects from DEEP2 Field 2 (pointings 21 & 22), Field 3 (pointings 31,32, & 33) and DEEP Field 4 (pointings 41, 42, & 43). In each case, the BRI photometry is taken directly from the DEEP2 catalogs described in §4.1, while the $ugriz$ photometry is determined from matching sources in SDSS, using the procedure described in §4.2. In Field 2 we use SDSS photometry from the DR9 data release. Since Fields 3 and 4 overlap with Stripe 82, we use the deeper photometry from the Stripe82 database (cf. §4.1).

4.4   DATA TABLES

Below we describe the columns that are included for each object in our new FITS BINTABLE[1] format files, as well as a brief description of each quantity. We have created one set of new catalogs that are parallel in content to each of the existing *pcat* photometric catalogs, as

---

[1]Part of the IDLUTILS package available at http://www.astro.princeton.edu/~schlegel/code.html.
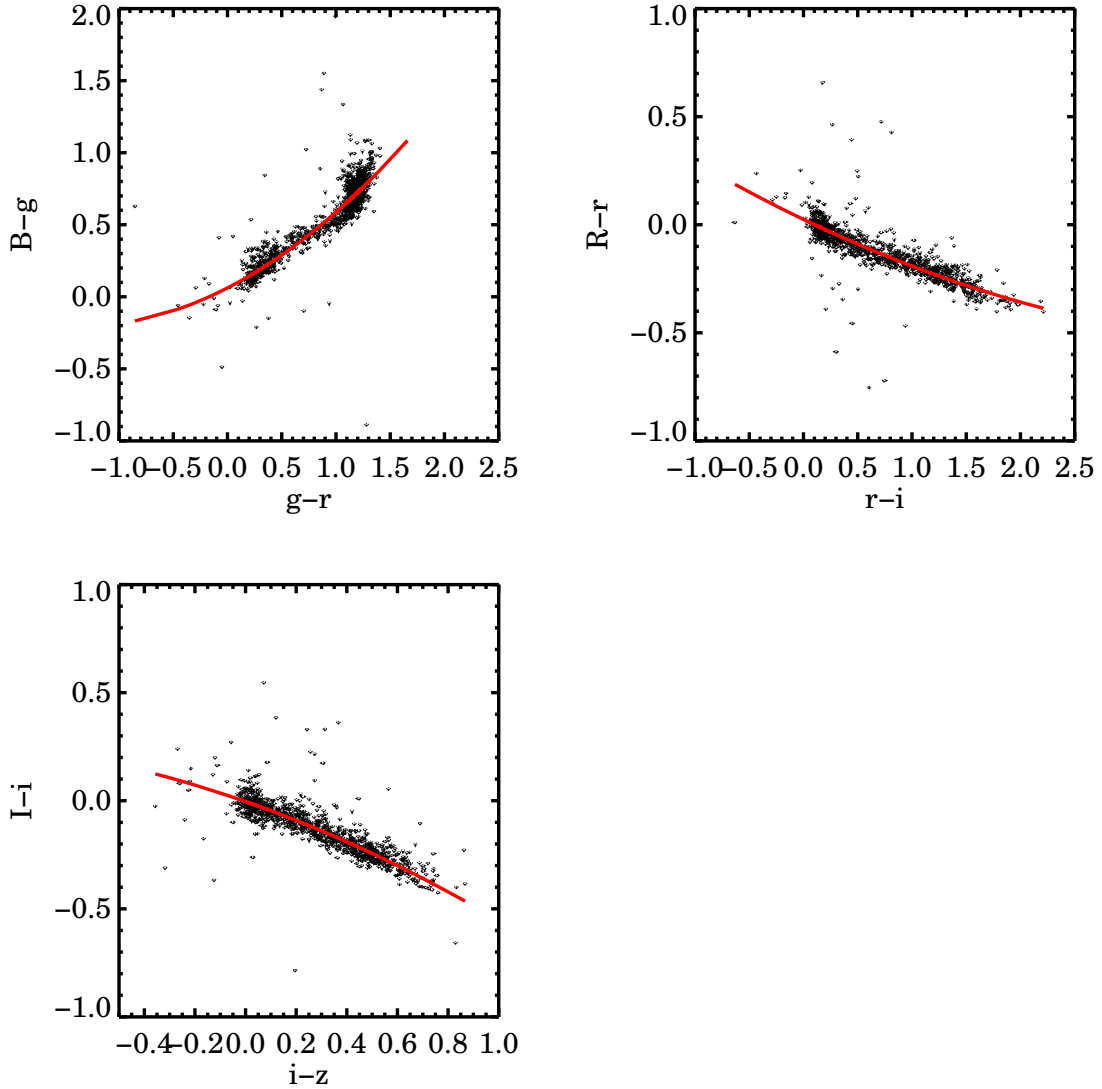
Figure 4.4 Plots of the difference between DEEP2 and CFHTLS-Wide magnitudes as a function of CFHTLS color for each BRI band, using objects identified as stars in DEEP2 pointings 11 and 12 with $18.2 < R < 21$. The red lines are the quadratic fits whose coefficients are listed in Table 4.4.
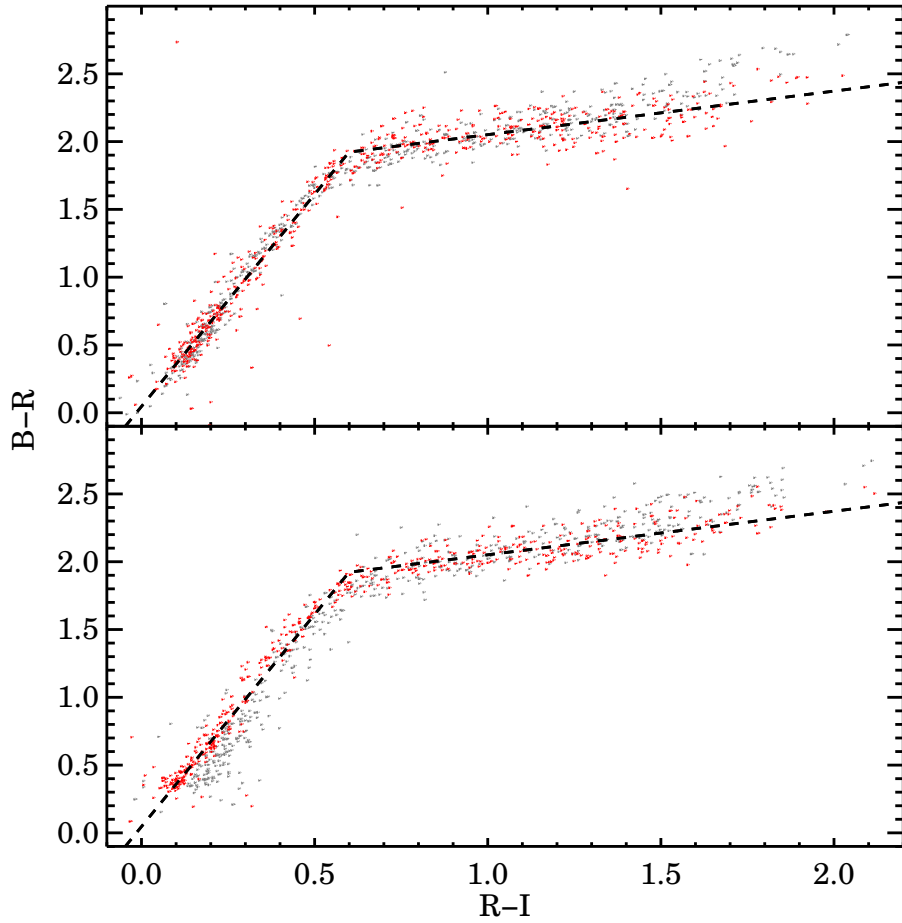
Figure 4.5 Color-color plots of the stars with $18.2 < R < 21$ that were used to determine the *ugriz* (CFHTLS-Wide) to *BRI* (DEEP2) transformation described in §4.3.1.2. The top panel shows the stellar locus for pointing 11 and the bottom for pointing 14, and the dashed lines are the same in each plot. The gray points are the colors straight from the public DEEP2 catalogs, and the red points are the colors after the transformation. The stellar locus in pointing 11 is relatively unaffected by the transformation compared to pointing 14. The improved calibration of the pointing 14 photometry is apparent in the greater consistency of the stellar locus for pointing 14 after the transformation to that from pointing 11 (most easily visible by comparing each to the dashed lines).

well as a single new catalog that parallels the *zcat* redshift catalog, and hence contains only objects for which DEEP2 obtained a spectrum. All of these columns appear in both catalogs. Further details of those columns that have been taken directly from other catalogs can be found in Newman et al. (2013b), Gwyn (2012), Abazajian et al. (2009), and Ahn et al. (2012). For each object, any column where data is not available is given a value of -99. The object properties included in the catalog are:

- OBJNO - a unique 8-digit object identification number, taken from the *pcat* photometric catalog. The first digit of OBJNO indicates the DEEP2 field an object is drawn from, and the second object indicates pointing number (e.g., objects in DEEP2 pointing 14 will have object numbers beginning with 14).

- RA_{DEEP}, dec_{DEEP} - Right ascension and declination in degrees from the DEEP2 catalogs, including the astrometric correction described in §4.2. These positions will therefore differ from those in the original *pcat* catalogs.

- RA_{SDSS}, dec_{SDSS} - Right ascension and declination in degrees from either CFHTLS-Wide (DEEP2 Field 1) or SDSS (DEEP2 Fields 2-4) for all *pcat* objects that have a match in either catalog. The CFHTLS-Wide astrometry in Field 1 has been corrected as described in §4.2.

- BESTB, BESTR, BESTI - For all pointings except for pointing 14 in Field 1, these are CFHT 12K *BRI* magnitudes taken directly from the DEEP2 *pcat* catalogs. Photometry in pointing 14 is predicted using the methods described in §4.3.1.2 for objects that have a match with CFHTLS-Wide. Objects without a match are assigned no *BRI* values in pointing 14.

- BESTBERR, BESTRERR, BESTIERR - errors in the *BRI* photometry taken directly from the DEEP2 catalogs for all pointings except for pointing 14 in Field 1. Those error estimates include sky noise only. Errors for pointing 14 were calculated using simple propagation of errors from the errors in CFHTLS-Wide photometry.

- U, G, R, I, Z - *ugriz* magnitudes taken either from CFHTLS-Wide (DEEP2 Field 1) or SDSS (DEEP2 Fields 2-4) for all *pcat* objects that have a match in either catalog. The CFHTLS photometry used was the Kron-like elliptical aperture magnitude designated as MAG_AUTO in the unified CFHTLS catalogs. In our new *zcat* catalog, if photometry is

available for an object in Field 1 from the CFHTLS-Deep survey, that is used; otherwise the magnitudes from the CFHTLS-Wide survey are used. In our new *pcat* catalogs, CFHTLS-Wide is used for all photometry. SDSS magnitudes in Fields 2-4 are the model magnitudes taken from either DR9 (Field 2) or the coadded Stripe 82 database (Fields 3 & 4).

- UERR, GERR, RERR, IERR, ZERR - errors in the *ugriz* magnitudes taken directly from either CFHTLS-Wide or Deep (for DEEP2 Field 1), or from SDSS (DEEP2 Fields 2-4), for all *pcat* objects that have a match in either catalog.

- PGAL - probability of the object being a galaxy based on the R-band image and BRI color. For the calculations in this chapter, any object with $p_{gal} < 0.2$ was treated as a star, following the standard in Newman et al. (2013b).

- RG - Gaussian radius of a circular 2-d Gaussian fit to the R-band image, in units of $0.207''$CFHT 12K pixels.

- BADFLAG - quantity describing the quality of the BRI photometry measurement. A badflag value of zero designates a measurement with no known systematic issues (e.g. saturation, overlapping with bleed trails, etc.) in any bands (http://deep.berkeley.edu/DR1/photo.primer.html).

- ZHELIO - heliocentric reference-frame redshift taken from the *zcat* catalogs.

- ZHELIO_ERR - error in the redshift measurement taken from the *zcat* catalogs.

- ZQUALITY - redshift quality code, Q, where $Q = 3$ or 4 indicates a reliable galaxy redshifts, and $Q = -1$ indicates a reliable star identification.

- SFD_EBV - Galactic reddening $E(B - V)$ from Schlegel et al. (1998). DEEP2 BRI photometry has been corrected for this amount of reddening.

- SOURCE - string describing the source of the photometry for each object, where the first catalog listed is the source of the BRI photometry and the second is the source of the *ugriz* photometry. For DEEP2 pointings 11-13 the the source tag is either DEEP-CFHTLSW or DEEP-CFHTLSD (Wide or Deep), and for pointing 14 it is just CFHTLSW since the BRI is predicted from CFHTLS-Wide. In DEEP2 Field 2 the source tag is DEEP-SDSS and for Fields 3 and 4 the source tag is DEEP-SDSS82, des-

ignating that the *ugriz* photometry comes from the deeper Stripe82 database. For all objects lacking a match in other catalogs the source tag is just DEEP.

Table 5 shows examples of the catalog data for nine objects in pointing 11; three objects with no matches between DEEP2 and CFHTLS, three objects with matches but no redshifts, and three objects with matches and redshifts.

4.5 CONCLUSION

In this chapter we have presented the details of improved photometric catalogs for the DEEP2 Galaxy Redshift Survey constructed by combining data from three different projects: DEEP2 itself, the CFHT Legacy Survey, and SDSS. To further this purpose, we have used positions from SDSS to improve the astrometry for both DEEP2 and CFHTLS-Wide catalogs, and photometry for SDSS stars to improve the magnitude zero points in the CFHTLS-Wide data.

We then employed data from CFHTLS and SDSS to assign *ugriz* photometry to DEEP2 objects by matching sky positions between each catalog. In DEEP2 Field 1 we matched to the CFHTLS-Wide or Deep, in Field 2 we matched to SDSS DR9, and in Fields 3 and 4 we used the deeper SDSS Stripe 82 database. For objects in DEEP2 pointing 14 that had a counterpart in CFHTLS-Wide, we replaced the poorer-than-standard BRI photometry with predicted values calculated using the transformations between the BRI and *ugriz* photometry measured in DEEP2 pointings 11 and 12.

In each of the four pointings of DEEP2 Field 1 there are an average of $\sim 40,000$ matches with CFHTLS. Figure 4.6 shows the relations between various photometric quantities for bright stars and galaxies ($18 < R < 21$) that have matches between DEEP2 and CFHTLS in pointing 11. For pointing 14 where we have predicted the BRI photometry from the CFHTLS photometry, the equivalent figure looks qualitatively similar with the exception of any plot that relates DEEP2 color (i.e. $B - R$ or $R - I$) to the CFHTLS colors used to calculate the transformations in equations 4.15-4.17. These relations look necessarily tighter since the BRI photometry was calculated using a fit to these color relations. The r vs R relation looks significantly tighter as well for similar reasons. The total number of objects
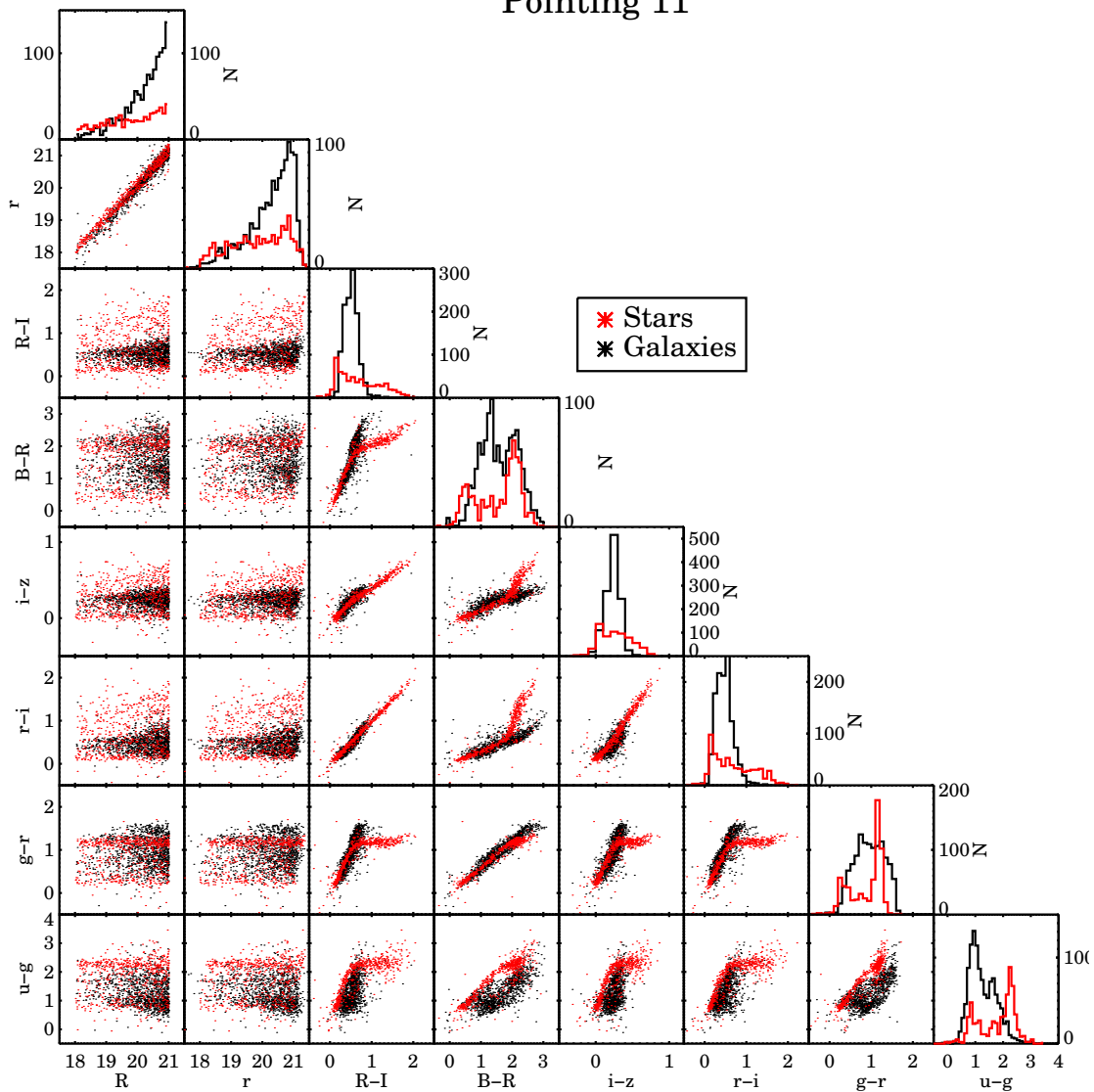
96

Figure 4.6 Plots of the relations between various photometric quantities for bright stars (red) and galaxies (black) with $18 < R < 21$ that have photometry in both DEEP2 pointing 11 and in CFHTLS-Wide. Histograms of each quantity are shown on the diagonal.

over all four pointings that have both $ugriz$ photometry and spectroscopic measurements is 16,584; 11,897 of those have high quality redshift measurements (zquality ≥ 3).

In the two pointings of DEEP2 Field 2 the average number of matches is only $\sim 7,700$ per CFHT 12K pointing, due to the shallowness of the SDSS DR9 dataset which overlaps the field. The total number of objects with both $ugriz$ photometry and redshifts in Field 2 is 968, with 751 having high quality redshifts. The three pointings of Field 3, where deeper Stripe 82 photometry is available, average $\sim 19,600$ matches between the *pcat* catalogs and SDSS. The total number of objects in Field 3 with $ugriz$ photometry and redshifts is 9691, with 6947 having high quality redshift measurements. Field 4 also overlaps SDSS Stripe 82; it includes three CFHT 12K pointings with an average of $\sim 22,200$ matches each, yielding 9445 objects with $ugriz$ photometry and redshifts, 6987 of which have secure redshifts.

For this catalog we have paired the spectroscopic redshift measurements from the DEEP2 Survey with the $ugriz$ photometry of CFHTLS an SDSS, making this catalog a valuable resource for the future as an excellent testbed for photo-z studies. These catalogs would be useful to future surveys such as LSST and DES for testing photo-z algorithms as well as the calibration of photo-z's. There are few public catalogs available with this number of objects with full $ugriz$ photometry as well as quality redshifts to this depth ($z \sim 1.4$). As a comparison, the zCOSMOS data release DR2 is one of the larger current datasets with these characteristics, and it contains $\sim 10,000$ objects with $ugriz$ photometry out to $z \sim 0.8$, $\sim$6000 of which have secure redshifts (Lilly et al., 2009). We caution readers that the SDSS and CFHTLS $ugriz$ passbands differ, so the combined redshift and photometric catalog presented here should not be treated as a uniform dataset; however, the SOURCE column can be used to divide into separate catalogs with consistent photometric passbands, which can be used separately to test photometric redshift methods. Alternatively, the CFHTLS or SDSS photometry can be transformed as described in §4.3.1.1, bringing the entire catalog into the same $ugriz$ system.

The extended DEEP2 catalogs described in this paper are publicly available and can be downloaded at http://deep.ps.uci.edu/DR4/photo.extended.html.

Pointing	$\text{RA}_{\text{SDSS}} - \text{RA}_{\text{DEEP}}$ ($''$)		$\text{dec}_{\text{SDSS}} - \text{dec}_{\text{DEEP}}$ ($''$)	
	median	σ	median	σ
11	-6.20×10^{-1}	3.01×10^{-1}	-6.51×10^{-2}	1.89×10^{-1}
	-8.17×10^{-4}	1.83×10^{-1}	-6.68×10^{-3}	1.07×10^{-1}
12	-6.42×10^{-1}	3.24×10^{-1}	-2.46×10^{-1}	2.44×10^{-1}
	-3.77×10^{-3}	1.95×10^{-1}	-3.47×10^{-3}	1.14×10^{-1}
13	-7.04×10^{-1}	3.55×10^{-1}	-4.02×10^{-1}	1.80×10^{-1}
	-5.41×10^{-3}	1.75×10^{-1}	-5.19×10^{-3}	1.02×10^{-1}
14	-4.32×10^{-1}	3.43×10^{-1}	-2.70×10^{-1}	1.88×10^{-1}
	-1.86×10^{-3}	1.87×10^{-1}	-2.60×10^{-3}	1.03×10^{-1}
21	-3.18×10^{-1}	1.39×10^{-1}	-1.97×10^{-1}	9.75×10^{-2}
	3.27×10^{-5}	9.38×10^{-2}	-1.08×10^{-3}	7.67×10^{-2}
22	-2.65×10^{-1}	1.20×10^{-1}	-1.82×10^{-1}	9.73×10^{-2}
	-2.84×10^{-3}	9.04×10^{-2}	-2.01×10^{-4}	7.29×10^{-2}
31	-4.61×10^{-2}	1.86×10^{-1}	-3.54×10^{-1}	1.58×10^{-1}
	-1.08×10^{-4}	1.15×10^{-1}	-5.98×10^{-4}	1.03×10^{-1}
32	-8.83×10^{-2}	2.14×10^{-1}	-3.14×10^{-1}	1.86×10^{-1}
	1.30×10^{-3}	1.16×10^{-1}	-9.10×10^{-4}	1.07×10^{-1}
33	8.48×10^{-2}	1.87×10^{-1}	-5.67×10^{-1}	1.53×10^{-1}
	-5.99×10^{-4}	1.13×10^{-1}	-4.95×10^{-4}	9.71×10^{-2}
41	1.27×10^{-1}	1.71×10^{-1}	-3.37×10^{-1}	1.79×10^{-1}
	5.24×10^{-4}	1.07×10^{-1}	-4.70×10^{-4}	1.02×10^{-1}
42	1.02×10^{-1}	1.70×10^{-1}	-2.92×10^{-1}	1.66×10^{-1}
	-3.72×10^{-4}	1.09×10^{-1}	-3.69×10^{-5}	1.02×10^{-1}
43	3.15×10^{-2}	1.64×10^{-1}	-3.34×10^{-1}	1.72×10^{-1}
	1.21×10^{-3}	1.07×10^{-1}	-6.59×10^{-4}	1.04×10^{-1}
Pointing	$\text{RA}_{\text{SDSS}} - \text{RA}_{\text{CFHT}}$ ($''$)		$\text{dec}_{\text{SDSS}} - \text{dec}_{\text{CFHT}}$ ($''$)	
	median	σ	median	σ
11	1.04×10^{-3}	2.10×10^{-1}	1.42×10^{-3}	1.30×10^{-1}
	3.40×10^{-4}	1.99×10^{-1}	-4.17×10^{-3}	1.16×10^{-1}
12	-5.57×10^{-2}	2.06×10^{-1}	-2.65×10^{-2}	1.25×10^{-1}
	4.83×10^{-4}	1.95×10^{-1}	-3.03×10^{-3}	1.16×10^{-1}
13	-2.52×10^{-2}	2.13×10^{-1}	-1.11×10^{-2}	1.20×10^{-1}
	5.21×10^{-4}	1.88×10^{-1}	2.68×10^{-3}	1.12×10^{-1}
14	3.69×10^{-2}	2.04×10^{-1}	-1.12×10^{-2}	1.17×10^{-1}
	-1.57×10^{-3}	1.78×10^{-1}	1.05×10^{-3}	1.03×10^{-1}

Table 4.1 This table lists the median and RMS variation in $\text{RA}_{\text{SDSS}} - \text{RA}$ and $\text{dec}_{\text{SDSS}} - \text{dec}$ for both CFHTLS-Wide and DEEP2, both before (regular text) and after (*italics*) the astrometric correction described in §4.2. The RMS was calculated using a robust estimator of the standard deviation described in §4.3.1.1. There is significant improvement in both quantities for all pointings.

Pointing	u band		g band		r band		i band		z band	
	a_0	a_1	a_0	a_1	a_0	a_1	a_0	a_1	a_0	a_1
W3–1–2	0.0195	-0.2309	0.0797	-0.1691	0.0380	-0.0106	0.0627	-0.1538	0.0507	0.0427
W3–1–3	-0.0394	-0.2043	0.0753	-0.1770	0.0791	-0.0210	0.0326	-0.1452	0.0111	0.0985
W3+0–1	-0.0024	-0.2010	0.1247	-0.1877	0.1171	-0.0379	0.0451	-0.1422	0.0522	0.0630
W3+0–2	-0.0152	-0.2334	0.0594	-0.1673	0.0891	-0.0221	0.0421	-0.1480	0.0491	0.0619
W3+0–3	-0.0116	-0.2320	0.0777	-0.1687	0.0516	-0.0107	0.0467	-0.1611	0.0356	0.0832
W3+1–1	0.0830	-0.2149	0.0889	-0.1820	0.0752	-0.0193	0.0378	-0.1394	0.0925	0.0677
W3+1–2	0.0673	-0.2198	0.0666	-0.1756	0.0613	-0.0276	0.0390	-0.1494	0.0493	0.0730
D3	-0.0127	-0.2247	0.0739	-0.1695	0.0325	-0.0194	0.0470	-0.1495	0.0320	0.0893
$\langle a_1 \rangle$		-0.2201		-0.1746		-0.0211		-0.1486		0.0724

Table 4.2 Coefficients describing the linear relation between the magnitude difference in CFHTLS and SDSS (i.e. $m_c - m_s$) and the relevant SDSS color term for each CFHTLS-Wide pointing overlapping DEEP2, as well as for the CFHTLS-Deep pointing in that region. These were used in the CFHTLS photometric calibrations described in §4.3.1.1. The average value of a_1 is also listed for each band, which can be used to transform between the CFHTLS and SDSS photometric systems as described in §4.3.1.1.

Pointing	u zero point offset		g zero point offset		r zero point offset		i zero point offset		z zero point offset	
	median	σ	median	σ	median	σ	median	σ	median	σ
W3-1-2	1.31×10^{-2}	2.90×10^{-1}	7.97×10^{-2}	3.34×10^{-2}	3.83×10^{-2}	2.90×10^{-2}	6.31×10^{-2}	3.05×10^{-2}	4.99×10^{-2}	4.09×10^{-2}
	1.33×10^{-2}	*2.90×10^{-1}*	*1.98×10^{-3}*	*3.25×10^{-2}*	*-4.89×10^{-4}*	*2.82×10^{-2}*	*2.21×10^{-4}*	*3.01×10^{-2}*	*-1.51×10^{-6}*	*4.05×10^{-2}*
W3-1-3	-5.55×10^{-2}	2.73×10^{-1}	7.47×10^{-2}	3.20×10^{-2}	8.01×10^{-2}	3.24×10^{-2}	3.30×10^{-2}	2.77×10^{-2}	1.26×10^{-2}	4.90×10^{-2}
	8.42×10^{-3}	*2.73×10^{-1}*	*9.25×10^{-4}*	*3.13×10^{-2}*	*-7.68×10^{-4}*	*3.09×10^{-2}*	*5.73×10^{-5}*	*2.65×10^{-2}*	*-1.37×10^{-3}*	*4.81×10^{-2}*
W3+0-1	-1.08×10^{-2}	2.65×10^{-1}	1.26×10^{-1}	3.07×10^{-2}	1.16×10^{-1}	3.17×10^{-2}	4.54×10^{-2}	2.73×10^{-2}	5.33×10^{-2}	3.97×10^{-2}
	6.03×10^{-3}	*2.65×10^{-1}*	*-1.21×10^{-3}*	*3.06×10^{-2}*	*-1.04×10^{-3}*	*3.12×10^{-2}*	*-2.60×10^{-3}*	*2.57×10^{-2}*	*-1.64×10^{-3}*	*3.94×10^{-2}*
W3+0-2	-7.93×10^{-3}	2.70×10^{-1}	6.00×10^{-2}	3.20×10^{-2}	8.92×10^{-2}	2.73×10^{-2}	4.17×10^{-2}	2.44×10^{-2}	4.97×10^{-2}	4.14×10^{-2}
	-2.67×10^{-3}	*2.70×10^{-1}*	*-5.26×10^{-4}*	*3.09×10^{-2}*	*-6.18×10^{-4}*	*2.65×10^{-2}*	*6.71×10^{-5}*	*2.33×10^{-2}*	*9.10×10^{-4}*	*4.05×10^{-2}*
W3+0-3	-2.10×10^{-2}	3.12×10^{-1}	7.70×10^{-2}	3.19×10^{-2}	5.13×10^{-2}	2.95×10^{-2}	4.74×10^{-2}	2.76×10^{-2}	3.58×10^{-2}	4.98×10^{-2}
	1.90×10^{-2}	*3.12×10^{-1}*	*1.02×10^{-3}*	*3.19×10^{-2}*	*1.64×10^{-4}*	*2.92×10^{-2}*	*-7.70×10^{-4}*	*2.76×10^{-2}*	*-7.94×10^{-4}*	*4.87×10^{-2}*
W3+1-1	7.38×10^{-2}	2.49×10^{-1}	8.85×10^{-2}	3.09×10^{-2}	7.55×10^{-2}	3.18×10^{-2}	3.70×10^{-2}	2.87×10^{-2}	9.31×10^{-2}	4.80×10^{-2}
	5.45×10^{-3}	*2.49×10^{-1}*	*4.56×10^{-4}*	*2.98×10^{-2}*	*5.47×10^{-4}*	*2.99×10^{-2}*	*-4.00×10^{-5}*	*2.84×10^{-2}*	*-1.91×10^{-3}*	*4.60×10^{-2}*
W3+1-2	5.27×10^{-2}	2.67×10^{-1}	6.54×10^{-2}	3.06×10^{-2}	6.14×10^{-2}	2.63×10^{-2}	3.82×10^{-2}	2.49×10^{-2}	5.08×10^{-2}	4.02×10^{-2}
	8.09×10^{-3}	*2.67×10^{-1}*	*3.69×10^{-5}*	*2.99×10^{-2}*	*7.76×10^{-4}*	*2.57×10^{-2}*	*2.09×10^{-4}*	*2.45×10^{-2}*	*-4.76×10^{-4}*	*3.92×10^{-2}*
D3	-1.77×10^{-2}	2.57×10^{-1}	7.43×10^{-2}	3.16×10^{-2}	3.13×10^{-2}	2.60×10^{-2}	4.60×10^{-2}	2.62×10^{-2}	3.23×10^{-2}	4.29×10^{-2}
	4.66×10^{-3}	*2.57×10^{-1}*	*7.02×10^{-4}*	*3.16×10^{-2}*	*8.28×10^{-4}*	*2.60×10^{-2}*	*1.39×10^{-3}*	*2.62×10^{-2}*	*6.27×10^{-4}*	*4.29×10^{-2}*

Table 4.3 This table lists the median and RMS of the zero point offset relative to SDSS before (regular text) and after (*italics*) the calibration of the CFHTLS-Wide and Deep photometry. The RMS was calculated using a robust estimator of the standard deviation, as described in §4.3.1.1. There is significant improvement in the median offset, such that it is much more consistent from pointing to pointing. The decrease in the RMS is small for all pointings, as photometric errors for each individual object dominate over the systematic variation, but in essentially every case there is a detectable improvement from allowing the zero point correction to vary across the pointing (save for the u band in Wide and all bands in Deep, where the corrections did not improve the RMS and hence have not been applied).

Pointing	B band					R band					I band				
	c_0	c_1	c_2	d_0	d_1	c_0	c_1	c_2	d_0	d_1	c_0	c_1	c_2	d_0	d_1
11	0.0507	0.4491	0.0895	-0.0475	0.0149	0.0248	-0.2358	0.0168	-0.0185	0.0058	-0.0069	-0.3915	-0.1944	-0.0026	0.0004
12	0.0987	0.2490	0.2290	-0.0717	0.0216	0.0159	-0.2211	0.0166	-0.0359	0.0111	-0.0068	-0.3714	-0.1796	0.0240	-0.0085
13	0.0366	0.5490	0.0073	-0.0807	0.0221	0.0299	-0.2557	0.0218	-0.0467	0.0156	-0.0038	-0.4006	-0.1404	0.0297	-0.0104
11 & 12	0.0640	0.3843	0.1396	-0.0639	0.0187	0.0239	-0.2404	0.0246	-0.0305	0.0094	-0.0040	-0.4083	-0.1461	0.0144	-0.0051

Table 4.4 Coefficients describing the transformation between CFHTLS-Wide $ugriz$ photometry and the DEEP2 BRI system. The c coefficients describe the quadratic fit for the color terms and the d coefficients describe the linear fit of the object size-based correction, as described in §4.3.1.2. The predicted BRI photometry of pointing 14 was determined using the coefficients from the combination of objects in pointings 11 and 12.

OBJNO	RA$_{DEEP}$ deg	dec$_{DEEP}$ deg	RA$_{SDSS}$ deg	dec$_{SDSS}$ deg	bestB	bestR	bestI	bestBerr	bestRerr	bestIerr	u	g	r	i	z
11100002	214.33959	51.94544	-99.0	-99.0	24.8987	24.4452	24.2239	0.1611	0.1027	0.1935	-99.0	-99.0	-99.0	-99.0	-99.0
11100003	214.35176	51.94724	-99.0	-99.0	24.9979	23.7502	23.5821	0.2009	0.0616	0.1219	-99.0	-99.0	-99.0	-99.0	-99.0
11100004	214.35030	51.94721	-99.0	-99.0	25.5034	24.0699	23.6283	0.2600	0.0738	0.1034	-99.0	-99.0	-99.0	-99.0	-99.0
11100000	214.36946	51.93833	214.36940	51.93835	25.2153	24.2380	23.6656	0.2787	0.1072	0.1404	24.7350	24.8243	24.8666	23.8106	25.0071
11100001	214.36935	51.93876	214.36935	51.93877	25.0578	24.5357	23.6953	0.1543	0.0903	0.0923	24.6641	24.4204	24.5461	23.3952	22.9106
11100008	214.27251	51.94721	214.27249	51.94729	24.5448	23.6794	22.9495	0.1433	0.0612	0.0722	25.1644	24.6349	24.3530	23.6916	23.2536
11100372	213.94919	52.07017	213.94912	52.07027	23.7849	23.5871	22.9274	0.0602	0.0573	0.0620	23.8947	23.2900	23.2600	22.7221	22.7198
11100402	213.64241	52.05337	213.64242	52.05340	24.3111	23.4869	23.0316	0.0737	0.0414	0.0547	25.0905	24.3498	23.9791	23.2209	23.1748
11100403	213.64160	52.05348	213.64157	52.05349	24.1674	23.4253	22.6158	0.0606	0.0368	0.0350	24.6405	24.0919	23.7302	22.9127	22.4641

uerr	gerr	rerr	ierr	zerr	pgal	rg	zhelio	z_err	zquality	SFD_EBV	Source
-99.0	-99.0	-99.0	-99.0	-99.0	3.00	2.59472	-99.0	-99.0	-99	0.00854562	DEEP
-99.0	-99.0	-99.0	-99.0	-99.0	3.00	2.95285	-99.0	-99.0	-99	0.00851513	DEEP
-99.0	-99.0	-99.0	-99.0	-99.0	3.00	2.39937	-99.0	-99.0	-99	0.00851823	DEEP
0.1844	0.1591	0.2015	0.2003	0.6875	3.00	2.98541	-99.0	-99.0	-99	0.00852105	DEEP-CFHTLSW
0.2191	0.1392	0.1903	0.1733	0.1265	1.00	1.91101	-99.0	-99.0	-99	0.00851886	DEEP-CFHTLSW
0.1538	0.0756	0.0710	0.1015	0.0772	3.00	3.13192	-99.0	-99.0	-99	0.00868888	DEEP-CFHTLSW
0.1357	0.0634	0.0749	0.1201	0.1356	3.00	2.95285	1.18247	6.40144e-05	4	0.0134441	DEEP-CFHTLSW
0.4416	0.0996	0.1601	0.0926	0.2277	3.00	2.38310	0.775875	4.99088e-05	4	0.0150038	DEEP-CFHTLSW
0.2792	0.0751	0.1218	0.0667	0.1132	3.00	2.23659	0.852072	4.44253e-05	4	0.0150446	DEEP-CFHTLSW

Table 4.5 Examples of the catalog data for nine different objects in pointing 11: three with matches and no redshifts, and three with matches and redshifts. Full data tables are provided at http://deep.ps.uci.edu/DR4/photo.extended.html.

5.0   CONCLUSION

Over the next decade and beyond there will be a variety of large cosmological surveys that will be used to gain insight into the structure and history of our Universe, and in doing so better understand the nature of dark energy. Many of these surveys will be obtaining data for an extremely large number of objects on the sky via wide-area imaging with unprecedented sky coverage. One of the key challenges of these surveys is to determine the ever-important redshift information for such an enormous number of objects, in some cases billions of objects. Current methods of obtaining accurate redshifts such as using spectroscopy are just not feasible for such enormous datasets, and alternatives must be explored.

Measuring galaxy redshifts using broadband imaging through only a few filters, i.e. photometric redshifts, is a promising avenue of study, although there are inherent limitations to this method as it relies on determining the location in wavelength of broad spectral features rather than narrow absorption or emission lines. This, among other things, makes them less understood than spectroscopic redshifts. Photometric redshifts are generally calculated using various photo-z algorithms, and understanding how these algorithms assign redshifts, as well as understanding the underlying true redshift distribution of the objects will be very important for future dark energy surveys.

This thesis presented a test of the cross-correlation technique for calibrating photometric redshifts which uses the measured spatial clustering on the sky of a photometric sample with a spectroscopic sample that has secure and accurate redshifts, as a function of redshift. These results have shown that the cross-correlation technique can be used to accurately reconstruct the true redshift distribution of a photometric sample that only has imaging information for each object. This technique can be used to measure the true redshift distribution of a large number of galaxies, enabling significant improvement in cosmological parameter measure-

ments. It also included a discussion of the contribution of weak gravitational lensing to the cross-correlation signal and how its effects can be mitigated. In addition, it has shown how similar clustering measurements can be used to constrain the low-z interloper fraction in high redshift candidate samples. And finally it described a new catalog that combines spectroscopic redshifts and deep photometry to be used as a testbed for future photo-z studies.

Combining information from both spectroscopic and photometric surveys will be a very powerful tool for future cosmological experiments, and there is already considerable work being done to test and refine the cross-correlation technique, including tests on real data (Schmidt et al., 2013; McQuinn & White, 2013; Ménard et al., 2013; de Putter et al., 2013). In addition to tests with data from observation, another possibility will be to test these techniques using larger, more realistic simulations, as this will more closely mimic the real datasets of future experiments. The cross-correlation technique for constraining the inter-loper fraction may also be applied to new surveys of the high-redshift universe such as the CANDELS Multi-Cycle Treasury Program on the Hubble Space Telescope (Grogin et al., 2011). Systematic uncertainties in the photometric redshift estimates for galaxies are expected to be a dominant source of error for many future cosmological measurements, and characterizing these uncertainties will be extremely important moving forward in our study of the Universe.

APPENDIX A

CROSS-CORRELATION DERIVATION

For the derivation of equation 2.3 we begin with the integral relating the angular cross-correlation of a narrow spectroscopic z-bin with the photometric sample, $w_{sp}(\theta, z)$, to the real-space cross-correlation, $\xi_{sp}(r(z, z'), z)$, and the redshift distribution of the photometric sample, $\phi_p(z')$. The quantity $w_{sp}(\theta, z)$ is a measure of the excess probability (above random) of finding a galaxy at a separation θ on the sky from another galaxy, and $\xi_{sp}(r(z, z'), z)$ is the analogous quantity except for real-space separations, $r(z, z')$. These are described in more detail in section 2.1.2. In the following, z is the redshift of the spectroscopic objects and z' is the redshift of a photometric object. To determine the angular cross-correlation between the two samples we convolve the real-space cross-correlation with the redshift distribution of the photometric sample and integrate over all possible redshifts of photometric objects, z', to obtain

$$w_{sp}(\theta, z) = \int_0^\infty \xi_{sp}(r(z, z'), z)\phi_p(z')dz'. \tag{A.1}$$

We assume a power law for the real-space cross-correlation, i.e. $\xi_{sp} = (r/r_0)^{-\gamma}$ with $r = (r_p^2 + \pi^2)^{1/2}$, where r_p and π are the line-of-sight and transverse separation between two objects as defined in equations 2.5 and 2.6. Since we are cross-correlating a narrow spectroscopic bin with the photometric sample we make the assumption that $\phi_p(z')$ does not change significantly over this range and can pull it out in front of the integral. To simplify the integral we perform a change of variable to write it in terms of the line-of-sight separation

using equation 2.6 to relate π to z'. Substituting $r_p = D(z)\theta$ (equation 2.5) we obtain

$$w_{sp}(\theta, z) = \phi_p(z) \int_{-\infty}^{+\infty} \left(\frac{((D(z)\theta)^2 + \pi^2)^{1/2}}{r_{0,sp}} \right)^{-\gamma_{sp}} \frac{1}{dl/dz} d\pi, \tag{A.2}$$

where $r_{0,sp}$ and γ_{sp} are the power law parameters for the cross-correlation, $D(z)$ is the angular size distance and $l(z)$ is the comoving distance to redshift z. The quantity dl/dz will also not vary significantly over the range which the cross-correlation is non-negligible so it can be pulled out in front of the integral as well. Evaluating this integral gives

$$
\begin{aligned}
w_{sp}(\theta, z) &= \frac{\phi_p(z)r_{0,sp}^{\gamma_{sp}}}{dl/dz} \int_{-\infty}^{+\infty} \left((D(z)\theta)^2 + \pi^2 \right)^{-\frac{\gamma_{sp}}{2}} d\pi \tag{A.3} \\
&= \frac{\phi_p(z)r_{0,sp}^{\gamma_{sp}}H(\gamma_{sp})D(z)^{1-\gamma_{sp}}\theta^{1-\gamma_{sp}}}{dl/dz}, \tag{A.4}
\end{aligned}
$$

where $H(\gamma) = \Gamma(1/2)\Gamma((\gamma - 1)/2)/\Gamma(\gamma/2)$ and $\Gamma(x)$ is the standard Gamma function. This gives the result shown in equation 2.3 relating the angular cross-correlation to the redshift distribution of the photometric sample.

APPENDIX B

POWERFIT CODE

In the course of the analysis described in chapter 2 I developed a short IDL function designed to fit for the parameters of a power-law plus constant model using full covariance information, with or without conditioning of the covariance matrix. Given arrays containing the independent variable values x, the dependent variable values y, and the covariance matrix of the y values, $\mathbf{C}$, it determines the best-fit parameters for a function of the form $y = ax^b + c$ via χ^2 minimization (cf. Equation 2.14). It outputs the best-fit parameter values in the form of a three-element array, i.e. $[a, b, c]$. POWERFIT calculates the fit parameters as described in §2.2.1. If the exponent, b, is fixed, the best-fit values of a and c are calculated analytically using standard linear regression formulae. To fit for all three parameters simultaneously, POWERFIT instead uses the AMOEBA function (distributed with IDL, and based on the routine amoeba described in Numerical Recipes in C (Press et al., 1992)) to search for the exponent value that minimizes the χ^2 of the fit.

POWERFIT optionally allows the user to fix either the exponent value, b, the constant, c, or both, at specified values when calculating the fit. It is also possible to condition the covariance matrix using either of the methods described in §2.2.2. For ridge regression conditioning, the user must provide a value for f, the fraction of the median of the diagonal elements of the covariance matrix to add to the diagonal elements before inverting. For SVD conditioning, the required input is the singular value threshold; any singular values below that threshold, as well as their inverses, are set equal to zero before calculating the inversion. The code is suitable for any application where a power law or power law plus

constant model is fit to data with a known covariance matrix; it can be downloaded at
http://www.phyast.pitt.edu/~janewman/powerfit.

BIBLIOGRAPHY

Abazajian, K. N., et al. 2009, ApJS, 182, 543

Ahn, C. P., et al. 2012, ApJS, 203, 21

Albrecht, A., et al. 2006, ArXiv Astrophysics e-prints

—. 2009, ArXiv e-prints

Bartelmann, M., & Schneider, P. 2001, Phys. Rep., 340, 291

Beaulieu, J. P., et al. 2010, in Astronomical Society of the Pacific Conference Series, Vol. 430, Pathways Towards Habitable Planets, ed. V. Coudé du Foresto, D. M. Gelino, & I. Ribas, 266

Benjamin, J., van Waerbeke, L., Ménard, B., & Kilbinger, M. 2010, MNRAS, 408, 1168

Bernstein, G., & Huterer, D. 2010, MNRAS, 401, 1399

Bernstein, G. M. 1994, ApJ, 424, 569

Bouwens, R. J., Illingworth, G. D., Blakeslee, J. P., & Franx, M. 2006, ApJ, 653, 53

Bouwens, R. J., Illingworth, G. D., Franx, M., & Ford, H. 2007, ApJ, 670, 928

—. 2008, ApJ, 686, 230

Bouwens, R. J., et al. 2012, ApJ, 754, 83

Broadhurst, T. J., Taylor, A. N., & Peacock, J. A. 1995, ApJ, 438, 49

Bunker, A. J., et al. 2010, MNRAS, 409, 855

Coil, A. L., Newman, J. A., Kaiser, N., Davis, M., Ma, C.-P., Kocevski, D. D., & Koo, D. C. 2004, ApJ, 617, 765

Coil, A. L., et al. 2008, ApJ, 672, 153

—. 2011, ApJ, 741, 8

Connolly, A. J., Csabai, I., Szalay, A. S., Koo, D. C., Kron, R. G., & Munn, J. A. 1995, AJ, 110, 2655

Cooper, M. C., et al. 2006, MNRAS, 370, 198

Crocce, M., Cabré, A., & Gaztañaga, E. 2011, MNRAS, 414, 329

Croton, D. J., et al. 2006, MNRAS, 365, 11

Davis, M., et al. 2007, ApJ, 660, L1

de Putter, R., Doré, O., & Das, S. 2013, ArXiv e-prints

Duran, I., Atrio-Barandela, F., & Pavón, D. 2012, JCAP, 4, 8

Eisenstein, D. J., et al. 2005, ApJ, 633, 560

Faber, S. M., et al. 2007, ApJ, 665, 265

Finkelstein, S. L., et al. 2012, ApJ, 756, 164

Fukugita, M., Ichikawa, T., Gunn, J. E., Doi, M., Shimasaku, K., & Schneider, D. P. 1996, AJ, 111, 1748

Gerdes, D. W., Sypniewski, A. J., McKay, T. A., Hao, J., Weis, M. R., Wechsler, R. H., & Busha, M. T. 2010, ApJ, 715, 823

Green, J., et al. 2012, ArXiv e-prints

Grogin, N. A., et al. 2011, ApJS, 197, 35

Gwyn, S. D. J. 2012, AJ, 143, 38

Hamilton, A. J. S. 1998, in Astrophysics and Space Science Library, Vol. 231, The Evolving Universe, ed. D. Hamilton, 185–+

Hartlap, J., Simon, P., & Schneider, P. 2007, A&A, 464, 399

Hearin, A. P., Zentner, A. R., Ma, Z., & Huterer, D. 2010, ApJ, 720, 1351

Hoaglin, D. C., Mosteller, F., & Tukey, J. W. 1983, Understanding robust and exploratory data anlysis (Wiley-Interscience)

Hoerl, A. E., & Kennard, R. W. 1970, Technometrics, 12, 69

Hubble, E. 1929, Proceedings of the National Academy of Science, 15, 168

Huterer, D., Takada, M., Bernstein, G., & Jain, B. 2006, MNRAS, 366, 101

Ilbert, O., et al. 2006, A&A, 457, 841

Jackson, D. D. 1972, Geophysical Journal International, 28, 97

Jain, B., Scranton, R., & Sheth, R. K. 2003, MNRAS, 345, 62

Johnston, R. 2011, A&A Rev., 19, 41

Johri, V. B., & Rath, P. K. 2007, International Journal of Modern Physics D, 16, 1581

Jose, C., Srianand, R., & Subramanian, K. 2013, MNRAS, 435, 368

Kaiser, N. 2011, Astrophysics Source Code Library, 8001

Kaiser, N., Wilson, G., Luppino, G., & Dahle, H. 1999, ArXiv Astrophysics e-prints

Kitzbichler, M. G., & White, S. D. M. 2007, MNRAS, 376, 2

Knox, L., Song, Y., & Zhan, H. 2006, ApJ, 652, 857

Kovač, K., Somerville, R. S., Rhoads, J. E., Malhotra, S., & Wang, J. 2007, ApJ, 668, 15

Landy, S. D., & Szalay, A. S. 1993, ApJ, 412, 64

Le Fèvre, O., et al. 2005, A&A, 439, 845

Lemson, G., & Virgo Consortium, t. 2006, ArXiv Astrophysics e-prints

Lilly, S. J., et al. 2007, ApJS, 172, 70

—. 2009, ApJS, 184, 218

Loveday, J., et al. 2012, MNRAS, 420, 1239

Loverde, M., Hui, L., & Gaztañaga, E. 2008, Phys. Rev. D, 77, 023512

LSST Science Collaborations: Paul A. Abell et al. 2009, ArXiv e-prints

Ma, Z., & Bernstein, G. 2008, ApJ, 682, 39

Ma, Z., Hu, W., & Huterer, D. 2006, ApJ, 636, 21

MacDonald, C. J., & Bernstein, G. 2010, PASP, 122, 485

Matthews, D. J., & Newman, J. A. 2010, ApJ, 721, 456

—. 2012, ApJ, 745, 180

Matthews, D. J., Newman, J. A., Coil, A. L., Cooper, M. C., & Gwyn, S. D. J. 2013, ApJS, 204, 21

McBride, C. K., Connolly, A. J., Gardner, J. P., Scranton, R., Scoccimarro, R., Berlind, A. A., Marín, F., & Schneider, D. P. 2011, ApJ, 739, 85

McLure, R. J., et al. 2011, MNRAS, 418, 2074

McQuinn, M., & White, M. 2013, MNRAS, 433, 2857

Meiksin, A., Szapudi, I., & Szalay, A. 1992, ApJ, 394, 87

Ménard, B., & Bartelmann, M. 2002, A&A, 386, 784

Ménard, B., Scranton, R., Schmidt, S., Morrison, C., Jeong, D., Budavari, T., & Rahman, M. 2013, ArXiv e-prints

Moessner, R., & Jain, B. 1998, MNRAS, 294, L18

Morrison, C. B., Scranton, R., Ménard, B., Schmidt, S. J., Tyson, J. A., Ryan, R., Choi, A., & Wittman, D. M. 2012, MNRAS, 426, 2489

Newman, J., et al. 2013a, ArXiv e-prints

Newman, J. A. 2008, ApJ, 684, 88

Newman, J. A., et al. 2013b, ApJS, 208, 5

Ouchi, M., et al. 2001, ApJ, 558, L83

—. 2004, ApJ, 611, 685

—. 2008, ApJS, 176, 301

—. 2010, ApJ, 723, 869

Peebles, P. J. E. 1980, The Large-Scale Structure of the Universe (Princeton University Press)

Peebles, P. J. E., & Yu, J. T. 1970, ApJ, 162, 815

Percival, W. J., et al. 2010, MNRAS, 401, 2148

Perlmutter, S., et al. 1999, ApJ, 517, 565

Press, W. H., Teukolsky, S. A., Vetterling, W. T., & Flannery, B. P. 1992, Numerical recipes in C. The art of scientific computing (Cambridge University Press)

Quadri, R. F., & Williams, R. J. 2010, ApJ, 725, 794

Riess, A. G., et al. 1998, AJ, 116, 1009

Ryan, Jr., R. E., et al. 2007, ApJ, 668, 839

Schechter, P. 1976, ApJ, 203, 297

Schlegel, D., et al. 2011, ArXiv e-prints

Schlegel, D. J., Finkbeiner, D. P., & Davis, M. 1998, ApJ, 500, 525

Schmidt, S. J., Ménard, B., Scranton, R., Morrison, C., & McBride, C. K. 2013, MNRAS, 431, 3307

Schneider, M., Knox, L., Zhan, H., & Connolly, A. 2006, ApJ, 651, 14

Schulz, A. E. 2010, ApJ, 724, 1305

Scranton, R., et al. 2005, ApJ, 633, 589

Shimasaku, K., et al. 2003, ApJ, 586, L111

Stoughton, C., et al. 2002, AJ, 123, 485

Sun, L., Fan, Z., Tao, C., Kneib, J., Jouvel, S., & Tilquin, A. 2009, ApJ, 699, 958

Szapudi, I., Szalay, A. S., & Boschan, P. 1992, ApJ, 390, 350

The Dark Energy Survey Collaboration. 2005, ArXiv Astrophysics e-prints

Tyson, A., & Angel, R. 2001, in Astronomical Society of the Pacific Conference Series, Vol. 232, The New Era of Wide Field Astronomy, ed. R. Clowes, A. Adamson, & G. Bromage, 347–+

Tyson, J. A. 2006, in American Institute of Physics Conference Series, Vol. 870, Intersections of Particle and Nuclear Physics: 9th Conference CIPAN2006, ed. T. M. Liss, 44–52

Wiggins, R. A. 1972, Reviews of Geophysics and Space Physics, 10, 251

Willmer, C. N. A., et al. 2006, ApJ, 647, 853

Yan, H., et al. 2012, ApJ, 761, 177

Yan, H.-J., Windhorst, R. A., Hathi, N. P., Cohen, S. H., Ryan, R. E., O'Connell, R. W., & McCarthy, P. J. 2010, Research in Astronomy and Astrophysics, 10, 867

Zacharias, N., Urban, S. E., Zacharias, M. I., Wycoff, G. L., Hall, D. M., Monet, D. G., & Rafferty, T. J. 2004, AJ, 127, 3043

Zehavi, I., et al. 2005, ApJ, 630, 1

Zhan, H. 2006, Journal of Cosmology and Astro-Particle Physics, 8, 8

Zhan, H., & Knox, L. 2006, ApJ, 644, 663

Zhang, P., Pen, U.-L., & Bernstein, G. 2010, MNRAS, 405, 359